Technische Universität München

Max-Planck-Institut für Physik
(Werner-Heisenberg-Institut)

Search for multi-TeV gamma ray emission from the SN1006 remnant with the HEGRA CT1 telescope

Vincenzo Vitale

Vollständiger Abdruck der von der Fakultät für Physik der Technischen Universität München zur Erlangung des akademischen Grades eines

Doctors der Naturwissenschaften

genehmigten Dissertation.

Vorsitzender:
Univ.Prof.Dr. Manfred Lindner

Prüfer der Dissertation:
1. Hon.Prof.Dr. Siegfried Bethke
2. Univ.Prof.Dr. Franz v. Feilitzsch

Die Dissertation wurde am 01/06/2004 bei der Technischen Universität München eingereicht und durch die Fakultät für Physik am 20/07/2004 angenommen.

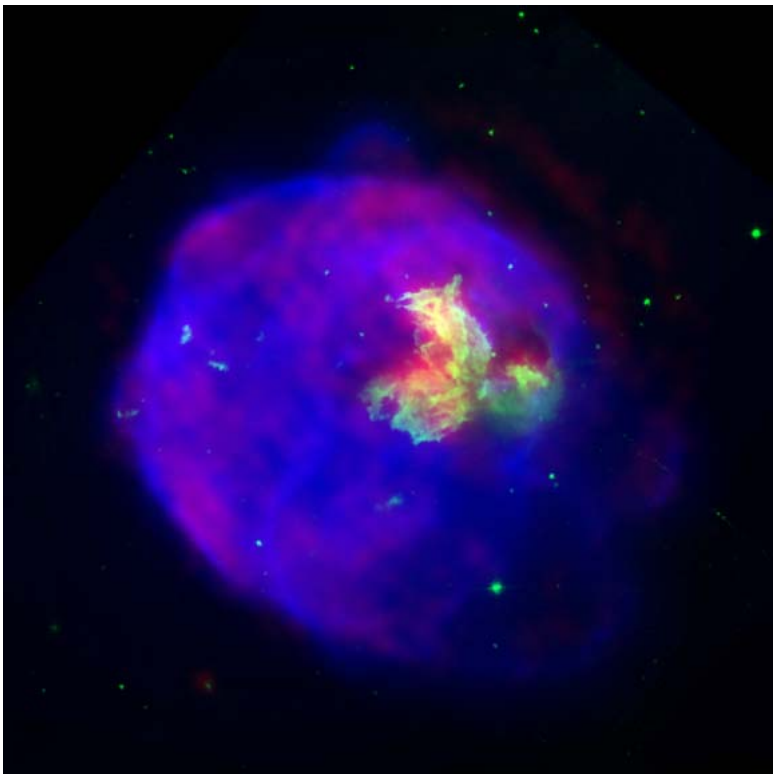

Figure 1: Image of N63A, a supernova remnant located in the Large Magellanic Cloud. This image contains X-rays from Chandra (blue), combined with optical (green) and radio (red) data. The X-ray glow is from material heated to about ten million degrees Celsius by a shock wave generated by the supernova explosion. The remnant age is estimated between 2,000 to 5,000 years. Optical and radio light are of the remnant, which appears as a triangular-shaped "hole" in the X-ray image. The hole is produced by absorption of X-rays in a dense cloud of cooler gas and dust on the side of the remnant nearest the Earth. A comparison of the X-ray image with the radio and optical images suggests that the shock wave is engulfing this massive cloud, so we see only the edge nearest the Earth. Courtesy of Chandra X Ray Observatory.

SUMMARY

The Galactic Cosmic Rays (GCRs, those Cosmic Rays with intermediate energy between 10s of GeV and 100s of TeV per unit of charge) are known from more than nine decades. Nevertheless, we still know very little about their origins. The Super Nova Remnants (SNRs) are the most popular GCRs candidate accelerators. But up to now we miss an unquestioned experimental proof of this theory. Therefore we investigated the SN 1006 remnant. This shell type remnant has been produced by the bright Super Nova, which has been visible during the year 1006. This is one of the few sources, from which TeV γ rays have been detected. The HEGRA collaboration tried to observe SN1006 in an up to now unexplored energy region above $\approx$ 15TeV. Here below I summarize the observations of the SN1006 with the HEGRA CT1 telescope. Very briefly the main steps of the data analysis and the main achievements are also listed.

We observed SN 1006 for more than 220 hours from 1999 to 2001 with the HEGRA CT1 telescope. CT1 is part of the HEGRA cosmic rays detector complex at La Palma (28.75° N, 17.9° W, 2225 m asl). SN 1006 (RA 15:02:48.8, Dec -41:54:42) culminates at less than 20° of elevation when observed from La Palma. Therefore only large zenith (ZA) angle observations are possible. We collected in total more than 346000 so-called ON-source events, restricting observations to a narrow range between 71 and 73° ZA, as well as a small set of OFF-source data at the same ZA. We recorded also a large background sample of muons passing through the telescope camera. Such muons leave narrow images, which might mimic γ events.

The data analysis of the SN 1006 data has been performed (as a part of my doctoral work), in order to search for the possible multi-TeV emission from this source. Some innovations have been introduced to the standard analysis techniques. The main of them are :

1. The development and the validation of a novel background rejection method. The standard rejection is un-effective for the SN 1006 data, because of the large zenith angle (the present observation is the one at largest zenith angle ever successfully performed).

2. The implementation of a 2-dimensional analysis (False Source Method) and the scan of the CT1 field of view. The standard analysis is op-

timized for point-like objects, while SN 1006 remnant is an extended one.

3. A new treatment for the residual background (the so-called *Ring method*) which is used together with the CT1 standard one (the so-called *Alpha fit*).

4. The telescope calibration (i.e. calculation of the *effective collection area, Impact parameter* and *Energy* reconstruction). Also the calibration is affected by the large zenith angle, and therefore it is a new one.

With the above mentioned analysis, the following main results have been achieved:

- **The detection of TeV γ rays from the North-East cap of the SN1006 remnant**, in accordance with the previous detection made by the CANGAROO collaboration.

- The TeV γ rays emission is detected as an excess of events. The excess consists of 103±17 events. The residual background consists of 225±9 events.

- **the excess significance is 5.1 standard deviations (σ)**, in accordance with the Lee and Ma theory, which is usually applied within the γ ray astronomy field. The initial significance was 5.6 σ, it has been reduced in order to account for the position indetermination.

- The integral flux is:

$$\Phi_\gamma(E > 18 \pm 2TeV) = (2.35 \pm 0.4_{stat})10^{-13} cm^{-2} s^{-1}$$

  This flux is obtained under the assumption that: the source emits a differential energy spectrum in the form of a pure power-law, with spectral index Γ = -2.0, which is the value favoured by the differential spectrum fit. The energy threshold (E_{th}) for the same photon index is 18±2 TeV.

- **A systematic uncertainty $\delta\Phi_{syst.}$ = 30%** has been considered for the fluxes calculations. With the inclusion of the systematic errors, the integral flux, for Γ = -2.0, becomes:

$$\Phi_\gamma(E > 18 \pm 2TeV) = (2.35 \pm 0.4_{stat} + 0.7_{syst.})10^{-13} cm^{-2} s^{-1}$$

  .

- The differential flux, in the form of a pure power law C $_{scale}\times$E$^{-\Gamma}$, is:

$$\frac{d\Phi}{dE} = (0.30 \pm 0.15) \times 10^{-11} \times (\frac{E}{TeV})^{-1.9\pm0.2}\ TeV^{-1}\ cm^{-2}\ s^{-1}$$

  The errors include the statistical ones, and those for the energy reconstruction. A 30 % systematic error is not included.

- No signal (events excess with significance larger than 5σ) has been found at the South-West cap and at the central region location. It is therefore possible to set an upper-limit for the integral flux from the South-West cap:

$$\Phi(E > 18 \pm 2TeV)_{\gamma,SW} = 0.83 \times 10^{-13} cm^{-2} s^{-1}$$

  at a confidence level of 95%, under the assumption of a power law with photon index Γ=-2.

  The upper limit for the SNR central region is:

$$\Phi(E > 18 \pm 2TeV)_{\gamma,center} = 0.66 \times 10^{-13} cm^{-2} s^{-1}$$

  also this at a confidence level of 95%, under the assumption of a power law with photon index Γ=-2.

Contents

Introduction

Many important discoveries have been performed by means of the study of the Cosmic Radiation. Cosmic Rays are energetic particles, of many different types, having their origin outside of our planet. The potential for further discoveries is still high, also after a century of research (Hess 1912). In Fig.2,3 and 4 one can see, for example, three very different experiments for the detection of cosmic particles, which are related to hot topics of contemporary physics. Some open basic questions about Cosmic Rays are:

- where do they come from ?
- how they gain their very high energy ?

This doctoral work deals with these questions. A simple mechanism for the acceleration of charged particles, by astrophysical objects, has been introduced many years ago (Fermi, [1]). After that more refined theories have been developed and few classes of objects have been suggested as cosmic accelerators. The Super Nova Remnants (SNRs) are the most popular candidate as accelerators of the Galactic Cosmic Rays (those with intermediate energy, between 10s of GeV and 100s of TeV per unit of charge). But up to now we miss an unquestioned experimental proof that SNRs accelerate the Galactic Cosmic Rays. An experimental effort is needed and we want to contribute to that with this study.

Are Galactic Cosmic Rays accelerated by the shock waves of the SNRs? There is no way to test this hypothesis *"in situ"*. But the emission of very high energy (VHE) γ rays may be an indirect evidence. Therefore we searched for VHE γ rays from the SN1006 remnant. This remnant is one of the three shell-type SNRs (SN1006, RXJ1713 and Cassiopeia A), emitting VHE γ rays, today known.

The present work is divided in the following chapters:

1. *Super Nova Remnants.*

   The main hypothesis under test, with this thesis, is:

   - are multi-TeV γ rays emitted from the North East cap of the SN1006 remnant ?

   Therefore the related basic physics is shortly discussed. The reader will find: the description of the Super Nova remnant and its evolution; the motivation to expect γ emission and the connection to the acceleration of Galactic Cosmic Rays.

2. *Imaging Atmospheric Cherenkov Telescope (IACT).*

   The atmospheric Cherenkov telescope HEGRA CT1 is the tool, with which this experimental study has been performed. Then, in chapter 2, one can read about: the development of the atmospheric air showers; the HEGRA CT1 set-up, as an example of stand-alone IACT.

3. *Data Analysis*

   The analysis of the SN1006 data has been performed, in oder to achieve the research objectives. This has been my work. It is reported in details from chapter 3. The main analysis parts are:

   (a) The development and validation of a novel background rejection method. It was needed to reject the dominant hadronic background and a significant muon one. The standard rejection for low zenith angles is un-effective for the SN1006 analysis. In fact the present observation is the one at largest zenith angle ever successfully performed. Therefore a new method was developed.

   (b) The implementation of a 2-dimensional analysis (False Source Method) and the scan of the CT1 field of view. The SN1006 remnant is an extended object for the angular resolution of CT1. Therefore at least a part of the remnant is observed off-axis and the 2-dimensional analysis was needed.

   (c) A new treatment for the residual background (the so-called *Ring method*), which is used together with the CT1 standard one (the so-called *Alpha fit*).

   (d) The telescope calibration (i.e. calculation of the *effective collection area*, *Impact parameter* and *Energy* reconstruction). Also the calibration is affected by the large zenith angle observation, and therefore it is a new one.

4. *Results and Discussion*

   The reader can find the results in chapter 4. They are reported in details, then are compared to the results of the other experiments. A results discussion follows.

5. *Appendices*

   In the Appendices are discussed:

   (a) the Diffusive Shock Acceleration;

   (b) the Cosmic Rays.

Figure 2: The MAGIC atmospheric Cherenkov telescope, for the study of very high energy γ rays from astrophysical sources. The CT1 telescope is the experimental precursor of MAGIC. MAGIC is the today largest atmospheric Cherenkov telescope, and has the lowest energy threshold (10-30 GeV). (Courtesy of MAGIC gallery Uni.Wuerzburg, http://www.astro.uni-wuerzburg.de/magic/gallery)

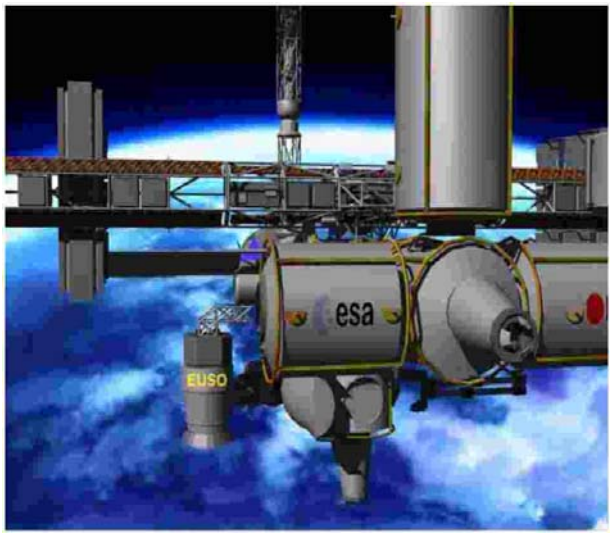

Figure 3: The future EUSO detector, for the study of the UHE cosmic rays, on board of the ISS (simulation).

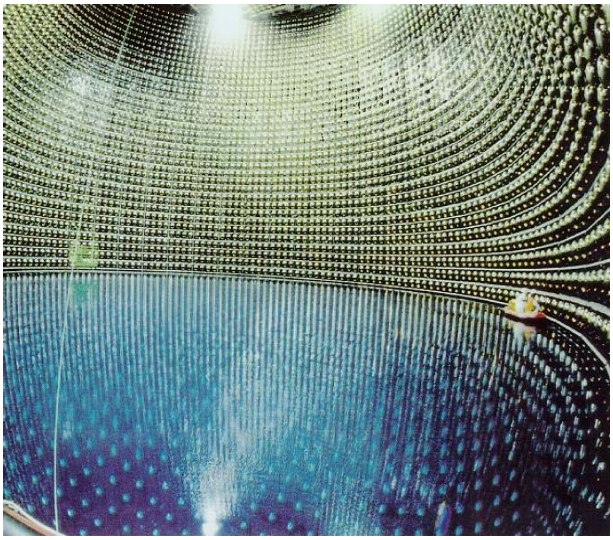

Figure 4: The super-Kamiokande experiment for the study of solar and atmospheric neutrinos.

Chapter 1

Supernova Remnants

The astrophysical object studied in this thesis is a Supernova Remnant (SNR) of shell type. Therefore I will describe what a SNR is. In section 1.1 I introduce the stellar evolution and the Supernova (SN) explosion, from which the SNR has its origin. The main references for this chapter are [2] and [3]. A supernova remnant (SNR) consists of matter ejected during the SN explosion. When this matter expands it sweeps up the Inter-Stellar Matter (ISM) and mixes with it. The evolution of the SNR is described in section 1.2. In some cases a compact object, as a neutron star (or a black hole), stays together with the ejecta to form a different type of remnant. A compact object and the ejecta can also interact. A short introduction to different SNRs types is given in subsection 1.2.4.

The interaction of the remnant with the ISM causes a number of interesting phenomena. From these phenomena radiation which spreads at many different wave-lengths (from radio to TeV γ rays) is received. The acceleration of the Galactic Cosmic Rays (GCRs) may be one of these phenomena. The SNRs are considered to be the most likely candidates as accelerators of the GCRs (see section 1.3). The basic mechanism of acceleration of the GCRs is reported in the appendix A, and the main properties of Cosmic Rays are described in the appendix B.

It is not possible to track back the charged cosmic rays because they are deflected and trapped by the galactic magnetic field. The charged cosmic rays arrive at the Earth with isotropically distributed directions. Instead, very high energy γ rays travel on a straight line into the galaxy. Gamma rays can be used as a probe to study the acceleration of the GCRs. The emission of very high energy γ rays coming from the SNRs, where these SNRs accelerate charged particles, is described in section 1.4 In the end

of this chapter (section 1.5) the recent observations of the remnant of the SN1006 are reviewed.

1.1 SNR genesis

Relations between the parent supernova and the remnant are strong:

- the supernova explosion provides energy for powering the expansion of the remnant;
- the amount and the type of ejected matter and also the remnant type are directly dependent on the supernova type;
- the environment into which the remnant expands can be highly influenced by the eventual stellar wind of the SN precursor.

Therefore in the following subsections I briefly discuss the SNe.

1.1.1 Supernovae classification

Supernovae are powerful stellar explosions. In some cases, for short time, they are brighter than their host galaxy (or comparable, see Fig 1.1). They are important for the physics of the galaxy. They eject the produced heavy elements and release considerable amount of energy. Supernovae are classified on the basis of their optical spectrum, which is very well known.

1. Type I → SN without hydrogen lines
   (a) Type Ia → SN with strong silicon lines
   (b) Type Ib → SN without strong silicon lines but with helium lines
   (c) Type Ic → SN without strong silicon lines and without helium lines

   Supernovae of Type Ia are the brightest. They show more constant light curve, consisting of a fast rise and an exponential decay of 55 days of characteristic time. They happen in all types of galaxies. Such features suggest that their progenitors are common stars of the same type (white dwarf at limit of Chandrasekhar mass)

2. Type II → with hydrogen lines
   (a) Type II-Linear → light curve with an exponential decay

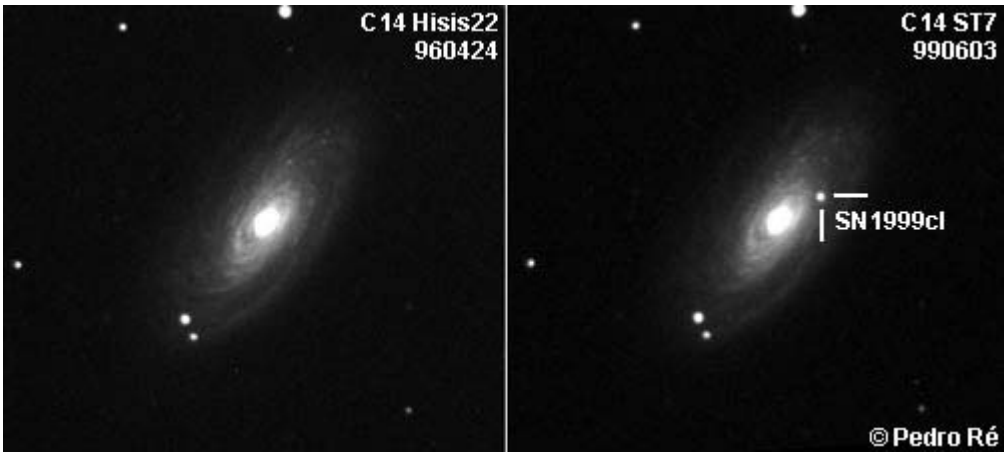

Figure 1.1: Comparison plates for the SN1999cl (IAUC 7185). The SN1999d was discovered May 29^{th}, 1999 by the Lick Observatory Supernova Search. On the left there is a plate of the host galaxy observed in 1996, and on the right an image from June 1999. The bright new source is the Supernova. The SN exploded in M88 at R.A. = 12h31m56s.01, Decl. = +14 25'35".3 (N. Fukahara finder chart). It is located 46" west and 23" north of the nucleus of NGC 4501 (= M88). The SN Mag was 15.1, it is classified as Type Ia. Image property of Pedro Re (pedrore@mail.telepac.pt)

(b) Type II-Plateau $\rightarrow$ light curve with an exponential decay plus a plateau lasting $\approx$ 100 days

Type II SNe have a more irregular light curve than the Type Ia, they have a slower rise and on average they are two magnitudes less luminous; a part of them exhibit a plateau, which is superimposed to the exponential decay, in their light curve. Type II SNe have been seen in arms of spiral galaxies, where the young giant stars are present and rarely seen in elliptical galaxies. It supports the idea that Type II SNe come from the core collapse of very massive stars.

1.1.2 Pre SN stellar evolution

In a crude approximation, a star is a spherical distribution of matter with mass in the order of 2×10^{30}Kg (= 1 $M_{\odot}$). The star evolves with time; the evolution can be followed over the Hertzsprung-Russell diagram (Fig.1.2). The matter that composes the star is affected by the strong gravitational

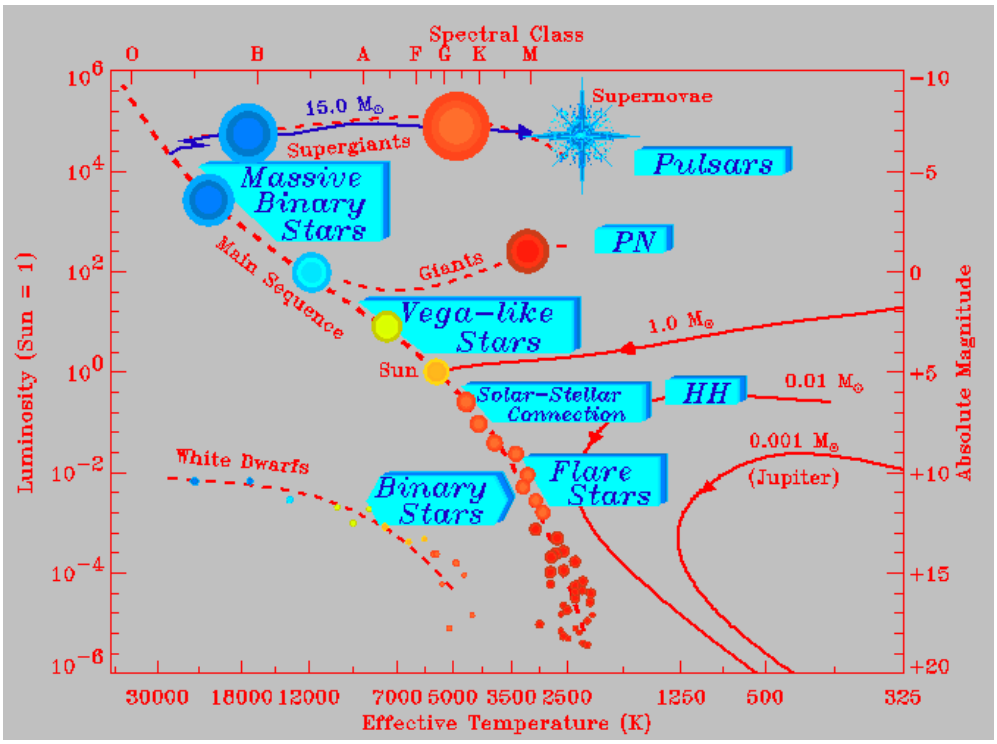

Figure 1.2: The diagram above is an example of the Hertzsprung-Russell (H-R) diagram. The first such diagram was plotted by Ejnar Hertzsprung in 1911, and (independently) by Henry Norris Russell in 1913. It is a "two-dimensional" plot for the observed stars, and represents one of the greatest observational synthesis in astronomy and astrophysics. In the diagram the Absolute Magnitude is plotted versus the Effective Temperature (an indicator of the temperature of the star surface). A star lies in in the H-R diagram in dependence on the evolution phase. The main regions of the H-R diagram are : a) the "Main Sequence", b) the "Red Giants" branch , c) the "Blue Supergiants" branch , and d) the white dwarfs region. Illustration property of B. Kellet (see [4])

field, which is generated by the star itself. Therefore the star tends to collapse. The star reaches a steady state when the gravitational collapse is balanced by a counter-acting pressure. In case of an ordinary star ("Main Sequence" star) this pressure comes from the nuclear reactions, which release energy. The nuclear fusion, of light elements into heavier ones, acts,

when the temperature of the reacting fuel is above a given threshold. Only light elements (H, He) are burned in small stars (< 1.44 $M_\odot$, the so-called Chandrasekhar limit). These small stars restart to collapse after they exhaust their light elements. The *free falling* collapse stops when the density rises to $10^9 \frac{Kg}{m^3}$. At this stage the degeneracy pressure of electrons counterbalances the gravity. Then the star is again in a steady state. It has the dimensions of an earth-like planet and is composed mainly by Carbon and Oxygen. It is named white dwarf because of the size and the hot surface.

Massive stars (> 10 $M_\odot$) have different stellar evolution. At first they burn light elements in their core. Then heavier elements (produced by the previous reactions) in the core and lighter elements in the outer shells, around the core, are burnt. The massive star becomes a multi-shell structure (onion-like), made of layers of different elements. These elements are the heavier the closer to the core of the star. A new stage of the evolution starts when the core is composed by Iron. Iron is a very stable nucleus, the fusion of two nuclei of Iron into a heavier element requires energy. Then in the core the gravity is not counter-balanced. As a consequence the core shrinks. It reaches a steady state when the degeneracy pressure of electrons counter-balances the gravity, as in the case of the white dwarfs. In the meantime, when the outer layers increase their activity as a response to the higher temperature, the star expands and becomes a red giant.

1.1.3 Type Ia Supernovae

The progenitors of the Type Ia SNe are likely to be white dwarfs having mass close to the Chandrasekhar limit. These stars compose a class of homogeneous objects, that can justify the strong regularity of the SNe of Type Ia. The mass of a white dwarf is increased by means of a suitable mass accretion process. The mass exchange within a close binary system is one of the processes proposed to explain that. When the mass of the white dwarf is accreted, the gravitational field overcomes the degeneracy pressure. The whole star collapses and increases the density. Under such conditions the nuclear reactions start again, this time their behavior is explosive. Then the star explodes as a Supernova and is fully disrupted.

The Type Ia SN explosion releases 10^{51} ergs of energy. Only 1% appears as visible light, while the rest is available as kinetic energy to blow up the SN ejecta at a speed of more than $10^7 \frac{m}{s}$ ($\approx 3.3 \times 10^{-2}$ of speed of light). Approximately 1 $M_\odot$ of ^{56}Ni, together with many other elements and isotopes, are produced by the major nucleo-synthesis processes.

1.1.4 Core collapse SNe (Type II, Ib/c)

The core made of Iron, in massive stars, is not stable for a long time. Heavy nuclei are decomposed into the lighter ones. This process is supported by the energy generated in the outer shells of the star in which the nuclear fusion is still active. Heavy nuclei are decomposed and many protons are freed. These free protons interact with the electrons in the core, for example in the following weak interaction:

$$p^+ \; e^- \; \rightarrow \; n \; \nu_e \tag{1.1}$$

The above reaction depletes the electrons in the core of the star. Such electrons are responsible for the degeneracy pressure which makes the core stable. Therefore the core is overbalanced and starts to collapse again. The next stages of the collapse are very complex and their treatment goes beyond this introduction (see [5]).

After the collapse of the core the star explodes as a Supernova. The outer layers of the star are ejected with the explosion, while a part of the core forms a very compact object. Such a compact object can be :

- a neutron star, if the degeneracy pressure (this time made by the nucleons) is enough to balance the gravitation;
- a black hole, when the collapse ends into a gravitational *singularity.*

SNe of Type II are supposed to be the explosions of stars which still hold their external layer of hydrogen; while Type Ib and Ic progenitors have lost their hydrogen through the stellar winds or interactions in the binary systems. A SN of Type II releases 10^{53} ergs of energy. A large fraction of energy is carried away by neutrinos (99%). These neutrinos are generated during the core collapse. Also for Type II SNe 10^{51} ergs of energy are available for the expansion of the SN ejecta, which have speed of $\approx 5 \times 10^6 \frac{m}{s}$. The light output carries 10^{49} ergs, which is comparable to the rotational energy of the compact core remnant.

1.2 SNR expansion in the interstellar matter (ISM)

The evolution of the SNR is studied by the means of observations of the known SNRs. The galactic SNRs known today amount to more than 230, while around 30 are observed in the Large and Small Magellanic Clouds [6]. A fraction of galactic SNRs are the remnants of the historical SN recorded by the ancient astronomers (see Tab 1.1). Many SNR have been discovered

SN	SNR	type	Chinese	Japanese	Korean	Arabic	European
A.D.1006	1006	shell	many	many		many	two
A.D.1054	Crab	plerion	few	few			
A.D.1181	3C 58	plerion	many	few		one	
A.D.1572	Tycho's	shell	few		one		many
A.D.1604	Kepler's	shell	few		many		many
A.D.1680	Cas A	shell					

Table 1.1: Table of the main historical records of SNe and related SN remnants. Not many observations were reported in A.D.1680

as extended radio emitters. SNRs are also searched in the X rays surveys because of the sensitivity and resolution development of the X rays detectors ([7],[8] and [9]).

Theoretical models should match the observed properties of the SNRs. The basic model [10] of a shell type SNR consists of an expansion of a given quantity of plasma into the interstellar matter. In this model all the properties are originated from the starting conditions like:

- ejecta mass;
- SN energy;
- ejecta velocity;
- ISM density.

Such a model is just an approximate description of a remnant. It is not adequate to describe the real complexity of a SNR. A more precise model has to consider also the individual morphology of remnants and many other factors which are neglected at the first approximation.

The SNR evolves during four main stages, characterized by different thermodynamic behaviour. These stages are :

1. the free expansion stage
2. the Sedov-Taylor stage
3. the radiative stage
4. the merging into the ISM

1.2.1 Free expansion stage

During the SN explosion masses in the order of some $M_\odot$ are ejected. Approximately 10^{50}-10^{51} ergs of kinetic energy are available for the ejection. During the free expansion the radius of the remnant is a linear function of time:

$$R_{SNR} \;=\; t \times \sqrt{\frac{2\ E_0}{M_{ejecta}}} \tag{1.2}$$

where $\sqrt{\frac{2\ E_0}{M_{ejecta}}}$ is in the order of $10^7 \frac{m}{s}$. In the ISM the sound speed is in the order of 10 $\frac{Km}{s}$ (for an ISM temperature of 10^4K and assuming an ideal monoatomic gas [11]). Therefore the ejecta move with supersonic velocity in the ISM and a shock wave arises. The shock wave travels in front of the ejecta and collects the ISM particles which it meets along the path. The meaning of *free expansion* is that the medium surrounding the SN has a low density and does not change the ejecta motion. The free expansion stage lasts from 100 to 1000 years, depending on the ISM density and ejecta mass.

1.2.2 Sedov-Taylor stage

The shell increases the mass because of the *snowplough* effect. The SNR enters the Sedov-Taylor stage when the swept-up ISM has reached the same order of magnitude as the original ejecta. At this point the expansion of the shell is considerably slowed down because of the increasing of the mass. At the first order the accretion in mass follows the relation, as given below:

$$M(t) \;\approx\; \frac{4\pi}{3}\ \rho_0\ R_{SNR}^3 \tag{1.3}$$

where ρ_0 is the ISM density, in the order of $0.3 \times 10^6 \frac{particles}{m^3}$ and does not change in the relevant region of space. The ISM density can be of higher value and heterogeneous . For example when the SN explodes into the stellar-wind generated by the precursor-star. In that case the density will be considerably higher and it will be an exponential function of the distance from the precursor-star

During the Sedov-Taylor stage an other shock arises. A reverse shock propagates inwards as a consequence of the slowing down of the external shock. The reverse shock is generated because the internal part of the remnant is less affected by the resistance of the swept-up material and its relative velocity to the external shock increases.

Both the forward and the reverse shocks heat the matter, which they cross. Shock heating is responsible for the thermal radiation from the SNR. The internal energy is almost unchanged also if the expansion slows down. This is because the SNR matter is very hot and the radiative energy emission is not efficient. An approximation for the shock temperature is:

$$T = (\frac{E_0}{n\ R^3}\ )\ 10^{10}\ K \tag{1.4}$$

where E_0 is the starting energy in units of 10^{51} ergs, R is the remnant radius in pc, n is the ISM density in cm^{-3} and K is the symbol for Kelvin degrees.

1.2.3 Radiative stage and merging into the ISM

The radiation mechanism becomes more effective when the shell cools down. At the temperature of 2×10^5 K a fraction of Carbon and Oxygen can partially recombine. Such atoms can radiate energy using a very efficient ultraviolet line emission. The radiative stage lasts 10^5 years and at the end all the internal energy of the SNR is radiated away. Thermal X rays are also produced during the free expansion and during the Sedov-Taylor phases. Instead bright optical filaments are the characteristics of the remnants at radiative stage. The SNRs also emit thermal radio-waves from the cooling filaments, and from the gas previously heated by the shock.

The SNR matter merges into the ISM after the radiative phase. At that time the SNR is composed by the SN ejecta and by an important component of the swept-up ISM. The merging of the SNR into the ISM is important for the galaxy evolution. As a result of the merging:

- the new heavy elements, synthesized by the SN processes, enter the galaxy;
- a new generation of metal-rich stars can be build up;
- a huge amount of energy is released by the SNR. This energy is responsible for the heating of the ISM, which would be much cooler without the SNR energy injection.

1.2.4 Morphology

Basic types of the SNR are :

- shell SNRs: their shape is of a roughly spherical shell. Their emissions come mainly from the shell, while the central region is less bright. Examples of shell-type SNR are the SN1006 and also the Tycho SNR (see Fig.1.3).

- plerionic SNRs: plerionic SNRs are center-filled remnants. Their emissions come mainly from a localized region, usually at the center of the object. A neutron star is supposed to be in the bright region. A representative plerionic SNR is the Crab SNR (Fig.1.4)

- composite SNRs: this type of SNR has both the features of the plerionic and of the shell-type remnants. There are more than 20 galactic composite SNRs. In these remnants both the shell and the compact object are active, in some of them they interact. For example see Fig. 1.5 in which Kes75 is shown.

In the following three images of different SNR types are shown. All of them are the X rays observations, obtained by the Chandra X-rays observatory [12].

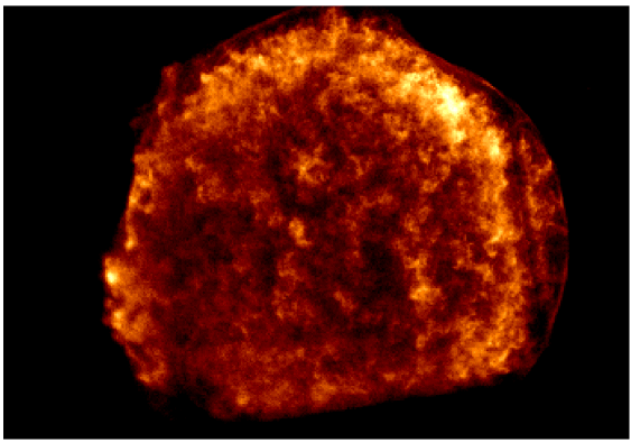

Figure 1.3: The shell-type SNR: X rays image of the Tycho SNR (Chandra satellite). The basic data of the Tycho SNR are: size of about 6 pc (in diameter); distance of about 2.4 kpc; age of 430 years. The SN was observed by the Danish astronomer Tycho Brahe in 1572. In this picture it is possible to see the clumpy structure and the (possible) shock front.

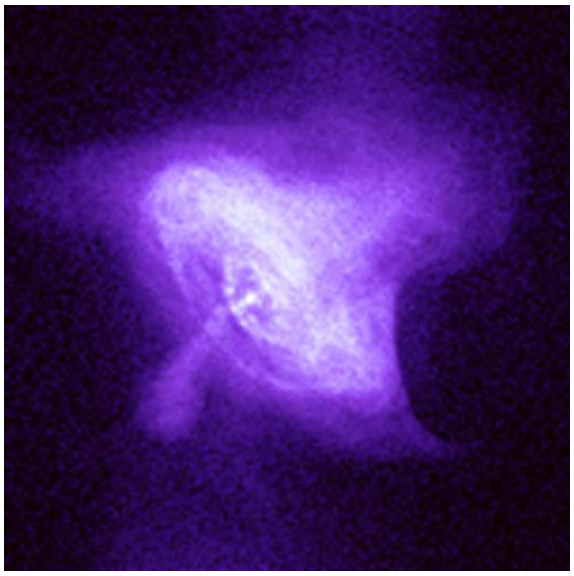

Figure 1.4: The plerionic SNR: X rays image of the Crab SNR (Chandra satellite). The basic data of the Crab SNR are: size of 43 pc, distance of 2 kpc; age of $\approx$ 950 years. The supernova explosion was observed by the Chinese (5 texts, 4 independent) and Japanese astronomers (3 texts, 2 independent) in 1054. In this picture it is possible to see the central bright object and a jet-like structure.

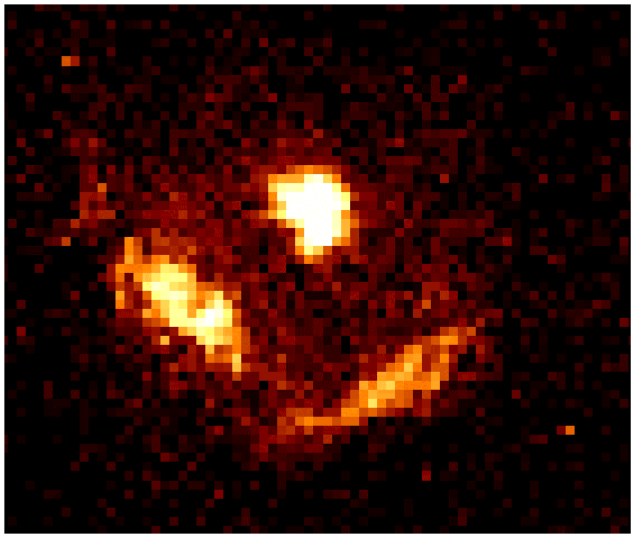

Figure 1.5: The composite SNR: X rays image of the Kes75 SNR (Chandra satellite). The basic data of the SNR G29.7-0.3 (Kes75) are: size of about 13 pc (in diameter); distance between 9 and 20 kpc; age of about 700 years.

1.3 Galactic Cosmic Rays acceleration at SNR

Supernova remnants are considered to be the most likely candidates as accelerators of the Galactic Cosmic Rays (GCR) of energy from 10s of GeV up to 100s of TeV-few PeV, per unit of charge. This idea is already few decades old. But the direct unquestioned proof, that the SNRs are the accelerators of the GCRs, is missing. Many types of researches are carried out in order to verify the relation between the SNRs and the GCRs. These researches span from the direct study of the GCRs composition and energy spectrum to the radio, X rays and γ rays astronomy.

From the basic observations we know that the GCRs start as common galactic nuclei. Those particles gain a very high energy during an *acceleration* process. Because the observed cosmic rays come from the outer space, the acceleration of the GCRs should happen into, or around, an astronomical object . And as we can indirectly observe cosmic rays in the other galaxies [13], the same object should be common in the universe.

The SNRs are considered to be good candidates for few simple reasons, the most important of which are :

- energy requirements;

  An estimate [14] of the power which is necessary for the Milky Way population of the GCRs is :

$$L_{CR} = \frac{V_D \ \rho_E}{\tau_R} = 5 \times 10^{40} \frac{erg}{sec} \tag{1.5}$$

$$with \quad V_D = \pi R^2 d = \pi (15 Kpc)^2 (200 pc) \approx 4 \times 10^{66} cm^3 \tag{1.6}$$

$$\tau_R \approx 6 \times 10^6 year \tag{1.7}$$

$$\rho_E \approx 1eV \tag{1.8}$$

  where L_{CR} is the power of the GCRs, V_D is the volume of the galactic disk, τ_R is the residence time of the GCRs in the galaxy, and ρ_E is the local energy density of the cosmic rays. While an estimate of the power (kinetic energy component) released by an explosion of the SN of Type II is:

$$L_{SN} = freq \ M \ v^2 \approx 3 \times 10^{42} \frac{erg}{sec} \tag{1.9}$$

$$with \quad M = 10 M_\odot \tag{1.10}$$

$$v = 5 \times 10^8 \frac{cm}{sec} \tag{1.11}$$

$$freq = \frac{1}{30} year^{-1} \tag{1.12}$$

The comparison between L_{CR} and L_{SN} suggests that the power released by the SN explosion copes with the GCRs requirements.

- acceleration process;

  An *astrophysical accelerator* (see Fig.1.6) is a system with a suitable source of energy. The same system also transfers the energy to individual particles by means of the acceleration process. The efficiency of the acceleration process is a key parameter. The total amount of energy which the accelerator transfers to the particles is

  $$E_{Particles} = E_{Source} \times \epsilon_{Process} \tag{1.13}$$

  where E_{Source} is the energy available for the astrophysical accelerator and $\epsilon_{Process}$ is the efficiency of the acceleration process. Therefore too low efficiency would require higher E_{Source} to cope with the given $E_{Particles}$. In the SNR case:

  - the E_{Source} is the kinetic energy coming from the SN explosion;
  - the acceleration process is the Diffusive Shock Acceleration (DSA, described in Appendix A), an evolution of the Fermi acceleration process (efficiency in the order of 10 - 30% [15]).

  The efficiency of the DSA satisfies the GCRs requirements.

- energy spectrum

  The GCRs escape from the astrophysical accelerator with a given energy spectrum. After that the GCRs diffuse in the galaxy and the energy spectrum changes. After the diffusion changes the experiments at the Earth (ground based or balloon-satellite borne) provide us with the energy spectrum of the GCRs.

  The energy spectrum in output of the DSA is a power law with the spectral index of $\approx$ -2. When the changes for the diffusion in the galaxy are considered, it agrees with the energy spectrum of GCRs at the Earth (the differential flux has the form of a power law with spectral index of $\approx$ -2.7).

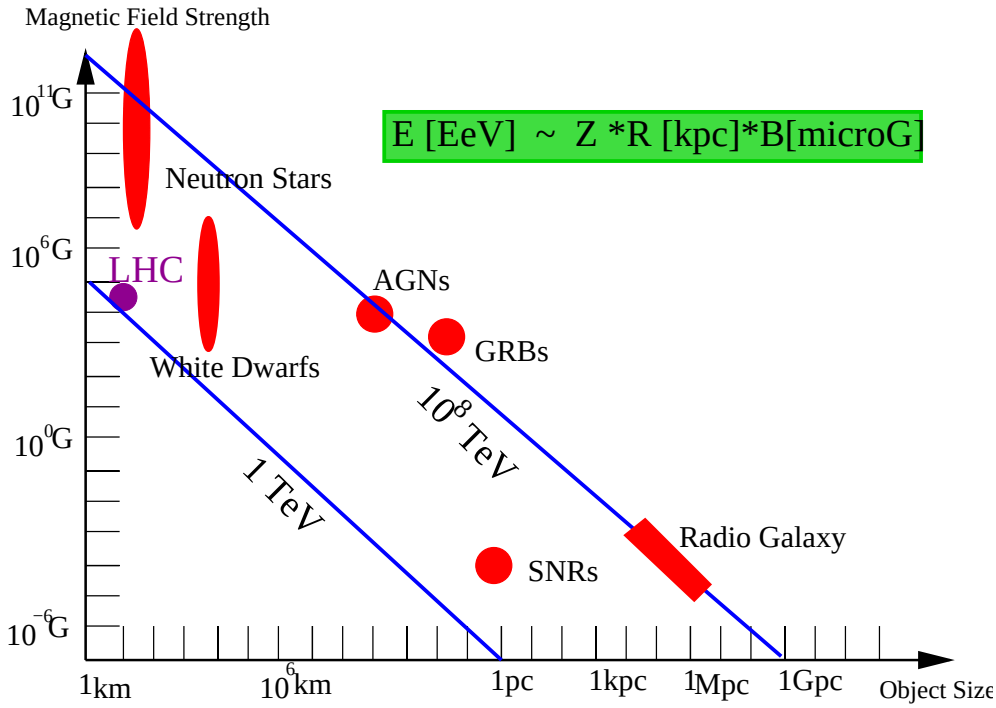

Figure 1.6: The so-called Hillas plot for the cosmic accelerators. In this plot the minimum strength of the magnetic field (B), needed to contain a charged particle inside an astrophysical object, is shown. The possible maximum energy is indicated with the blue lines and it can be calculated with the formula reported over the plot. A violet point represents the energy of the proton beam, which will be produced at the LHC accelerator

1.4 Very high energy γ rays from the SNRs

The hypothesis under study is: are the GCRs accelerated by the shock waves of the SNRs ? It is not possible, as it often happens in astrophysics, to test this hypothesis with a direct measurement. Instead it is possible to search for an indirect evidence. The very high energy γ rays can be the signature of very high energy charged particles. There are processes with which VHE electrons or nuclei emit γ rays. Because of these processes a given flux of VHE γ rays is expected from a source of GCRs. This flux is determinated, not only by the basic processes, but also by the configuration and physical conditions of the source. The basic emitting processes for γ rays [16] are :

- π_0 production, in hadronic interactions, and following decay

$$N + N_T \rightarrow \pi^0 x \tag{1.14}$$

$$\pi^0 \rightarrow \gamma\,\gamma \tag{1.15}$$

where N is a cosmic rays nucleus and N_T is a target nucleus of the interstellar medium (target nuclei located in the high density regions, will give more defined sources than the uniform medium), mainly H or He, π^0 is the neutral π meson (pion) of mass $\approx$ 134.97 MeV, x indicates the other reaction products. The π^0 is easily produced in hadron-hadron interactions, above the energy threshold of its rest mass. The π^0 decay is fast and the mean-life if in the order of $\Gamma \times 10^{-16}$ sec ($c\tau$ = 7.8045 m), where Γ is the Lorenz factor of the pion. A fraction of the energy of the primary VHE cosmic particle is transferred to the π^0. After the π^0 decay, this energy is carried out by the daughter γs. Under the hypothesis that SNRs are the GCRs accelerators, we have the following scenario:

- the cosmic rays (N) are recently accelerated by the shock waves of the SNRs. They escape from the accelerator and hit a target particle (N_T).
- the energy spectrum of the primary cosmic rays and that of the π^0 are dependent on the characteristics of the SNR.

- Inverse-Compton scattering

$$e\,\gamma' \rightarrow e'\,\gamma'' \tag{1.16}$$

where the energy of γ'' is higher than that of γ'. The Inverse-Compton scattering is a Quantum Electro-Dynamic (QED) process. This process consists of the scattering of a low energy photon and a high energy electron. After the interaction the photon gains energy. There are two regimes for the Inverse-Compton scattering :

- the Thomson regime, which describes the cases when $\Gamma \times \bar{E}(\gamma')$ is small compared to the rest mass of the electron ($m_e c^2$);
- the Klein-Nishina regime, which applies when the rest mass of the electron is small compared to $\Gamma \times \bar{E}(\gamma')$.

Regime	$\bar{E}(\gamma'')$	energy spectrum
Thomson	$\propto \bar{E}(\gamma')\ \Gamma^2$	$E(\gamma'')^{-\frac{(\alpha+1)}{2}}$
Klein-Nishina	$\propto \bar{E}(\gamma')$	$E(\gamma'')^{-\alpha}$

Table 1.2: The formulas for the Inverse-Compton scattering. $\bar{E}(\gamma)$ is the average energy of the photon, Γ is the Lorentz factor of the electron. The differential energy of the electrons is supposed to be $\propto E^{-\alpha}_{electron}$, where α is the spectral index

where $\bar{E}(\gamma)$ is the average energy of the photon, Γ is the Lorentz factor of the electron. Some useful formulas referring to the Inverse-Compton scattering are given in table 1.2. Under the hypothesis that the electrons are accelerated in the SNR shocks:

- the electrons (e^-) escape from the SNR with the energy up to 10s of TeV.
- the electrons scatter the low energy photons of the CMBR (Cosmic Micro-Wave Background) or the local Infra-Red field.

- synchrotron radiation

  The synchrotron radiation is produced by the particles deflected by the magnetic field. The radiated photons have a frequency spectrum with a peak at:

$$\nu_c \ = \ \frac{2}{3}\Gamma^2 sin\theta \tag{1.17}$$

  where θ is the *pitch angle* between the particle trajectory and the direction of the magnetic field, $\nu_g = \frac{eB}{2\pi m_e}$ is the *gyration frequency*, Γ is the Lorenz factor of the particle and m_e is the mass of the radiating particle (in this case an electron). A useful formula for the energy of the synchrotron photons, radiated by electrons, is:

$$E_{h\nu} \ = \ 0.05 \ \ (\ \frac{E_e}{TeV})\ (\ \frac{B}{\mu G})\ \ (eV) \tag{1.18}$$

  .

  Electrons of 10s of TeV in a strong magnetic field (10s of μG) will produce X rays via synchrotron radiation. The synchrotron emission

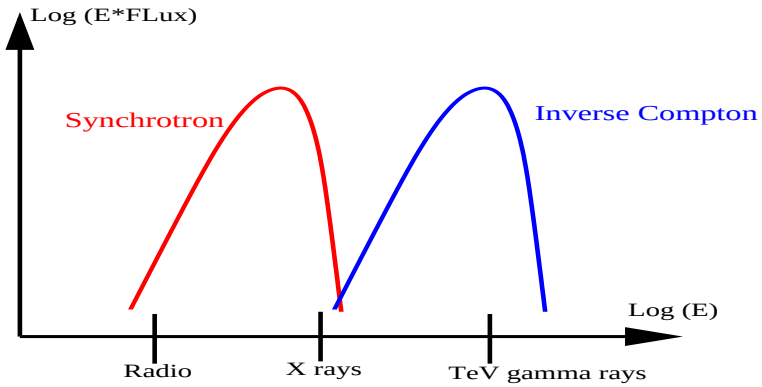

Figure 1.7: The so-called ϵF_ϵ plot, where is shown the photon flux multiplied by the photon energy versus the energy. The synchrotron emission (red curve) is generated by a population of energetic electron, which are deflected by a magnetic field. The synchrotron peak is a function of the electron energy. The Inverse Compton emission (blue curve) is also generated by the electron population, which scatters low energy photons.

provides information on the energy of the parent electrons, if the magnetic field is known. In the case of the SNRs, this energy is related to the magnetic field strength in the shell.

In an other case, the synchrotron emission produces the low energy photons (seed photons) which will be further up-scattered by the electrons via the Inverse Compton scattering (Synchrotron Self Compton model).

The so-called ϵF_ϵ plot is a useful tool to study the synchrotron and the Inverse Compton emissions (see Fig 1.7).

In order to verify our hypothesis on the GCRs, it is not sufficient to detect VHE γ rays from the SNRs. It is necessary to exclude any other possible phenomenon which produces VHE γ rays. Therefore we need detailed models of γ rays emission from the SNRs. These models have to provide information such as the flux of the VHE γ rays from a given SNR; or the characteristic energy spectrum of the γs produced by the GCRs. They can be classified as :

- *Leptonic* models, for which the γ rays are produced from the electrons by the Inverse-Compton scattering. These models have no big implication for the origin of the GCRs.

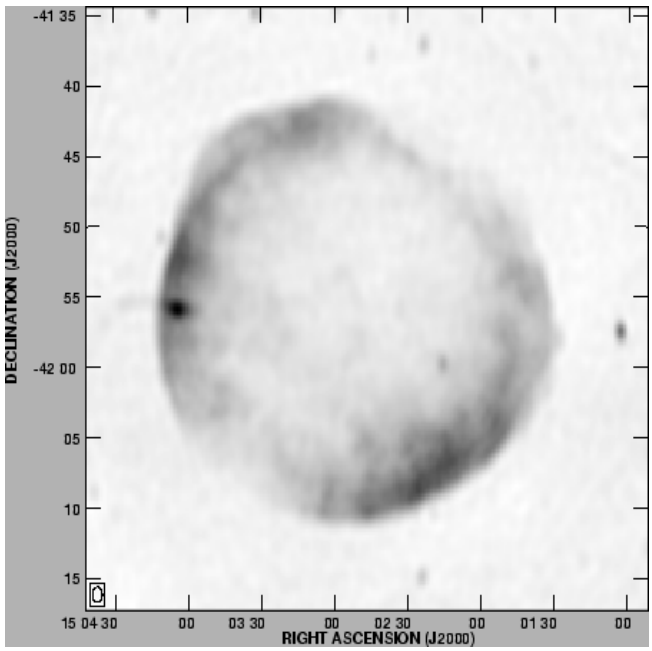

Figure 1.8: A Radio image of the remnant of the SN 1006; it is a typical Galactic Shell-type SNR (courtesy of ADIL; image code 98.BG.01.07). This 8-GHz image was made using the Molonglo Synthesis Radio Telescope (MOST). The brightened shell emission with a weaker emission projected against the center is clearly seen.

- *Hadronic* models, which consider a γ production by the decay of π^0, which are generated in hadronic interactions. They are directly connected with the GCRs study. An unambiguous proof would be the detection of νs from charged pion decay ($\pi^{\pm} \rightarrow \mu^{\pm}\nu_{\mu} \rightarrow e^{\pm}\nu_{\mu}\nu_{e}$).

The models of the γ rays emission from the SNR are reported in section 4.2, for the discussion of this thesis results.

1.5 The remnant of the SN 1006

The remnant of the SN 1006, (G327.6+14.6) has been created by the explosion of a historical Supernova. Because of this identification, the age of the remnant is very well known. This is essential for the understanding of the remnant properties.

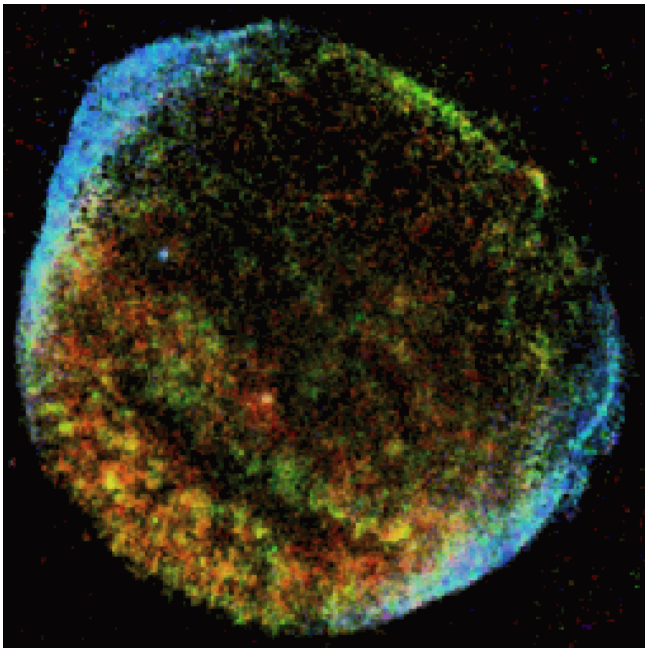

Figure 1.9: The image above shows a composite ROSAT HRI image of the remnant of the SN1006 displayed in false color derived from the ROSAT PSPC spectra. The blue colour represents non-thermal emission, and the red colour the thermal emission.

The remnant is much easier to be seen with the radio or in X rays observations rather than with the optical ones. The SNR optical spectrum consists only of Balmer hydrogen lines [17]. The shape of the remnant is circular, as it can be seen in Fig 1.9 and 1.8, with angular diameter of $\approx 0.5°$. The remnant radius is determinated to be 9.5 pc, under the assumption that the distance is 2.18 $\pm$ 0.08 Kpc [18]. The remnant is limb-brightened and it shows the North-East (NE) and South-West (SW) regions significantly brighter than the rest of the shell. Because of these two brighter poles, it is classified as a bipolar or a barrel-shape shell [18]. The NE part of the rim is the brightest part of the shell, emitting non-thermal X rays.

The SNR shell expands into a low density ISM with the velocity of 2890 $\pm$ 100 km/s [19]. This velocity is high if related to the age of the remnant. The SN 1006 was a type Ia SN, likely to have a white dwarf as a progenitor. Therefore the circum-stellar medium was not altered by the progenitor by means of stellar winds, as it would have been for more massive progenitors. The expansion velocity and the regular shape of the shell are consistent with

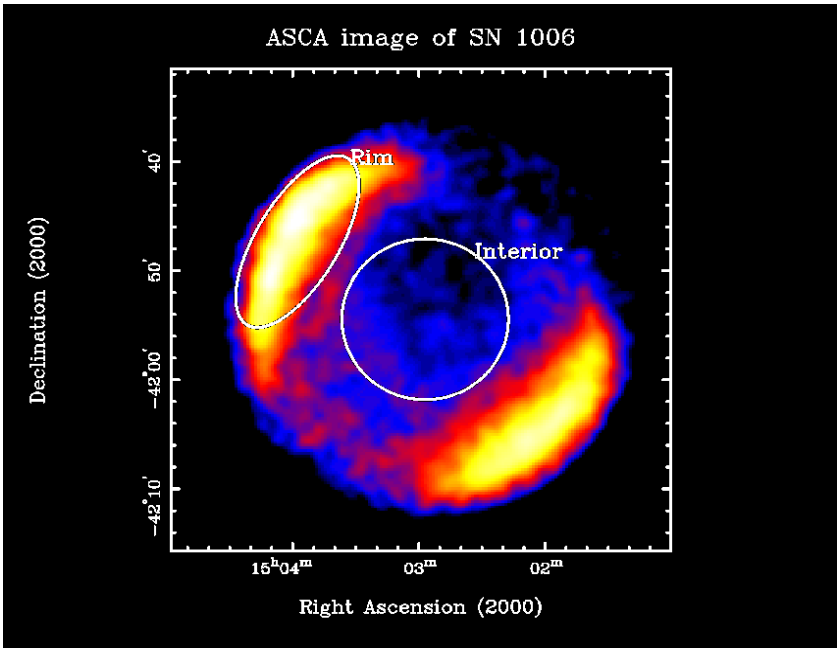

Figure 1.10: The SN1006 as seen by ASCA X ray satellite. The yellow and red colours are the non-thermal emission, and the blue colour the thermal emission.

a uniform low density environment.

A short summary of the main and of the most recent (published) observations of the SN1006 is given below.

- The remnant of the SN 1006 was discovered with radio observations in 1965 [20]. After the discovery this remnant was frequently observed at many different wave-lengths.
- In 1976 Winkler and Laird reported detection of X rays from the remnant of the SN 1006 [21]. The detection was performed using the data of the OSO-7 satellite and consisted of a thermal emission in the energy range of 1-10 KeV. The X rays satellites, which followed OSO-7, also detected the remnant. For example in 1980, the Einstein-Observatory produced a sky map of the X rays emission for this object [22].
- In 1995 non-thermal X rays emission was detected with the ASCA

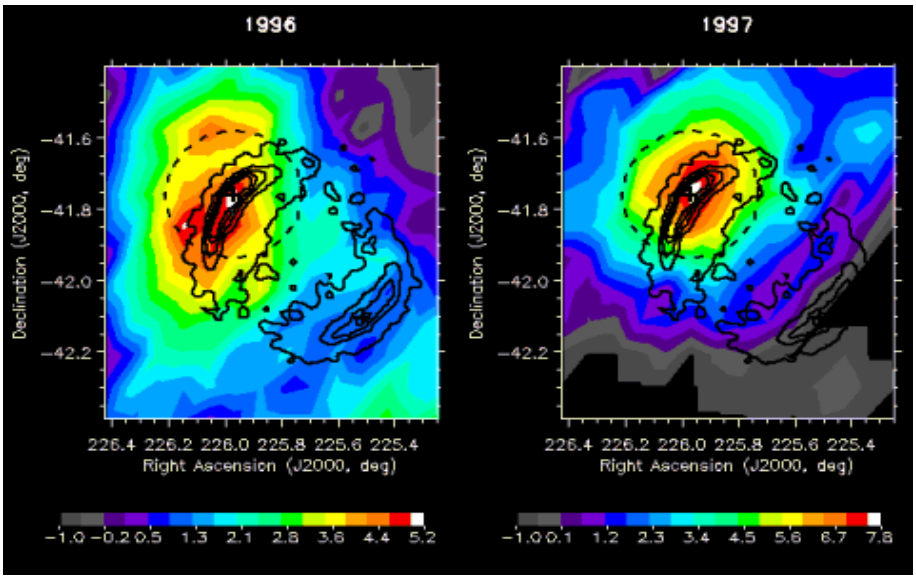

Figure 1.11: The significance sky map of the TeV γ rays detected by CANGAROO. White is the maximum significance, while blue and violet the minimum. Intensity of non-thermal X-rays (ASCA data) is shown by contour.

satellite (see Fig 1.10). ASCA was the first satellite to have CCD detectors, which allowed a more precise study of the X rays energy spectrum. The non-thermal emission was understood as synchrotron radiation of VHE electrons. The energy of these electrons was estimated to be in the order of 10s of TeV. This detection was published on NATURE [23] , with the claim to be the first evidence for shock acceleration of electrons in the SNRs.

- The ROSAT satellite also detected non-thermal X rays from the SN1006 [24].
- In 1998 the Cangaroo collaboration reported the detection of VHE γ rays from the NE part of the SN 1006 rim [25](see also Fig 1.11). The Cangaroo collaboration operated a 3.8m IACT (Imaging Air Cherenkov Telescope) based in Woomera (Australia). For this first detection the energy threshold of the detector was of 3.0$\pm$0.9 TeV. The VHE emission was considered to be Inverse-Compton scattering of the same VHE electrons which are responsible for the X rays synchrotron. After this first detection, the Cangaroo collaboration further observed

the remnant of SN1006 with larger IACTs (10 and 12m).

- Between the years 2000 and 2003, many new observations at various wave-lengths were published, for example the observations with the Beppo-SAX X rays satellite [26], new optical studies [27] and [19], and also studies of the SN1006 environment [28]
- In 2003 the SN1006 was observed with the Chandra [29] and XMM Newton satellites. The Chandra satellite has a very high resolution in imaging X rays sources. With these data it is possible to study very detailed structures of the SNR shell [30].
- In 2003 also the Integral satellite for γ rays was used to observe the SN1006. The Integral data are at this moment still not published.

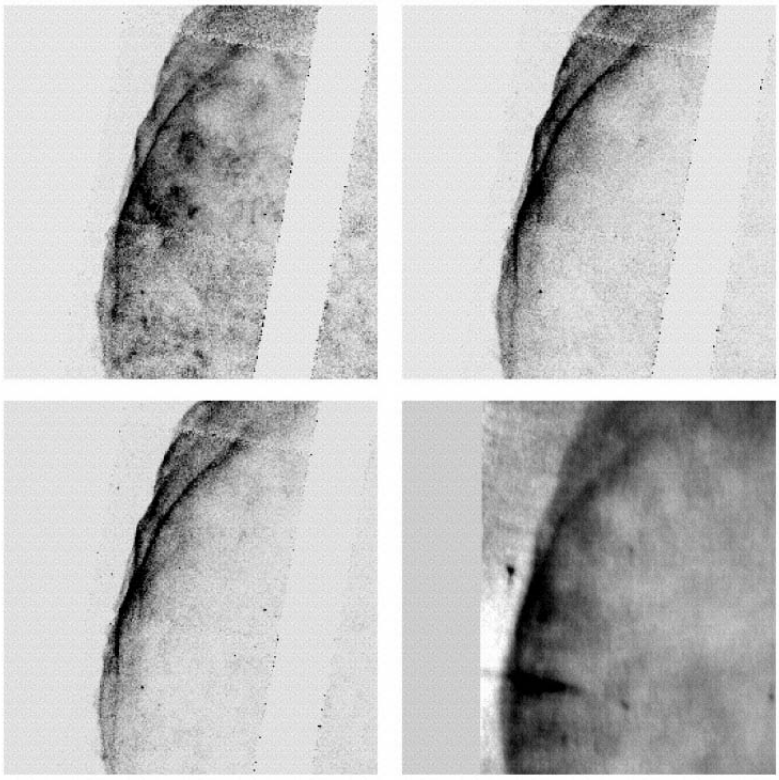

Figure 1.12: A composition of images of the North-East part of the SN1006 rim, from [29]. The four panels contain: the 0.5-0.8 KeV X rays image (top-left), the 0.8-1.2 KeV X rays image (top-right), the 1.2-2.0 KeV X rays image (bottom-left), a radio image (Reynolds et al., 1986, bottom-right). The X rays images are obtained with the Chandra satellite.

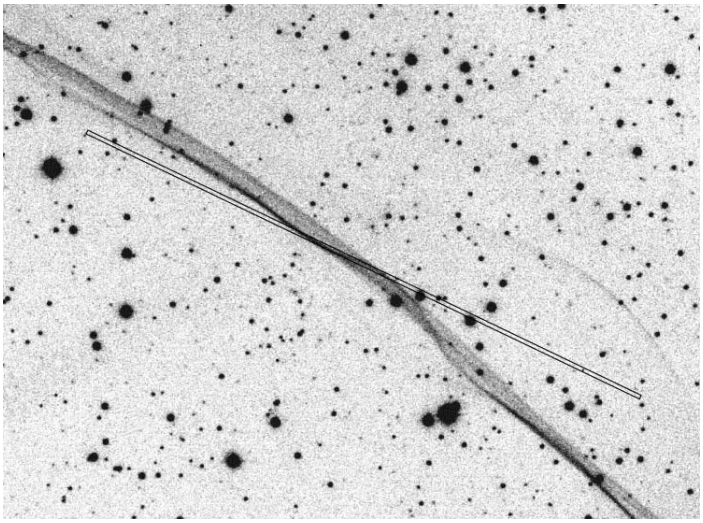

Figure 1.13: An image of the North-East part of the SN1006 rim, from [19] (the North is at the top; the east is to the left). It is possible to see a filament. This observation is obtained at the H_α wave-lengths.

Chapter 2

Imaging Atmospheric Cherenkov Telescope (IACT)

Air showers start with the interaction of a very high energy cosmic primary particle with a nucleus of the upper atmosphere. A short description of the distribution of the atmospheric matter is given in section 2.1. At the first interaction some secondary particles or photons (with various energies) are produced. They carry the energy of the primary cosmic particle. The secondary particles undergo subsequent interactions with atmospheric nuclei. Some produced particles may decay before interacting. Therefore many generations of secondary particles are generated, and number of produced particles increases fastly, giving rise to an *avalanche*. This avalanche multiplication (a shower or a cascade) stops when the particles are below a given critical energy and they do not produce new secondary particles. The types of interactions and the development of the shower is described in sections 2.2 and 2.3. Different types of interactions related to hadrons and γs produce different types of secondary particles and a different geometrical development of the shower. In this context the term *hadrons* is used as a collective name for protons and all the other cosmic nuclei, as well for mesons. Because of the Cherenkov emission (see section 2.4) charged particles with sufficient momentum, traversing the atmosphere, can radiate light. The Atmospheric Cherenkov Telescopes (ACTs) are suitable devices for the detection of the Cherenkov light produced by the air showers. The basic properties of the detector are introduced in section 2.5. A strong improvement of the ACT comes from the capability of resolving air shower images. A discussion of the image formation and the image parameterization is given in subsections 2.6, 2.6.1 and 2.6.2. The stand alone IACT HEGRA CT1 is described in section

2.7. This is an instrument which is used to perform the study I report in this thesis. Description of the CT1 is also meant to give an example of the structure of IACTs in general.

2.1 The Atmosphere

The atmosphere is the medium where the air showers develop. The atmospheric matter density follows an exponential distribution, decreasing with the altitude. Equations for pressure X and matter density ρ are given below:

$$X_h = X_0 e^{\frac{-h}{h_0}} \tag{2.1}$$

$$\rho = \frac{dX_h}{dh} \tag{2.2}$$

where X_0 is $\approx 1030\ \frac{g}{cm^2}$, ρ = matter density, h = altitude and h_0 is the height scale factor. The temperature plays some role in shaping the atmospheric gas. The atmospheric temperature decreases with the altitude up to the tropopause (12 - 16 Km), then also the height scale factor decreases, going from $h_0 = 8.4$ Km at the sea level to $h_0 = 6.4$ Km at 200 $\frac{g}{cm^2}$. From this first approximation we know, that the atmospheric depth (amount of matter along a vertical path, from a given altitude to higher limit of the atmosphere) at the sea level is equivalent to ≈ 27 electromagnetic interaction lengths (section 2.2) and ≈ 13 hadronic absorption lengths (section 2.3). The atmospheric depth is an integral value, it incorporates the information on the distribution of the atmospheric gas. It is a parameter, which for the study of the air showers, is much easier to handle than the altitude. The equation for the depth of an inclined path, going from the sea level to a point at a distance L and altitude h_p, is :

$$X_p = \int_L (\rho h_p)\ dl \tag{2.3}$$

$$h_p = Lcos\theta\ +\ \frac{1}{2}\frac{L^2}{R^2}\ sin^2\theta \tag{2.4}$$

where X_p is the depth, θ is the zenith angle and R is the Earth radius.

2.2 Electro-magnetic shower

In this section I shall describe the γ initiated showers, which are closely related to those produced by electron. These two types are collectively

called electro-magnetic showers. Photons and electrons of high energy are, because of their nature, very likely to interact with atmospheric nuclei with electro-magnetic processes. The most important processes are

- pair production $\gamma \rightarrow e^+e^-$
- Bremsstrahlung $e^\pm \rightarrow e^\pm\gamma$

Small contributions come from

- annihilation $e^+ e^- \rightarrow \gamma\ \gamma$
- Compton scattering (if $E_e << E_c$)
- photoproduction $\gamma N \rightarrow \gamma N^*, \quad N^* \rightarrow N\ h$

The *interaction length* is a useful quantity. An interaction length λ_{rad} (or more precisely the so-called *radiation length*) is the amount of matter which an electron should traverse in order to reduce the energy by a factor of $\frac{1}{e}$ due to the radiation loss only. The term length arises because for a given matter density λ_{rad} defines also a physical length. Another useful quantity is the *interaction length for pair production*, λ_{pair}:

$$\lambda_{pair} \approx \frac{9}{7}\ \lambda_{rad} \tag{2.5}$$

An electro-magnetic shower can be represented in a very simple picture. It is an ordered sequence of pair production of γ rays and Bremsstrahlung radiation of the electrons (positrons), as shown in Fig 2.1. Those processes cause a chain reaction, which basically stops, when the electrons energy is less than the critical energy $E_c \approx \frac{710MeV}{Z+0.92}$ (for gases). Electron energy loss, for energies below E_c, is more likely due to the ionization. The number of produced particles is 2^n at n^{th} step and has a maximum $n_{max}=\frac{E_0}{E_c}$. The depth of the shower maximum is $t_{max}=\frac{1}{ln(2)}\ \ln(\frac{E_0}{E_c})$, considering that, on average, there is one interaction for each interaction length $\lambda_{e.m.}$. The electro-magnetic showers are of compact structure (compared to the hadronic ones), because of the value of $\lambda_{e.m.} \approx 36\ \frac{g}{cm^2}$ of atmosphere. A parameterization of longitudinal electro-magnetic shower development (from [32]) is

$$\frac{dE}{dt} = E_0\ b\frac{bt^{a-1}e^{-bt}}{\Gamma(a)} \tag{2.6}$$

$$t_{max} = \frac{(a-1)}{b} = 1.0 \times (ln(\frac{E_0}{E_c}) + C_i) \quad , \quad i = e,\ \gamma \tag{2.7}$$

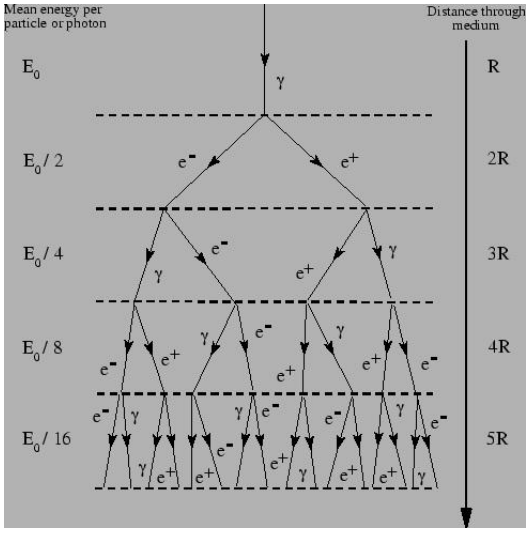

Figure 2.1: The so-called toy model of an electro-magnetic shower, adapted by [31]. The high energy γ produces an electron-positron pair. At second stage both the electron and the positron radiate a γ because of the Bremsstrahlung. The stages of pair production and Bremsstrahlung alternate and give rise to a shower of particles.

where $\frac{dE}{dt}$ is the energy loss in unit of $\lambda_{e.m.}$, a and b are parameters related to the medium in which the shower develops, C_γ= +0.5 and C_e= -0.5 . The opening angle in pair production, the bremsstrahlung radiation angle and the electrons multiple scattering are the cause for the transverse (lateral) development of an electro-magnetic shower. It is measured in terms of $Moliere\ \ radii$ ([32]), which are defined as

$$R_{Moliere} = \lambda_{rad} \frac{E_s}{E_c} \quad , E_s = 21.2MeV \tag{2.8}$$

In addition the earth magnetic field leads to same broadening of the shower. In the majority of cases, electrons and photons are the only types of particles produced in electro-magnetic showers. Other contributions could arise from photoproduction.

2.3 Hadronic cascade

In this section the hadronic cascade is introduced. The hadronic interactions are the most likely between the cosmic rays nuclei and those of the atmosphere. The energy carried by cosmic primaries is high enough to fragment nuclei or, depending on the interaction cross-sections and the mass products, to produce new hadronic particles. The most important processes for the hadronic cascade are :

- hadronic production

  $hN \rightarrow \pi, \kappa..., p(n), A, ...$

- subsequently the π^0 initiates an electro-magnetic sub-showers, while the charged mesons and the few nucleons initiate hadronic sub-showers.

  $\pi^0 \rightarrow \gamma\gamma$

- a small fraction of mesons can decay before interacting. An example of decay chains is the following, which leads to the production of μs and νs

  $\pi^{\pm} \rightarrow \mu^{\pm}\bar{\nu_\mu}(\nu_\mu); \quad \mu^{\pm} \rightarrow e^{\pm}\bar{\nu_e}\nu_\mu(\nu_e\bar{\nu_\mu}) \ ...$

Fluctuations play an important role for the hadronic cascades. Many final states of comparable likelihood are available at each interaction. Two primary cosmic hadrons of the same mass, charge and energy can produce different states already at the first interaction. At each step those two types of cascades can diverge in type of interactions, secondaries and energy distribution. Finally from the two equal primaries we can get two very different showers in the shape and particles output. The *hadronic absorption length* is an analogous of the interaction length for the hadrons. It is defined as the amount of matter which a hadron should traverse before undergoing an inelastic collision. The hadronic absorption length ($\approx 83 \ \frac{g}{cm^2}$) is more extended than the electro-magnetic interaction length. Therefore the hadronic cascade is longer (longitudinal development) than an electro-magnetic shower; in the atmosphere hadronic cascade develops at a lower altitude than an electro-magnetic shower of the same energy. Hadronic

cascade is irregular because particles production with a high transverse momentum can take place almost randomly during the cascade development. The hadronic cascades have, in general, a wider opening angle than the electro-magnetic showers.

The π_0 decay in two photons starts a pure electro-magnetic shower. It carries, on average, one third of the energy from each interaction. After few generations of hadronic interactions the majority of energy is gone into this electro-magnetic channel; i.e. the cascade ends when electrons energy is $< E_c$. With the productions of μ and ν a variable, but non-negligible, fraction of the energy is carried away from the shower. The μ is likely to survive and to strike the ground, because of its slow decay. The probability of interaction (along the vertical path in the atmosphere) for the ν is zero.

2.4 Cherenkov light emission

Many showers, expecially the electro-magnetic ones , develop completely in the atmosphere without any particles reaching the ground. In that case the atmosphere acts as a calorimeter which fully contains the event. Nevertheless, the light emissions provide information about showers. The showers radiate fluorescence and the Cherenkov light. The Cherenkov radiation is an electro-magnetic shock wave produced when a charged particle travels in a medium with a speed higher than the speed of light in that medium.

That particle radiates a coherent wavefront of conical shape, which is described by its opening angle (Fig. 2.2).

$$cos(\theta_C) \;=\; \frac{1}{\beta\; n(\nu)} \tag{2.9}$$

where θ_C is the cone opening angle, $\beta = \frac{v_{particle}}{c}$ and introduces a dependence on mass and energy of the particle, $n(\nu)$ is the medium refractive index which is function of the frequency of the electro-magnetic waves.

Previous formula implies :

1. The Cherenkov radiation is a threshold emission. The condition to have $\theta_C > 0$ implies that a β_{min} exists, below which there is no emission. This feature is largely used in particle physics to select different types of particles with Cherenkov detectors (see [33] or [34] for example).

2. The measurement of the Cherenkov angle gives a direct measurement of the particles speed.

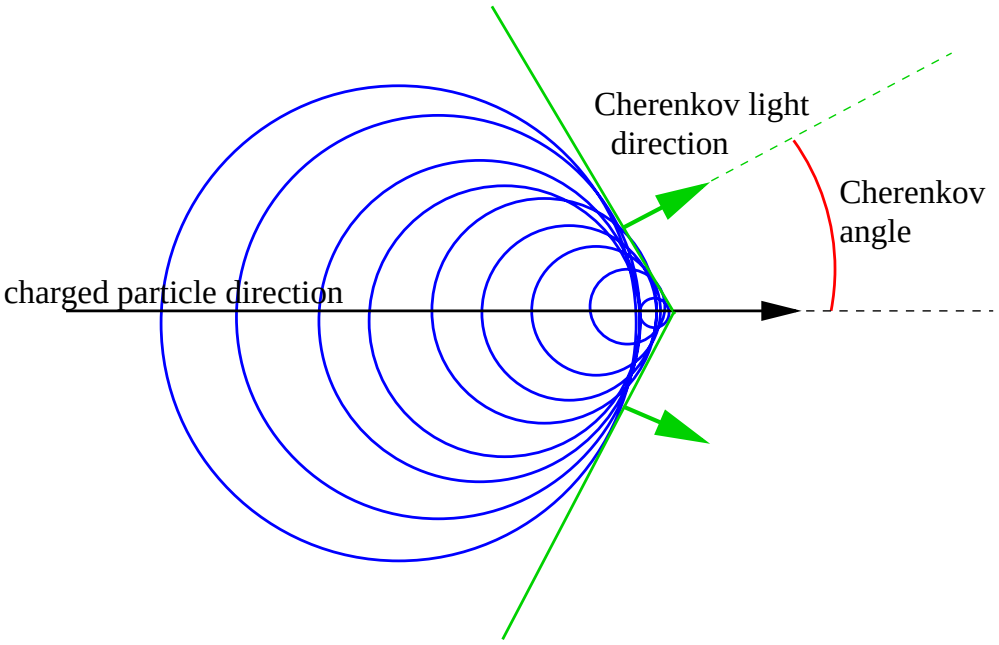

Figure 2.2: Cherenkov radiation. It is an electromagnetic shock wave. It is formed when the charged particle travels faster than the speed of light in the same medium. The direction of the charged particle is shown by the black arrow. The blue circles are the light front emitted at different times. They envelope to form a conical front. The orientation of this light front is shown by the green arrows. The Cherenkov opening angle Θ_C is indicated by the red arc.

3. There is a maximum Cherenkov angle $\theta_{C\ max}$ for particle with $\beta \approx 1$.

$$\theta_{C\ max} \ = \ arccos(\frac{1}{n(\nu)}) \tag{2.10}$$

The reliability of this radiation as an experimental tool depends on the total amount of emitted Cherenkov photons . The following relation holds in the typical range of sensitivity of photo-multipliers (between 350 to 550 nm), which are the usually used devices to detect Cherenkov light.

$$\frac{dN}{dx}(\lambda_1, \lambda_2) \ = \ 2\ \pi\ z^2\ \alpha\ sin^2\theta_C\ (\frac{1}{\lambda_2}\ -\ \frac{1}{\lambda_1}) \ = \ 475\ z^2\ sin^2\theta_C\ \frac{photons}{cm} \tag{2.11}$$

where N is the number of Cherenkov photons in the wave-length range from λ_1 to λ_2, z is the electro-magnetic charge of the particle, α is the fine-structure constant (it is a *running constant*, i.e. $\alpha \approx \frac{1}{137}$ at low energies, $\alpha \approx \frac{1}{128}$ at 80-100 GeV), θ_C is the Cherenkov angle.

In air showers the electrons are the most likely particles to emit the bulk of the Cherenkov light, followed by μs and light mesons, because of their masses and their number in a shower. In the case of the air shower particles, the radiation of Cherenkov light depends strongly on the structure of the atmosphere. The most important effect is the dependence of the refractive index of air on its density, and in turn on the altitude:

1. The Cherenkov energy threshold for electrons increases with the altitude ($\approx$ 20 MeV at the sea level vs $\approx$ 70 MeV at 20 Km) but the ratio $\frac{light\ yield}{length}$ decreases.

2. Also for other particles it is easier to radiate Cherenkov light when they are close to the sea level

3. The opening angle $\theta_{C\ max}$ is smaller at higher altitude.

Cherenkov light marks the direction of the radiating particle. In the air showers, the cone opening angle $\theta_{C\ max}$ gives a small uncertainty on the direction reconstruction. A bigger effect comes from the multiple Coulomb scattering of electrons, or other secondary particles, on the atmospheric gas. This scattering randomly deviates a particle from its original direction to another and the amplitude of the deviation depends on the particle energy. It can be parameterized as :

$$\Theta = \frac{13.6MeV}{\beta\ c\ p}\ z\sqrt{\frac{x}{\lambda_{e.m.}}}\ (1 + 0.038\ ln(\frac{x}{\lambda_{e.m.}})) \tag{2.12}$$

where p, βc and z are the momentum, velocity and charge number of the particle and $\frac{x}{\lambda_{e.m.}}$ is the thickness of the scattering medium. The multiple scattering Θ dominates over the Cherenkov opening angle θ_C for electrons at low energies.

In the atmosphere, Cherenkov photons, produced by the air showers undergo scattering and absorption processes (see [35]). As a consequence a fraction of photons and then of information is lost. The atmospheric molecules produce the Rayleigh scattering. This process acts between the electro-magnetic waves and electric dipoles with the dimension much smaller than the wavelength of light. A photons beam, traveling in a medium, along

a given direction, in presence of small dipoles (the Rayleigh condition), is attenuated in intensity :

$$I(x) \ = \ I_0 \ exp(\ -\alpha \ x) \ (n-1)^2 \quad , \alpha \ = \frac{k_0}{\lambda^4 \ \delta} \tag{2.13}$$

where I_0 is the initial (un-absorbed) intensity, I(x) is the intensity after light path x, $k_0 = \frac{32\pi^2}{3}$, λ is the wavelength of light, δ is the numeric density of dipoles. In the atmosphere the dependence from n (refractive index) translates in a dependence on the height, at which the Rayleigh scattering works. The scattering direction is given by :

$$\frac{d^2\delta_{ph}}{dx \ d\Omega} \ = \frac{3}{16\pi} \frac{d\delta_{ph}}{dx} (1 + cos^2\phi) \tag{2.14}$$

where Ω is the solid angle, δ_{ph} is the numeric density of photons and ϕ the polar angle.

The Rayleigh scattering is strongly dependent on the wavelength. It is dominant in the case of a clean atmosphere. Mie scattering is given by the bodies of size comparable with the wavelength of light. This process has a strong dependence on the scattering angle. The backscattering cross-section, for isotropic dielectric spheres, is

$$\sigma_{Mie} \ = (\frac{2\pi r}{\lambda})^4 \ r^2 \ (\frac{n^2-1}{n^2+1}) \tag{2.15}$$

where r is the radius of the scattering bodies, λ is the light wavelength, n is the refraction index.

In the atmosphere the Mie scattering is produced by aerosol which includes dust, water (as drops or small crystals), etc. This type of effect is sensitive to the atmospheric condition and composition, and the density of aerosol. Mie scattering is not fully understood. During clear nights the contribution of Mie scattering is less than that of Rayleigh scattering on the La Palma site.

The ozone (O_3), which is concentrated between 12 and 28 Km a.s.l., strongly absorbs the UV light below $\approx$ 300nm. The effect limits the wavelength range of Cherenkov light detectable from air showers.

2.5 Atmospheric Cherenkov Telescope

A proper photo-detector is the basic device needed to build an active calorimeter for the cosmic rays in the energy range from few 100s of GeV to few

100s of TeV. That is because the atmosphere acts as a radiator while the Cherenkov light propagates information about those showers which do not arrive at the ground. The photo-detector tasks are:

- to measure the Cherenkov light produced by the air showers;
- to provide information, in order to reconstruct approximately the geometry of each shower.

A suitable set-up is an optical reflector coupled to a camera of photomultiplier tubes (PMs). This device is named Atmospheric Cherenkov Telescope (ACT). In the following passages the basic properties of this set-up are described. A large sensitive surface is needed in order to collect as many Cherenkov photons as possible. But there are sources of light background which mix with light coming from the air showers. This background is not negligible and makes the measurement difficult . During dark nights Night Sky Background (NSB) light is at the level of 2×10^{12} $\frac{photons}{m^2\ sec\ sterad}$ ([36])in the wavelength range from 300 to 550 nm.

Part of the NSB is composed of the fluorescence emission of the, excited during the day, atmospheric gas molecules; the other component is the backscattered radiation coming from the ground. Light coming from bright stars and the moonlight also has to be considered. The number of photons of the NSB collected by each PM, within the integration time necessary to collect the Cherenkov signal, is small. Then the Poisson statistics can be used, in order to deal with the NSB counts. For the Poisson fluctuations dominated background (N) and for the shower signal (S) it holds (see also [37]):

$$\delta N \ \propto \sqrt{\Theta\ A\ \tau\ \eta\ \phi} \tag{2.16}$$

$$S \ \propto (\eta\ A) \tag{2.17}$$

where Θ is the solid angle acceptance of the detector, A is the collecting surface, τ is the integration time, η is the detector efficiency, ϕ is the flux of the background (NSB and other). There are two main factors which ACT exploits to enhance the signal coming from the showers :

- An optical reflector can be built as a composite surface and it can be extended in the order of 10s of m^2 (in the order of 100s of m^2 for next generation reflectors).

- A good quantum efficiency (typical of 20%) and a proper choice of the operating wave-length window.

The factors minimizing the NSB are:

- a narrow Field of View (FOV) of few 10s of deg^2, which contributes in defining the geometric acceptance;
- a very fast operational mode of photo-multipliers and the electronic chain, in the order of 10s of nsec. The light produced by the air shower is concentrated into a time window of few 10s of nsec. while the NSB is steady.

An important parameter in the design of this device is the minimum energy E_{th} needed for the detection of a shower on the top of the background (*energy threshold*):

$$E_{th} \propto \left(\frac{\delta N}{S}\right) \propto \sqrt{\left(\frac{\Theta\ \tau\ \phi}{A\ \eta}\right)} \tag{2.18}$$

As we will see later, a much higher signal then few times $\sqrt{NSB}$ is needed, in order to distinguish γ from hadron events. An ACT should be able to collect light from a shower at 10 - 20 km a.s.l, with an angular spread in direction of light rays of more than 2° at least. Air showers develop along direction of the primary cosmic rays (shower axis). The light yield of Cherenkov photons has, in first order, polar symmetry around the shower axis, therefore we consider a radial behavior (lateral distribution of Cherenkov photons). This distribution is almost flat for an electro-magnetic shower of not too high energies. The light-pool extends up to about 130m. The light produced between 7 and 20 Km a.s.l. is projected at the radius range from 120 to 130 meters ([37]). It is because of the change in the refractive index, that produces an *hump* in the light yield. At very high energy (few 10s of TeV) the light pool intensity varies strongly with the impact parameter. Hadronic showers develop deeper into the atmosphere, they do not show flat regime and have no *hump* in their lateral distribution of Cherenkov photons.

The effective collection area (A_{eff}) is the surface equivalent from which an ACT can detect enough photons with the right direction from a shower. The A_{eff} depends on the lateral distribution of Cherenkov photons, shower core altitude and distance. For an ACT, as designed above, its value is in the order of 10s of thousands of m^2. As mentioned before, hadronic and electro-magnetic air showers have different lateral distribution of Cherenkov

photons, which implies a different effective collection areas for those two different types of particles. From this difference we can calculate the minimum detectable flux of the γ showers on the top of a dominant background of hadronic:

$$N_\gamma \propto \Big(\frac{A_\gamma \sqrt{T}\ E^{0.8-G}}{\sqrt{A_h \Theta}}\Big) \tag{2.19}$$

where A_γ ,A_h are the effective collection areas for γs and hadrons, T is the total observation time, G is the integral emission power-law exponent of a given γ rays source.

2.6 Imaging technique

An ACT needs a camera capable of resolving shower images (i.e. a fine pixelized matrix of photo-sensors, at the focal plane), in order to distinguish between the γ and hadronic air showers exploiting the main differences:

1. γ rays are radiated usually by discrete sources, while cosmic rays at GeV - TeV energies are isotropic, when arriving at Earth. (DIRECTION)

2. Electro-magnetic showers and hadronic cascade are different in shape and project images with different features. (SHAPE)

Therefore the telescope camera should consist of few hundreds of photomultipliers (pixels), each covering $\approx 0.2^\circ$ in diameter. That allows to cover a FOV of some $\deg^2$ and to have a pixel size smaller than the average width of the shower image. Such camera makes the ACT become an Imaging ACT (IACT).

2.6.1 Image formation

The image shape depends not only on the shower shape but also on the relative orientation of the shower axis and the telescope axis. It is useful to define some quantities in order to describe such dependence. The impact point is the intersection of the shower axis with the plane, which is to tangent the telescope and perpendicular to the observation axis. The *Impact parameter* is the distance between the impact point and the telescope center (see Fig2.4). A shower with the axis parallel to the pointing axis of the telescope and very small impact parameter is the most simple configuration;

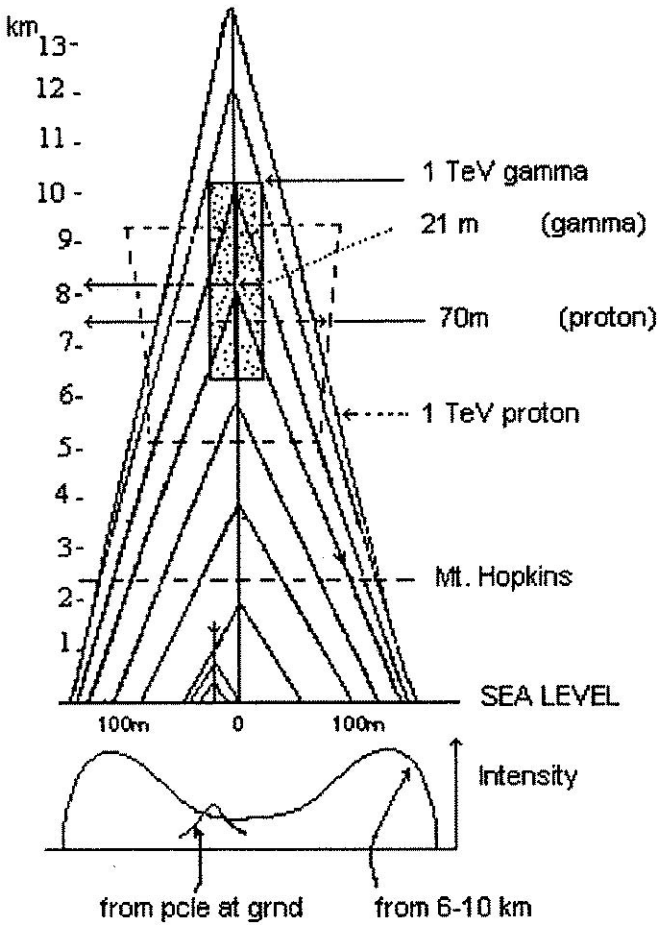

Figure 2.3: A geometric model of emission of Cherenkov radiation for the electro-magnetic and hadronic air showers (Hillas toy model,[37]). The core of a γ shower is enclosed by a small box. It is at altitude from 6 to 10 Km a.s.l., while the core of a hadronic shower is between 5 and 9 Km a.s.l. (here enclosed in a bigger box). The intensity profile is shown on the bottom. Light from 7 to 20 Km a.s.l is focused in correspondence of a radius of 120 - 130 meters from the center. The particles from the shower tail spread their Cherenkov emission on a large area.

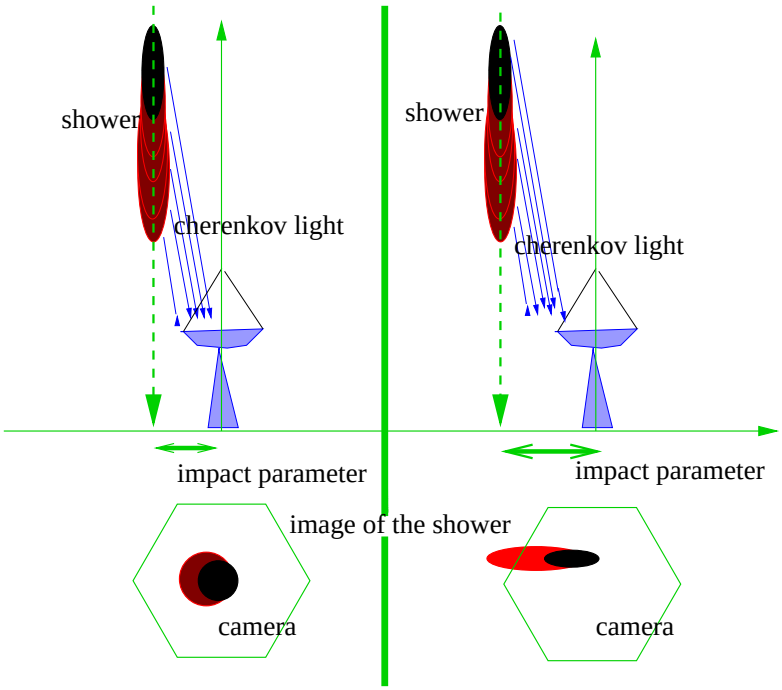

Figure 2.4: Image formation and Impact parameter. The Impact parameter is the distance between the telescope and the point at which the shower axis crosses the telescope plane. It is indicated by double green arrows. The larger is the Impact parameter, the more elongated is the image of the shower. The bottom of the shower (red in this illustration) is imaged closer to the camera center.

as it produces a circular image. A shower image becomes radially elongated as the impact parameter increases. It is because the telescope collects light from the side and not from the base of the shower. The image can be approximated by an ellipse. The upper part of the shower projects light closer to the center of the camera, while the lower part projects light closer to the edge. That is because the Cherenkov light produced at higher altitude has a smaller Cherenkov opening angle, then it is closer to the shower axis direction. The light produced at the base of the shower forms a wider angle in respect to the shower axis. Therefore the major axis of the ellipse is related to the longitudinal development of the shower, while the minor axis depends on the lateral development.

The major axis of the shower image always lies on a camera radial axis

when the shower axis and the pointing axis of the telescope are parallel. If the shower axis is not parallel to the pointing axis of the telescope , then the difference vector can be decomposed in two components:

1. A component along the radius (direction from the impact point to the detector) which can not be recorded by a single telescope and only affects the major axis of the image, with a decreasing effect;

2. An other component perpendicular to the first one, which produces a rotation of the shower image in the camera, then the image does not point to the camera center anymore; this miss-pointing is measured by the angular distance (*Alpha* parameter) from the ellipse major axis and the camera radius passing through the center of gravity of the image (see Fig. 2.5).

2.6.2 Image parameters

The informations about the air showers are extracted from their images. The analysis of the shower images uses a proper image parameterization (Hillas parameter [38]). The *image parameters* are defined on the light distribution in the camera plane. They consist of the 0^{th},1^{th},2^{th} order moments of the distributions, and other composed parameters. Before their calculation, a *cleaning* is performed in order to remove the light background component in the images. The most used parameters, in part in angular units, are :

- Size = the total integrated light content of the shower.
- Width = the rms spread of light along the minor axis of the image, i.e. a measurement of the lateral development of the shower.
- Length = the rms spread of light along the major axis of the image, i.e. a measurement of the longitudinal development of the shower.
- Distance = the distance from the centroid of the image to the center of the field of view of the camera.
- Miss = the perpendicular distance between the major axis of the image and the FOV center.
- Alpha = a derived parameter; $\alpha = \sin^{-1}(\frac{miss}{distance})$, i.e. a measurement of the shower axis orientation.
- Conc = the degree of light concentration as a ratio between two largest pixel signals and the Size parameter.

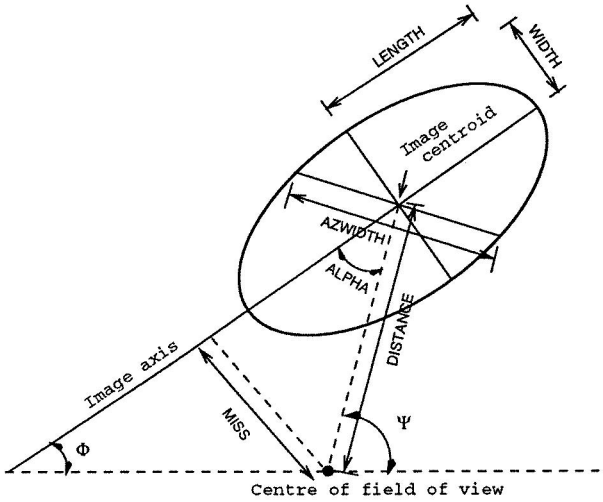

Figure 2.5: Shower image parameters based on a moment analysis. The image is approximated by an ellipse where the semi-major and semi-minor axes reflect the length and the width parameters and represent the shape of the captured image. The alpha, miss and azwidth parameters relate to the orientation or "pointing" of the image. The distance parameter is a measure of the image centroid from the center of the camera FOV

The other parameters are :

- Leakage = the fraction of leakage of the shower image out of the camera.
- Asym = a measure of how asymmetric the image is; a γ ray images have tails which preferentially point away from the source position.

2.7 HEGRA CT1 as an example of an IACT

HEGRA CT1 is an example of a stand alone IACT. Here I shall describe this telescope showing a practical realization of the concepts exposed in the previous sections. Main components of the CT1 are divided in four sectors:

- optics
- camera
- read-out electronics (trigger and data acquisition)

- mounting and tracking system

2.7.1 Optics

The optics is composed of the reflector and the so-called Winston cones (i.e.light concentrators in front of the PMs). The CT1 reflector is $10m^2$ large, and is made by 33 aluminum hexagonal mirror segments. The mirrors have diamond-milled surfaces of spherical shape with the radius of 9.8 m. They are arranged in the Davis-Cotton spherical design, which offers a uniform spot size also at the edge of the FOV, (in contrast to a parabolic design which is isochronous but introduces more aberrations). The reflectivity is $\approx$ 80%. In order to avoid ice deposition and water condensation, each mirror contains an heating system.

In previous configuration the reflector size was $5m^2$, made of 18 aluminized glass mirrors, with SiO_2 coating.

In front of the camera a 1mm UV transmitting foil is placed; it protects the camera from the intrusion of dust and water. There are Winston cones on the back of this foil. Each photomultiplier (PM) is coupled to a cone. Those cones are used as light concentrators and also as a shield against large angle stray lights.

2.7.2 Camera

The photo-detection and electronics devices are the camera, signal transmission, trigger and the readout electronics modules. The CT1 camera is composed by 127 photo-multipliers tube (PMs). In the optical system of the CT1 each pixel (a PM) covers an angular region of 0.244° of diameter. PMs are EMI 9083A of 21 mm of diameter, with photocathode quantum efficiency of 26% at 375 nm. They are 10-stage type and work at medium gain using only 8 stages to prevent high levels of anode currents induced by NSB. This operational mode allows to reduce the effects of the long time exposure to NSB light and to perform observations during moderate moonlight time. PM output signal is read both in current (slow) and in voltage (fast pulses). The voltage signal goes through a fast pre-amplifier, with an amplification factor of 10. Data transmission uses coaxial cables.

2.7.3 Trigger and Data Acquisition

Trigger logic requires :

- a voltage level threshold of 50 mV, which is equivalent to approximately 13 photo-electrons (LEVEL);
- at least two neighbouring pixels over threshold in a time window of 6 nsec (TOPOLOGY);

in order to accept the event. The use of the topology conditions allows to reject a large quantity of "false events" generated randomly by the NSB light fluctuations.

For each accepted event the pixels output signals are digitized using a Le Croy 2249 charge sensitive 12 bit Q-ADC. The signal is integrated for 30 nsec (ADC-gate width). After the event acquisition the system is inhibited in order to avoid pile up of the signal from different events.

Data acquisition modules are placed in crates and controlled by two WIENER CC 16 units. Those are linked to a 300MHz PENTIUM II processor based computer using two PC16-TURBO ISA cards. The DAQ system works up to event trigger rate of $\approx$ 70 Hz with a stable performance.

2.7.4 Mounting and tracking system

The CT1 has an equatorial mounting which is simpler than the alternative alt-azimuth mounting. An equatorial mounting has two axes, of which one is parallel to Earth rotation axis (hour angle). The telescope rotates at a constant angular velocity around this axis to point at its target. The other axis is used to follow the elevation (declination) of the target above the horizon. On the case of an equatorial mounting there is no rotation of the field of view around the tracked sky position, as instead for alt-azimuth. The equatorial mounting requires a heavy counterweight, in the case of the CT1 a counterweight of 6 tons. The telescope motion is obtained by stepping motors while the tracking control uses 14 bits Gray code shaft encoders. The accuracy in tracking is at the level of 0.04°. A software off-line tracking correction is applied, in order to remove small polar axis and bending effects.

Figure 2.6: The HEGRA CT1 stand alone IACT. The CT1 is located in La Palma, Canary Islands (28.75° N, 17.9° W, 2225m. a.s.l.), at the ORM (Observatorio Del Roque De Los Muchachos). Some other telescopes of the ORM are also visible in the picture. The ORM is one of the two observatories of the IAC (Instituto de Astrofisica Canarias).

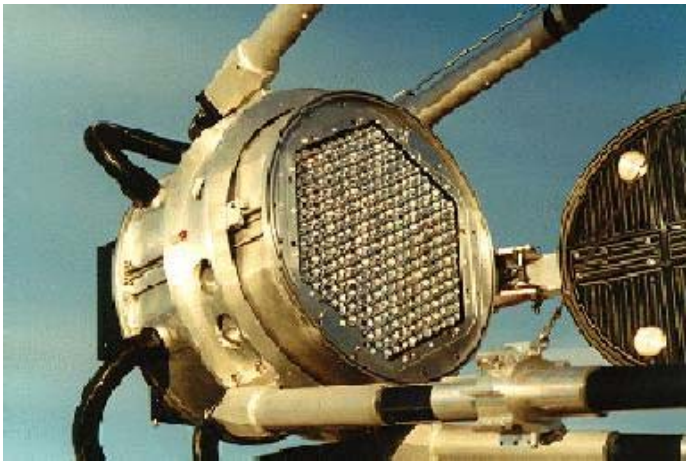

Figure 2.7: The CT1 camera. It contains 127 photo-multipliers EMI 9083A of 21 mm of diameter, with photocathode quantum efficiency of 26% at 375 nm. Each photo-multiplier covers an angular region, of hexagonal shape, with an effective diameter of 0.244°.

Chapter 3

Data analysis

In this chapter I report on the data analysis which had been used to obtain the final results.

The pre-processing and the filtering (section 3.1) are the first operations performed on the raw data. After these operations, it is possible to calculate the image parameters, which will be used to perform further stages of data analysis.

The set-up also provides the measurement of the anode current for each of the photo-multiplier tube (PM) of the camera. These measurements have been analyzed (section 3.2) and some bright stars in the field of view of the telescope have been detected. Those stars are used as position reference for the absolute pointing of the telescope and therefore they allow to check the tracking of the telescope.

A very important part of the data analysis for IACTs is the rejection of the dominant background of hadronic events. The methods for the rejection of the background are discussed is section 3.3. At first I describe the most often used method for the hadron rejection. In subsection 3.3.3 it is shown that the background rejection for small zenith angle is not effective at large zenith angle. Such problem affects the data analysis for this thesis because the remnant of SN1006 can be observed from La Palma only at a large zenith angle (> 70 °). Therefore it was necessary to develop a rejection method for large zenith angle observations. The method of finding selection cuts for large zenith angle is reported in the subsections 3.3.4 and 3.3.5. This selection method is illustrated in subsection 3.3.6, where the study of the efficiency is also shown.

The next part of the analysis consists of the search for off-axis sources (section 3.4). The SN remnant is an extended object, therefore the analysis

method should allow the search for a signal over the whole CT1 field of view. The so-called False Source Method ([39], [40], [41]) has been implemented for such a purpose. The FSM and its implementation are reported in subsection 3.4.2; while some tests with experimental data are in 3.4.3.

The following analysis step is the evaluation and suppression of the residual background (section 3.5). Two independent methods have been used, namely the *fit of the Alpha parameter distribution* and the *Ring background method*. They are respectively reported in sub-sections 3.5.1 and 3.5.2

In the last section of this chapter (3.6) are described the telescope calibrations: the effective collection area calculation, in subsection 3.6.2; and the Energy and Impact parameter reconstruction, in subsection 3.6.3.

3.1 Pre-processing and filtering of the events

The pre-processing and filtering procedure are the first operations after the data acquisition. They are also the first step for the data analysis, as can be seen in the Fig.3.1. At the pre-processing level, the data format are distributions of ADC counts (*raw data*) and other measurements. From these informations the showers images and then the image parameters will be obtained.

In the following subsection the main tasks and the methods used for the pre-processing and filtering are listed. They have been implemented in the standard analysis chain of the CT1 telescope. The same standard chain incorporates the procedure for extracting the image parameters from the data. The formulas used for the calculation of the image parameters (Hillas parameters) are listed in Appendix C.

3.1.1 Relative Gain

In the set-up of the CT1, a *channel* is a system made by a PM, the preamplifier and the cable needed to transmit the signals. The response of the channels of the camera to a fixed light intensity is not uniform. It is needed to know the relative gain of each channel in order to renormalize the contribution of the single pixels to the images. The measurement of the relative gain of the channels is obtained with the so-called laser-runs. During laser-runs the pixels are exposed to pulses of light coming from a single calibrating source. For each laser-run 100 measurements are acquired. The calibrating source in the set-up of the CT1 telescope were:

- initially a triggered nitrogen laser (337 nm). This device transmits

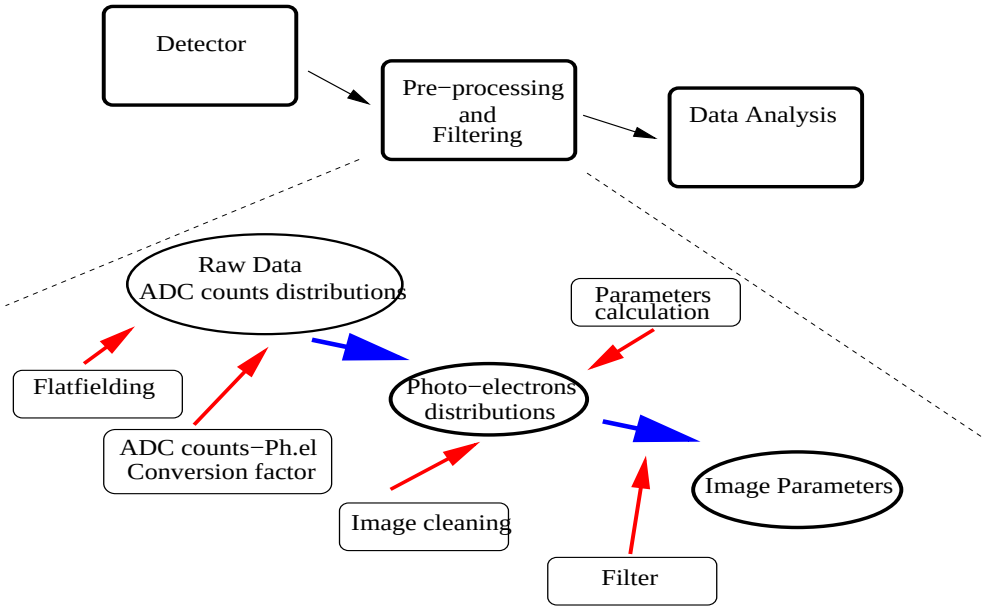

Figure 3.1: The scheme of the data flow and of the processes which are part of the pre-processing and filtering stage. The pre-processing is composed of : 1) the flat-fielding of the camera (relative gains); 2) the calculation of the ADC counts-to-Ph.el. conversion factor; 3) the image cleaning; 4) the parameters calculation. After these processes a filtering process is applied, to reject false or low quality events.

a short light flash, by means of an optical fiber to a small NE111 scintillator. The scintillator is in the center of the mirror dish, and is used in order to broaden the wave-length spectrum (peak at 390 nm). Because of its position the scintillator also diffuses the light uniformly over all the PMs.;

- in the second phase a LED light pulser substituted the laser.

The estimate of the relative gains is obtained by comparing the response of single channels to the average of the responses.

$$< M_i^{ADCc} > = \frac{1}{100} \sum_j^{100} (M_{i,j}^{ADCc} - PED_{i,j}^{ADCc}) \qquad (3.1)$$

$$G_i = \frac{M_i^{ADCc}}{\frac{1}{127}\sum_j^{127} M_{i,j}^{ADCc}} \quad (3.2)$$

where $M_{i,j}^{ADCc}$ is the measurement of the calibrating pulse jth by the PM ith, expressed in ADC counts; $PED_{i,j}^{ADCc}$ is the jth measurement of the pedestal of the PM ith, expressed in ADC counts; G_i is the relative gain of the PM ith.

3.1.2 Conversion factor from ADC counts to no. of photo-electrons

A channel signal corresponds to the intensity of light (number of photons) falling onto a PM. This light produces a number of photo-electrons at the photocathode. This number depends on the Quantum Efficiency of the photo-cathode. The photo-electrons are collected to the first dynode. The amplitude of the signal in output from the PM depends on the number of collected photo-electrons and is proportional the PM gain, which is a function of the HV in use. The signal in output from the PM is amplified and then digitalized by the qADC. Therefore the output of the channel is an integer number in units of ADC counts. This output can be converted to the absolute number of photo-electrons when the conversion factor (CF) is properly obtained. Such CF is dependent on the hardware attributes and operational parameters as well as on the time, because of the decreasing with time of the PM gain (*fatigue*). An estimate of CF can be obtained by measurement of fluctuations affecting a strong signal. This method is explained in [42]. The measurements performed during the laser-runs can be used for this method. One can calculate the CF with the following formula, under an assumption that the intensity of light pulses coming from the calibrating source is stable:

$$CF = \frac{N_{pulse}^{ph.el}}{< PS^{ADCc} >} = \frac{F^2 \times < PS^{ADCc} >}{\sigma^2_{PS^{ADCc}}} \quad (3.3)$$

where $N_{pulse}^{ph.el.}$ is the number of photo-electrons generated by a light pulse, $< PS >$ is the mean value for the distribution of the signal, expressed in ADC counts, $\sigma^2_{PS^{ADCc}}$ is the variance of the distribution of the signal also expressed in ADC counts, F is the so-called *specific excess noise factor* The F factor is a parameter constant in time, which relates to the quality of a PM. (a measurement for the PMs EMI 9083A used in the CT1 telescope gives F=1.09±0.05).

3.1.3 Night Sky Background (NSB) light

The PMs of the telescope collect background light added on the top of the Cherenkov light from the air showers. It is necessary to determine the level of this background light and, if possible, to subtract it from the data. The estimate of the NSB light intensity is obtained with the measurements of the pedestals of PMs. For CT1 an AC coupling (i.e. the mean value of the NSB is already subtracted) is used. The pedestal is a DC offset on the qADC input.

Pedestal are measured with dedicated pedestal-runs. During a pedestal-run the telescope is artificially triggered and 500 measurements are acquired. The number of photons collected by a single photomultiplier in 30 nsec is :

$$N = < I(NSB) > \times A_{mirror} \times \epsilon_{refl} \times \Theta_{pixel} \times \tau = \quad (3.4)$$

$$= 2 \times 10^{12} \frac{ph}{m^2 \ sec \ sterad} \times 10 m^2 \times 0.84 \times 2.1 \times 10^{-5} deg^2 \times 30 nsec = \quad (3.5)$$

$$= 1.06 \frac{ph}{nsec} \quad (3.6)$$

where <I(NSB)> is the average intensity of NSB light, A_{mirror} is the reflecting surface of the telescope mirror, Θ is the opening solid angle of a pixel, τ is the collection time . The number of *photo-electrons*, which are produced with collected photons in a PM, is $1.06 \frac{ph}{nsec}$ × Q.E. = 0.13 photo-electrons, where Q.E. is the average PM quantum efficiency ($\approx$ 12 %). The number of photons of the NSB collected by a PM is small and it follows a Poisson statistical distribution. Therefore one can obtain an estimate of the NSB light intensity by measuring the RMS or the distribution of pedestals.

$$\sigma PED^{ph.el_i} = \sigma PED_i^{ADCc} \times CF \times \frac{1}{G_i} \quad (3.7)$$

where σPED_i^{ADCc} is the RMS of the distribution of the pedestals, expressed in ADC counts, CF is the conversion factor from photo-electrons to ADC counts (which is dependent on the specific excess noise factor of the PMs), G_i is the relative gain of the pixel i^{th} and $\sigma PED^{ph.el_i}$ is the RMS of the distribution of the pedestals, expressed in photo-electrons. The above method works only in absence of electronic noise, or in case the electronic noise can be neglected, as it is considered for CT1.

A reference value for the CF of the CT1 is CF = 0.72±0.07 $\frac{Ph.el.}{ADCcounts}$, (for example see [43])

3.1.4 Image cleaning

The image cleaning is a procedure for subtracting the NSB noise component from the images of the air showers. The method used for the image cleaning with the standard analysis chain is so-called topological tail-cuts. It relies on the estimation of the NSB light intensity, as described in the previous section. The pixels having signals below a few σPED from the pedestals have significant probability to collect NSB photons only. Instead, the pixels above a threshold of some σPED have a significant probability of not being correlated with NSB, i.e. detect a genuine signal. Therefore the following procedure is applied:

1. All the pixels having signal above 3 σPED, and having a neighbour also above this threshold, are classified as *core* pixels. They are considered to be part of an image of the air shower.

2. All the pixels having signal above 2.5 σPED and below 3 σPED and having a neighbour core pixel are classified as *boundary* pixels.

3. All the pixels which are neither core nor boundary are further ignored.

3.1.5 Filter

The filtering procedure is applied in order to reject noise-induced triggers, not-usable events or of low quality. The filtering procedure consists of the application of a set of rejection conditions among which are :

- At least two pixels of the event should contain a signal higher than 13 ph.el. and they should be among the 91 pixels of the inner camera;

- showers with more than 92 core pixels are unlikely to be originated by compact Cherenkov image , therefore they are rejected;

- a minimum of 60 ph.el. per image is required, in order to reject not well defined events;

- the event trigger rate is an indicator of the stable atmospheric conditions and detector performances, then runs having an anomalous trigger rate (3-5 RMS above or below the mean rate) are rejected.

Further improvement of the data quality can be achieved. These methods are based on the use of the image parameters and are related to the techniques for the background rejection.

3.2 Stars as position reference

3.2.1 The pointing of the telescope

Cherenkov telescopes are simpler construction compared to the optical ones. Particularly at large zenith angle, mechanical deformations can result in mispointing. With optical telescopes the guide stars are used to cross-check the pointing accuracy. With Cherenkov telescopes this is not possible because of the lack of guide-γ sources. In order to study an unknown (point-like or extended) source, one needs to know the absolute pointing of the telescope with accuracy. The telescope pointing is used to relate the field of view of the telescope (having coordinate system CS_{FOV}) to a set of astronomic coordinates (CS_{sky}). The pointing of the CT1 is controlled by the tracking system. The same system provides the equatorial coordinates towards which the telescope is pointed with a precision of 0.1°. The telescope deformations (camera support bending) can introduce significant deviations. Such position corresponds to the center of the FOV of the telescope (position (0,0) of the CS_{FOV}). The CS_{FOV} is defined in the following way (see Fig 3.2) :

1. it is centered in the central position of the hexagonal camera, which is occupied by the pixel #1sp (the code *sp* means spiral counting, see Fig. 3.2);

2. the x axis is parallel both to the camera base and to the Right Ascension coordinate;

3. the y axis is parallel both to the camera height and to the Declination coordinate.

When large zenith angle observations are performed, there are two effects, that can be a source of errors in pointing the telescope.

- the deformation of the telescope frame;

- the principal CT1 axis may not point exactly to the north pole.

An alternative position reference is useful for cross-checking the telescope pointing and for the correction an eventual mispointing. The transformation from the CS_{FOV} (position over the camera plane) to the CS_{sky} (position in the sky) can be obtained, by means of the same reference. Bright stars in the FOV can be used as position reference. They can be detected by means of the PMs DC currents.

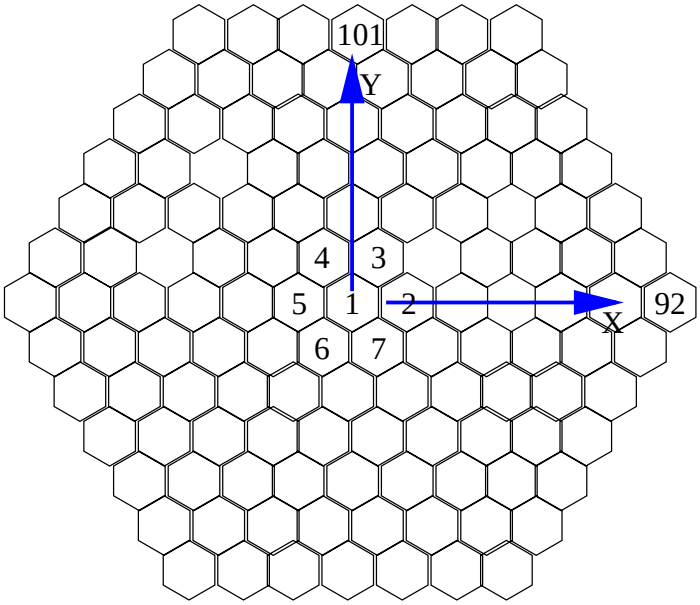

Figure 3.2: The CT1 camera and the CS_{FOV} (coordinate system of the field of view). The CS_{FOV} is an orthogonal coordinate system. It is defined in the following way: it is centered in the central position of the hexagonal camera, which is occupied by the pixel #1sp. The x axis goes from the pixel #1sp to the pixel #92sp and is parallel both to the camera base and to the Right Ascension coordinate. The y axis goes from pixel the #1sp to the pixel #101sp. The y axis is parallel both to the camera height and to the Declination coordinate. In order to describe the spiral numbering, the pixels from #2sp to #7sp (first ring) are shown.

3.2.2 Effects of the light of the stars

The signal coming from the PMs is integrated for $\approx$ 30 ns after a trigger. During this time-window PMs of the camera collect the Cherenkov light originated by the air showers. In the same time they also collect photons coming from various types of light backgrounds. One of these backgrounds are the stars. With the AC-coupling the steady source of background noise are suppressed. Only the fluctuations are influencing the light signal. The integration time-window is chosen in order to maximize the collection of Cherenkov photons from the air shower and to minimize the background. Therefore the telescope camera records only few photons coming from the stars. For measuring the starlight a separate circuit, monitoring the DC

anode current, is used. An effect of the star light is to produce a steady anode current output from the PMs. Then a PM, which collects light from a star, gives an anode current slightly higher than a PM which does not collect star light. One can obtain a map of the anode currents. It consists of a plot of the measurements of the currents versus the PMs positions. In this type of map each detectable star produces an hot spot of anode currents, which deviates significantly from the rest of the anode currents measurements. Then the anode current map can be compared to a detailed sky map of bright stars. The precision of the method is limited by the coarse grain of the camera pixel (0.24° in diameter). The knowledge of the position of the same stars in the CS_{FOV} (position in the camera, by means of the anode currents map) and in the and CS_{sky} (position in the sky, with a sky map) allows one to relate the CS_{FOV} to the CS_{sky} directly. I applied this method to the CT1 data for the analysis discussed in this thesis.

I shall discuss another effect, briefly, in order to complete the description of the effects of star light. The light of stars also affects the telescope trigger. This effect is not related to the search for a position reference. A PM (camera pixel) has an higher probability to be above the threshold level and to contribute in triggering the detector if a bright star radiates the PM with light constantly. Only the light fluctuations ($> 2.166\ \frac{photo-electrons}{nsec}$) contribute to trigger the detector, because of the AC-coupling. We can have two different cases:

1. a single *hot* pixel.

   The effect of a single *hot* pixel is minimized by the trigger. A triggering event should satisfy a topology condition :

   (a) at least 2 PMs should have signal above the threshold level AND

   (b) these 2 PMs should be *neighbours*

   This condition decreases the probability for having the telescope triggered with the contribution of a single *hot* pixel (if such pixel is isolated). This trigger condition works also for some other sources of light background.

2. a star bright enough to radiate over a cluster of pixels.

   An example of a very bright star which radiates light over more than 1 pixel is ζ (zeta) Tauri. It is a binary system with the principal star being of magnitude 3, close to the Crab Nebula. The Crab is frequently

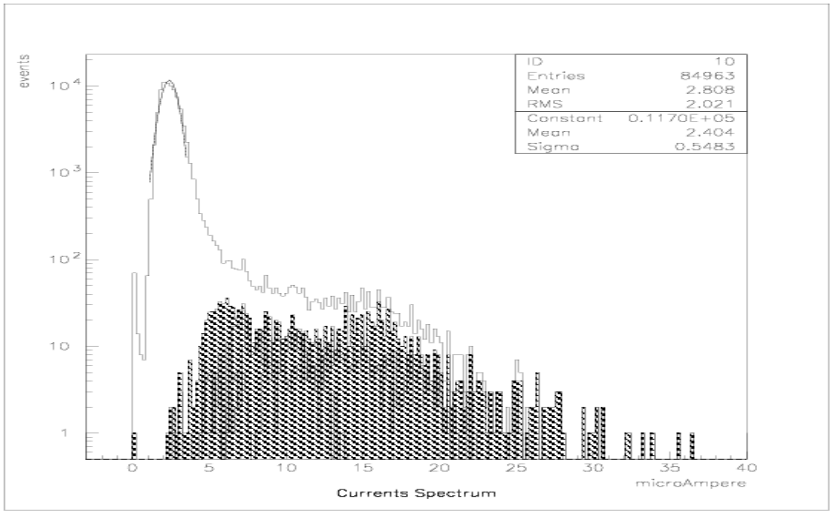

Figure 3.3: The spectrum of the anode currents, i.e. the distribution of the anode currents for all the pixels and runs used (entries per pixel). The measurements have: average value of 2.8 μAmp: distribution rms of 2 μAmp. A Gaussian fit of the measurements bulk gives: peak value of 2.4 μAmp; spread (FWHN:2.34) of 0.5 μAmp. There is a tail of high currents values. The shadowed histogram is the contribution of 4 pixels (#52, #30, #31 and #117). Individual current values fluctuate because of: small tracking error, wind-driven camera oscillations and atmospheric transmission changes.

observed because it is the *standard candle* for IACTs in the northern hemisphere. During these observations ζ Tauri radiates 2 or 3 pixels and increases considerably the trigger rate. A suitable method in this case is the exclusion from the trigger logic some of the over-irradiated pixels. During Crab observations with the CT1, one or two pixels, on average, are excluded from the trigger.

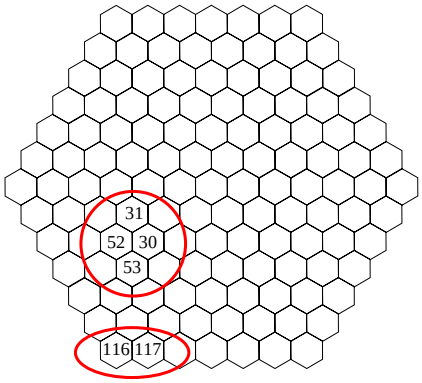

Figure 3.4: Positions of the pixels with the highest anode currents. The positions of pixels #31sp, #52sp, #30sp, #53sp, #117sp, #116sp are shown. These pixels have anode currents which deviate significantly from the rest of the measurements (pixel #53sp shows this behaviour only few times). They cluster around two positions.

Star	Position (IRCS2000)	Magnitude	Spectral Type
κ Centauri	RA=14:59:09, DEC=-42:06:15	3.13	B 2 IV
β Lupi	RA=14:58:31, DEC=-43:08:02	2.68	B 2 III

Table 3.1: Table of basic data of the brightest stars in the field of view of the CT1 telescope during the observations of SN1006 [44].

3.2.3 Anode currents data and their analysis

According to the standard mode of operating CT1, anode currents are measured 10 times a run (20 minutes on average) and stored in dedicated files (TelLog files). Therefore the bright steady light sources in the field of view of the telescope are sampled every 2 minutes. In this section I describe the analysis of the measurements of the anode currents, for the data taken during the SN1006 observations. Typical values for the anode currents are in the order of few μAmp. If bright stars are present in the field of view of the telescope then they should produce currents which deviate significantly from the bulk of the other measured currents. There are two bright stars in the field of view of the telescope during the observations of the SN 1006 (κ Cen and β Lup, see table 3.1) and one expects to detect them by the anode currents.

The *spectrum of the anode currents* (see Fig 3.3) is the distribution of the anode currents measurements for all the pixels and for all the runs used for the analysis. In this spectrum one can see that the measurements have an average value of 2.8 μAmp with an rms distribution of 2 μAmp. A Gaussian fit of the bulk of the measurement gives a peak value of 2.4 μAmp and a spread (FWHM:2.34) of 0.5 μAmp. In the same distribution one can see a tail of high currents values. Few pixels are responsible for such tail. In the shadowed histogram (see Fig 3.3) one can see contribution of 4 pixels (#52, #30, #31 and #117) to the spectrum of the anode currents. The measurements in this tail are :

- above 7.8 μAmp = (distribution average + 2.5 times the distribution rms).
- partially above 12.8 μAmp = (distribution average + 5 times the distribution rms).
- above 7.9 μAmp = (mean value of the *bulk g-fit* + 10 times the spread (sigma) of the fit) .

The pixels with the highest anode currents cluster around two position (see Fig 3.4). The spectrum of the anode currents and the configuration of the hot spots are consistent with the hypothesis that at least two bright stars are in the field of view of CT1.

A further analysis is needed in order to obtain, as precise as possible, the positions of these two candidate stars. I had searched for the contribution of anode currents produced by the candidate stars with the following procedure. At first I had calculated the mean value A.C.$_{i,t}$ of the distribution of currents (where i is the pixel number and t is the sub-sample under study). Then I subtracted the anode current $\overline{c.b._t}$ produced by the background light. In this context every source, which is not a star, is considered to be background. I assumed that:

1. the *c.b.* (currents background) is distributed randomly around an average value = $\overline{c.b._t}$;
2. $\overline{c.b._t}$ is equal to the mean value of the *bulk fit*, for each sub-sample t.

Then the contribution of the bright stars to the anode currents is

$$A.C._{star(i,t)} \;=\; A.C._{i,t} \;-\; \overline{c.b._t} \tag{3.8}$$

where $\overline{c.b._t}$ is an average contribution of the currents background, A.C.$_{i,t}$ are the raw measurements of anode currents, the index i runs over the pixel

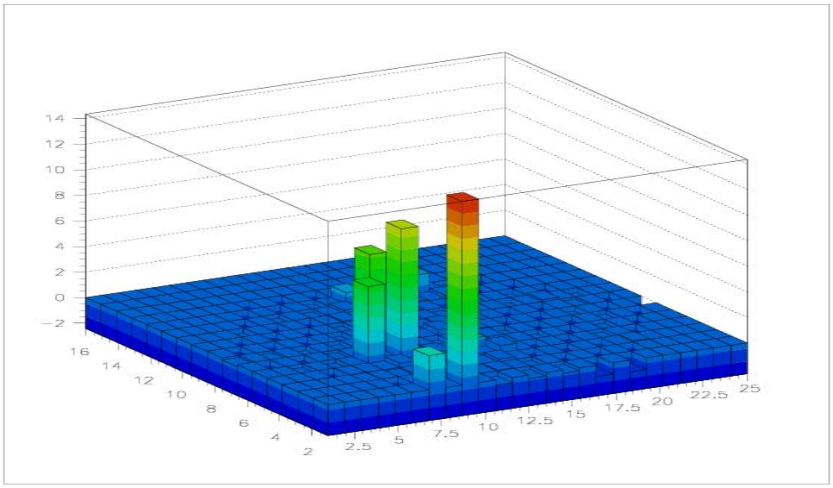

Figure 3.5: Map of the anode currents produced by bright stars. The x and y axis are the positions of the pixels (in arbitrary units) while the z axis is the anode current excess in μA. After the subtraction of the current background ($\overline{c.b.}_t$), the majority of the pixels are close to 0 μAmp. The two stars (κ Cen and β Lup) are clearly visible. (κ produces the three close columns, β produces the two columns at the edge of the plane). Some neighbour pixels, are not closely connected in this representation. This artefact comes from the projection of the hexagonal camera topology on a squared grid.

number i=1,...,127 while the index t runs over the sub-samples in which the data have been divided.

The next step is to study the 2 dimensional distribution of the light excess produced by the bright stars (A.C.$_{star(i,t)}$) over the camera plane. Because of the mirror imperfections. the point-like star image is *smeared* over a bell-shaped intensity distribution. The measurement of A.C.$_{star(i,t)}$ is associated with the center of the pixel i (see Fig 3.5). One has to consider that the pixels are of hexagonal shape. This geometry has some implications. The circular spot of light can cover a small fraction of the pixel, for example,

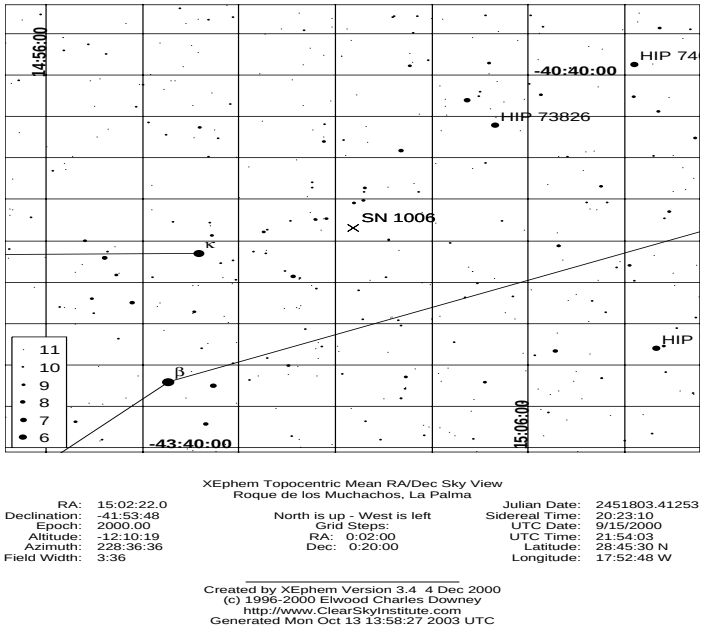

Figure 3.6: Sky map of the region of SN1006. The cross labelled as SN1006 points to the center of the SNR shell. The stars are indicated by the points, the star magnitude is indicated by the size of the points. The points labelled with β and κ point to the position of the stars β Lup and κ Cen. This sky map can be compared to the map of anode currents in Fig. 3.5.

one of the corners. Then light falling onto a small fraction of the pixel area is attributed to the whole pixel. If one applies the center of gravity method, the precision of the measurements can be improved both for the position and the spread of the light excess. An example of the distribution of the light excess $A.C._{star(i,t)}$ over the camera plane is shown in Fig 3.5. One of the candidate stars is close to the edge of the camera while the other candidate is closer to the center of the camera. The projections of the light excess distribution along the x and y axes are calculated , both for the regions of the edge and the central star candidate. A Gaussian fit is applied to the x and the y projections in order to obtain the mean position and the spread of

the distribution of light excess. A different method is used for the candidate star at the edge of the camera. Two pixels (#117sp and #116sp) are related to this candidate. Both pixels are in the same row therefore :

- the weighted mean of the light excess distribution (in the related region) is considered as the position of the candidate star along the x axis;
- the rms of the same light excess distribution is considered as uncertainty along the x axis;
- the central y position of the pixels #117sp and #116sp is considered as the position of the candidate star along the y axis;
- half diameter of a pixel is considered as uncertainty along the y axis.

The spectral type (then the emission spectrum) and the magnitude of β Lupi are similiar to those of κ Centauri (see magnitude of the star and spectral type in Tab 3.1). Therefore we expect to detect the same amount of light from the two stars (or better we expect more light from β Lupi). Instead the light detected from β Lupi is less than for κ Centauri. It is likely that only a fraction of the β Lupi light spot is intercepted by the camera, while a significant fraction is not detected (leakage, see the total current in Tab 3.3), because β Lupi is just at the edge of the field of view. The measurements of the positions of the two star candidates can be found in Tab. 3.2 and Tab. 3.3.

Epoch	ΔX	$\delta(\Delta X)$	ΔY	$\delta(\Delta Y)$	Total Current
4500-5000	-0.53	0.14	-0.40	0.10	23.0
5000-5500	-0.53	0.14	-0.42	0.10	22.5
5500-6000	-0.52	0.14	-0.42	0.12	22.5
9000-9500	-0.65	0.14	-0.47	0.10	32.0
9500-10000	-0.59	0.14	-0.50	0.10	32.0
10000-10500	-0.55	0.12	-0.50	0.12	29.0
10500-11000	-0.55	0.13	-0.50	0.12	28.0
13000-14000	-0.56	0.13	-0.47	0.12	25.0
14000-15000	-0.56	0.13	-0.5	0.12	26.0
all	-0.59	0.11	-0.47	0.12	28

Table 3.2: The position of the star κ Cen, measured with the anode currents. The data are divided epochs (the run number is used to assign the epoch); ΔX and ΔY are the coordinates of the star respect to the center of the CT1 camera; $\delta(\Delta X)$ and $\delta(\Delta Y)$ are the errors associated with ΔX and ΔY respectively. The excess of currents, which is associated with the star, is shown in the column *total current*

Epoch	ΔX	$\delta(\Delta X)$	ΔY	$\delta(\Delta Y)$	Total Current
4500-5000	-0.49	0.14	-1.49	0.12	16.0
5000-5500	-0.48	0.14			15.5
5500-6000	-0.48	0.14			15.0
9000-9500	-0.48	0.17			5.0
9500-10000	-0.48	0.17			7.0
10000-10500	-0.49	0.16			7.0
10500-11000	-0.49	0.14			10.0
13000-14000	-0.48	0.14			6.0
14000-15000	-0.49	0.14			7.5
all	-0.48	0.14			11

Table 3.3: The position of the star β Lup, measured with the anode currents. The format of the table is the same as in table 3.2. The best estimates for ΔY and $\delta(\Delta Y)$ are reported. They are affected by the partial leakage of the spot of the star light out of the camera edge.

3.3 Background rejection

3.3.1 Supercuts and the selection of the γ events

Nuclei are the main component of the cosmic rays. They generate a rate of showers at least two orders of magnitude higher than the rate of the gamma rays events. This ratio also holds for the observations of the strongest sources (for example Crab Nebula). One needs to suppress such dominant background in order to search for the γ rays signals. The Whipple Cherenkov telescope was the first detector allowing the detection of very high energy γ rays. The Whipple group used an effective method of background rejection in order to achieve their results ([45] and [46]). The method of selection used by the Whipple group is named *supercuts*. It has been widely used by many groups operating Cherenkov telescopes. In the following I describe the supercuts and their working principles.

The main principle of the supercuts is to reject the hadronic events and to retain the gamma candidates on the basis of the shape of the showers images. The image parameters (Hillas parameters, [38], see also Fig. 2.5) preserve a substantial fraction of the informations contained in the images. Therefore the criteria for the selection of the γ events can be expressed in the form of conditions over the image parameters. The word *cuts* refers to the definition of conditions as inequalities, for example:

$$A_{lower\ limit} < P_1 < B_{upper\ limit} \tag{3.9}$$

which means that an event is accepted only if the parameter P_1 calculated for such event has a value between a lower (A) and an upper (B) limit. The most important selection cuts are related to the *Width*, *Length* and *Dist* parameters. The supercuts also include a condition on the *Alpha* parameter, providing information on the incoming direction of the γ ray (or of the hadron, see section 2.6). The selection ranges of the supercuts and the distributions of the parameters for γs and the hadrons are shown in Fig. 3.7. Other cuts are made on other parameters (like *Size*, etc...). They are not considered as the basic version of supercuts, and in general they are less effective than the principal cuts.

The motivations for the selection conditions of the supercuts are the following:

- *Width* and *Length*: γ rays air shower are shorter (longitudinal development $\rightarrow$ Length), thinner (lateral development $\rightarrow$ Width) and more regular in shape than the hadronic events of the same energy

(see Fig.3.7). The distribution of Width and Length of the γ rays events has average value smaller than that for hadrons. Therefore the selection of *small* Width (or Length) retains a consistent fraction of the γ events and rejects many of the hadronic ones. In this context a *small* value means a value below the majority of the hadrons and (hopefully) above the majority of the γs. This selection works for showers of the same energy. The γ events of high energy could have the same extension of hadronic events of low energy, i.e. the cuts on Width and Length parameters need a small correction as function of the shower energy (the parameter Size is a reasonable approximation of the energy). That is because the Width and Length parameters are a slow-varying function of the energy (just to remind the longitudinal development of an electromagnetic shower is a linear function of the logarithm of the energy).

- *Dist*: the position of the center of gravity of the image in the camera (Dist) is used for two reasons:

  1. Dist is related to the impact parameter (the distance between the detector and the point where the axis of the air shower crosses the ground). Showers too close to the detector show only the shower tail (see Fig 2.3 and subsection 2.6.1). Therefore a minimum Dist is required.
  2. Events with a large Dist are unlikely to be contained into the camera plane. These events are truncated and they can not be correctly reconstructed. Therefore also a maximum Dist is required.

- *Size*: if too few photoelectrons are collected from a shower then the shower image is not well defined and the image parameters are measured with a poor precision. Then a threshold of the number of photoelectrons (Size) collected from a shower is required . Although the cut in Size is not included in the original supercuts a minimum size is implied by the trigger conditions and the image-cleaning process.

The supercuts are described in Tab 3.4. They are the same as in [45] but they include also a cut in Size. This cut in Size is used as standard with the data analysis of the CT1 telescope. It should be mentioned that the images change as function of the zenith angle, Impact and Size parameters. These changes have to be treated with advanced analysis. Then cuts dependent on zenith angle, Impact and Size parameters are required.

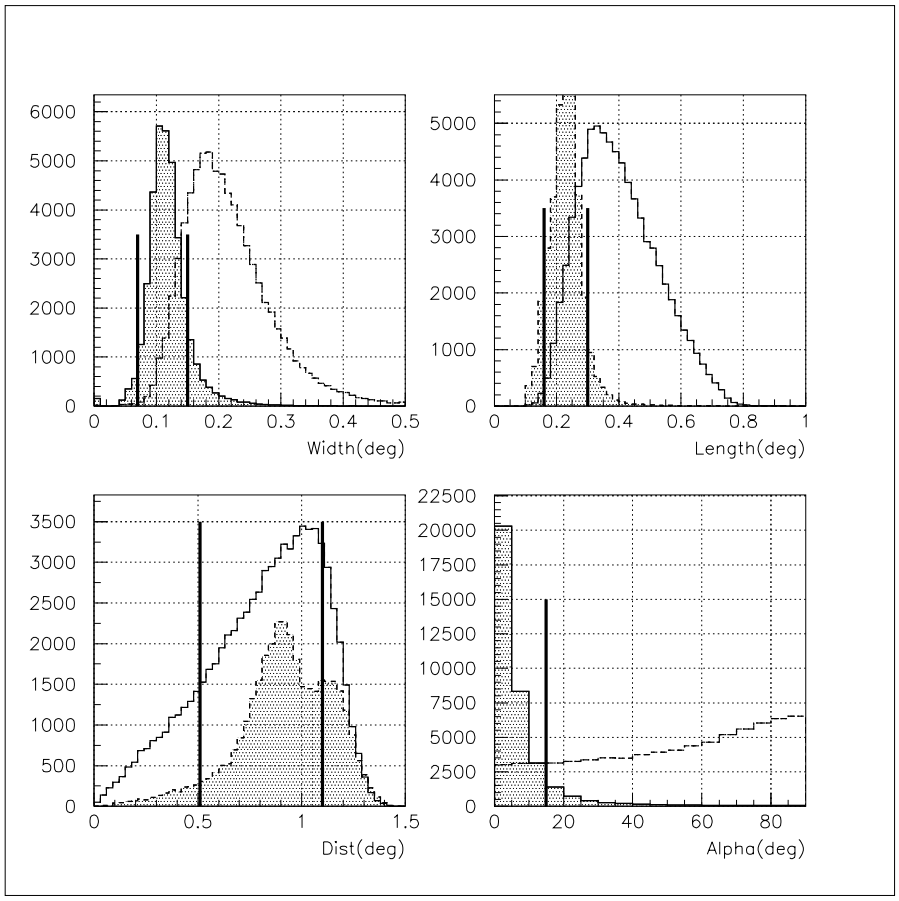

Figure 3.7: The distributions of the Width, Length, Dist and Alpha parameters (for a large zenith angle range). The shadowed histograms represent the MonteCarlo simulations of γ events. The white histograms represent the experimental hadron events (so-called OFF-data). The black vertical lines show the selection ranges of the supercuts.

lower limit	parameter	upper limit	unit
0.07	Width	0.15	degree
0.16	Length	0.3	degree
0.51	Dist	1.1	degree
60	Size		number of photo-electrons
	Alpha	15	degree

Table 3.4: The basic original supercuts. These cuts are used for low zenith angle samples.

3.3.2 Selection cuts for low zenith angle

The finding of a proper method for the rejection of the background is one of the most important steps for the analysis of the data of a Cherenkov telescope. The supercuts and other similar selection cuts can be tuned by choosing the proper lower and upper limits for the selection ranges. They can be tuned both for being applied to a given telescope or for being used to a special analysis. The tuning procedure is usually based on a training sample of MonteCarlo simulations or of experimental data. In this section one can see the performances of the supercuts on the data of the CT1. Although supercuts have been originally developed for the Whipple telescope they can be also used in a slightly modified form for the CT1 data. These selection cuts will be used as a reference for the improved selections which will be discussed further. The *Tlow* cuts are selection cuts derived from supercuts, for low zenith angle. The Tlow cuts are tighter than supercuts, and their performances will be evaluated. The Tlow cuts are described in the Tab. 3.5, they will be used as the base to develop the selection cuts for large zenith angle in the next sections.

The following quantities are useful in order to evaluate the effectiveness of the selection of the γ events and the rejection of the hadrons :

- *gamma efficiency* ϵ_γ

$$\epsilon_\gamma = \frac{N_\gamma(surviving)}{N_\gamma(total)} \tag{3.10}$$

- *hadron efficiency* ϵ_h

$$\epsilon_h = \frac{N_h(surviving)}{N_h(total)} \tag{3.11}$$

where $N_{\gamma(h)}(total)$ is the total number of the simulated γ (hadronic) events which are used; while $N_{\gamma(h)}(surviving)$ is the number of the simulated γ (hadronic) events which remain after the selection procedure. The $N(total)$ can be referred to :

- the total number of simulated events;
- the number of simulated events which trigger the detector;
- the number of simulated events which already satisfy previous selection conditions.

Therefore it is useful to specify the starting condition for the evaluation of the efficiencies. In the following I assume that $N_{\gamma(h)}(total)$ means the number of the events which satisfy the trigger condition (events after the trigger).

- *quality factor* Q

$$Q = \frac{\epsilon_\gamma}{\sqrt{\epsilon_h}} \tag{3.12}$$

where ϵ_γ and ϵ_h are the efficiencies defined above. The Q factor is the enhancement factor of the signal significance after the application of the selection strategy.

I used the following samples of data for comparing the performances of the supercuts and the Tlow cuts:

1. MonteCarlo simulations of the γ rays air showers.

   35574 simulated γ events (γ MC) are used. They are obtained (see [47]) by using the code Corsika ([48],[49]) for the simulation of the air showers. After that the telescope performances are simulated by a dedicated code. The night-sky-background (NSB) light level is also included in the treatment of the response of the detector. The experimental measurements of the NSB light level in the region of the source under study are used in order to simulate the correct response of the detector.

2. Experimental measurements of the hadronic air showers.

   Instead of using MC simulated hadronic events, I used observed hadronic images. 210145 hadronic events are used. A major advantage of the observed hadronic events is the larger statistics compared to the MC

hadronic simulations. MC hadronic simulations are very time consuming, expecially at large zenith angle and for TeV energies (also when clusters of modern computers are used). Therefore MC hadronic simulations are limited to a low statistics. Experimental measurements of hadronic air shower are obtained by pointing the telescope on a sky region,where there are no γ rays sources present. The possible contamination of experimental γ events is negligible (as tested with the distribution of the Alpha parameters of these events). These type of data are named OFF-data. The OFF-data are used as a background data sample. Because they are acquired events, they satisfy the trigger conditions. Therefore the simulated events should also satisfy the trigger conditions (after trigger events) to be compared to the OFF-data. The OFF-data used in the following comparison are taken in a sky regions with NSB comparable to that of the Crab Nebula region.

The two samples are homogenous: both samples are composed by events at zenith angle lower than 45° and are affected by comparable NSB.

In the tables 3.6, 3.7,3.8, 3.9, one can see the γ and the hadron efficiencies obtained with the supercuts and the Tlow cuts. Both efficiencies for a single condition and for the logical AND of all the conditions (named *AND of conditions*) included in a set of cuts are shown. In Fig. 3.8 the plot of the ϵ_γ versus the ϵ_h is also shown. From the listed data it is possible to conclude:

1. the Tlow cuts have a higher hadron rejection power ($\epsilon_h = 0.0028 \pm 0.0001$) than the supercuts ($\epsilon_h = 0.0058 \pm 0.0002$);

2. the Q value of the Tlow cuts is higher (Q = 8.0±0.3) than the one of the supercuts (Q = 7.0±0.3);

Therefore the Tlow cuts are suitable for analysis in which an higher hadron rejection power is required.

lower limit	parameter	upper limit	unit
0.066	Width	0.145	degree
0.165	Length	0.280	degree
0.5	Dist	1.05	degree
60	Size		number of photo-electrons
	Alpha	12.5	degree

Table 3.5: The Tlow cuts

Condition	N_{start}	$\sqrt{N_{start}}$	$N_{surviving}$	$\sqrt{N_{surviving}}$	ϵ
0.07< Width < 0.15	210145	458	30583	175	0.145
0.16<Length<0.3	210145	458	48548	220	0.231
0.51<Dist<1.1	210145	458	139051	373	0.661
Size>60	210145	458	202984	450	0.966
Alpha<15	210145	458	25618	160	0.122
AND of conditions	210145	458	1222	35	0.0058±0.0002

Table 3.6: Efficiencies of the supercuts on the OFF-data at the zenith angle below 45°. For each row one can read the selection condition, the number of starting events (after trigger events) and the statistical error associated; the number of events surviving the selection condition and the statistical error associated, and the efficiency of the selection condition. In the last row the results for the logical AND of all the selection conditions are shown.

Condition	N_{start}	$\sqrt{N_{start}}$	$N_{surviving}$	$\sqrt{N_{surviving}}$	ϵ
0.07< Width < 0.15	35574	189	30060	173	0.845
0.16<Length<0.3	35574	189	30214	174	0.850
0.51<Dist<1.1	35574	189	25199	159	0.708
Size>60	35574	189	33805	184	0.950
Alpha<15	35574	189	31766	178	0.893
AND of conditions	35574	189	19039	137	0.537±0.009

Table 3.7: Efficiencies of the supercuts on the simulated γ events at the zenith angle below 45°. The format of the table is the same as in table 3.6

Condition	N_{start}	$\sqrt{N_{start}}$	$N_{surviving}$	$\sqrt{N_{surviving}}$	ϵ
0.066< Width < 0.145	210145	458	26158	161	0.124
0.165<Length<0.28	210145	458	36370	190	0.173
0.5 <Dist<1.05	210145	458	125883	355	0.600
Size>60	210145	458	202984	450	0.966
Alpha<12.5	210145	458	21357	146	0.102
AND of conditions	210145	458	596	24	0.0028±0.0001

Table 3.8: Efficiencies of the Tlow cut on the OFF-data at the zenith angle below 45°. The format of the table is the same as in table 3.6.

Condition	N_{start}	$\sqrt{N_{start}}$	$N_{surviving}$	$\sqrt{N_{surviving}}$	ϵ
0.066< Width < 0.145	35574	189	29395	171	0.826
0.165<Length<0.28	35574	189	27630	166	0.777
0.5<Dist<1.05	35574	189	22880	151	0.643
Size>60	35574	189	33805	184	0.950
Alpha<12.5	35574	189	30537	175	0.858
AND of conditions	35574	189	14998	122	0.422±0.003

Table 3.9: Efficiencies of the Tlow cuts on the simulated γ events at the zenith angle below 45°.The format of the table is the same as in table 3.6

Cuts	ϵ_h	ϵ_γ	Q value
Supercuts	0.0058±0.0002	0.537±0.009	7.0±0.3
Tlow cuts	0.0028±0.0001	0.422±0.003	8.0±0.3

Table 3.10: The γ and hadron efficiencies, and the Q value for the supercuts and the Tlow cuts.The *Tlow* cuts are selection cuts derived from supercuts, for low zenith angle. The Tlow cuts are tighter than supercuts. They will be used as the base to develop the selection cuts for large zenith angle in the next sections. In this table the Q values for data a the zenith angle lower than 45° are shown.

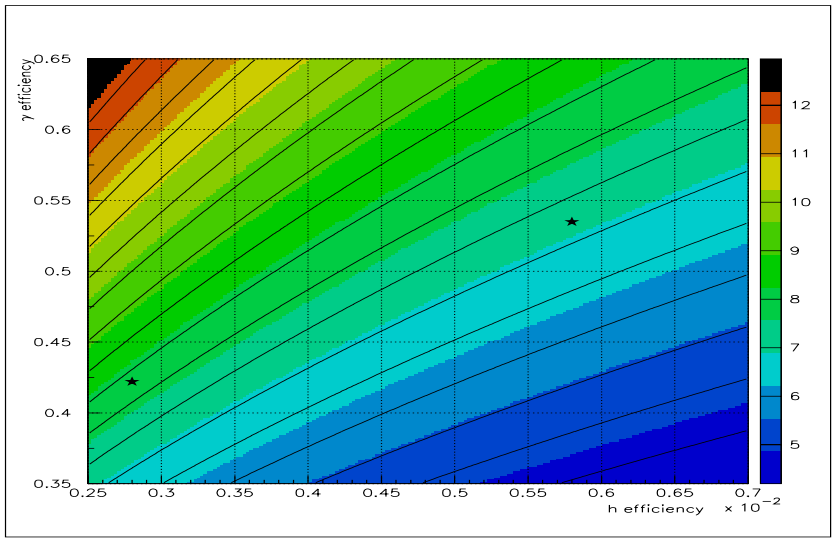

Figure 3.8: The Neyman-Pearson plot for supercuts and Tlow cuts. In this plot the γ efficiency is plotted versus the hadron efficiency. The various colors show combinations of efficiencies for which the Q value is a given one. Iso-Q-value curves are also plotted. The supercuts and the Tlow cuts are represented by the two stars. The star on the right-up, is that one for the supercuts, corresponding to a Q value of ≈ 7. The star on the left-down is that one for the Tlow cuts, corresponding to a Q value of ≈ 8.

Cuts	ϵ_h	ϵ_γ	Q value
Supercuts	0.0369±0.0005	0.177±0.003	0.92±0.04
Tlow cuts	0.0232±0.0004	0.132±0.003	0.87±0.05

Table 3.11: Table of the efficiencies and the Q values for the supercuts and Tlow cuts at zenith angle $> 60°$. One can see that the ϵ_γ is lower than the efficiency of the same cuts at low zenith angle. Whereas the ϵ_h is higher (worst hadron rejection). Both effects are produced by shrinking of the shower images and both effects also cause a bad performance in terms of the Q value.

3.3.3 Observations at large zenith angle

It is possible to verify that selection cuts for small zenith angle are not-effective for the data taken a large zenith angle.

In table 3.11 one can see the performances of the Tlow and the supercuts for the data with zenith angle greater than 60°. The Q value of the selection cuts approaches 1. If Q is equal to 1 then there is no enhancement of the significance of an eventual signal extracted from the data. The reasons of bad performance are:

- the images of the air shower shrink with the increasing zenith angle.
- the distributions of Width and Length parameters move to smaller values
- a bigger fraction of hadronic events has Width and Length comparable with the γ events at low zenith angle
- therefore such events are not rejected

3.3.4 Selection cuts for large zenith angle

We needed to find selection cuts which were effective at large ZA. A simple method to accomplish this task is illustrated in the following scheme:

- to study the transformations of the shower images depending on the zenith angle;
- to describe these transformations as a function of the zenith angle;

- to include the dependence on the zenith angle into the selection cuts. This dependence will be obtained by the study of air showers images, within a large zenith angle range (0 to 75°).

The changes of the images could be either evaluated by the Monte Carlo simulations or by the study of the real hadron events. In the second case one assumes that the images of the γ events transform in the same way of the hadrons images. The assumption is based on the following arguments:

- the effects of zenith angle come mainly from the geometrical factors (the configuration and the distance between the shower and the observer)
- such geometrical factors affect the propagation of Cherenkov light independently on the type of primary particle which has generated the shower.

We opted for studying the zenith angle dependence with real hadrons events. The main advantages of this solution were:

- the transmission and geometrical effects which affect the data are the real ones, while for a simulation they have to be approximated;
- as at the first point, also the response of the detector is the original one;
- it is possible to use a larger statistics, because it is faster to acquire real data than to simulate the MonteCarlo events.

After the study of the real hadron events also the MonteCarlo simulation of the γ events have been studied. The simulation of the γ events at large zenith required a long time and a strong effort.

The sample used for this study was composed of more than 211000 Off-data events and 52403 simulated γ events. In the following I report the study of the transformations of the images in dependence on the zenith angle. At first I define some useful parameters which will be used. Width and Length are the most important parameters which were studied in order to characterize the transformations of the images (and also Size and Dist, which are shown later). Both Width and Length parameters have distributions similar to the function in Fig. 3.9. For this type of distribution it is possible to define:

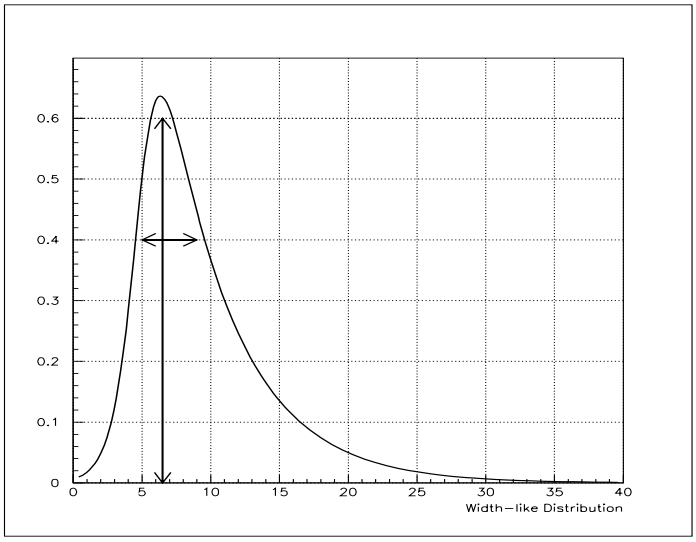

Figure 3.9: A function resembling shape of the distributions of Width and Length parameters. For this type of distribution it is possible to define: 1) the MVL (Most Likely Value), which is the position of the maximum of the distribution and is indicated by a vertical double arrow in the figure; 2) the SAP (spread around the peak), which is spread of the distribution around its maximum, without considering the tail, it is indicated by a horizontal double arrow.

- the *MLV*, which is the most likely value for the events in the distribution. I will refer to it as :

$$MLV_{par}(ZA) \tag{3.13}$$

  where MLV is a function of the zenith angle and par indicates the image parameter under study.

- SAP (spread around the peak) which is the spread of the distribution around the peak, not considering the tail of the distribution. I will

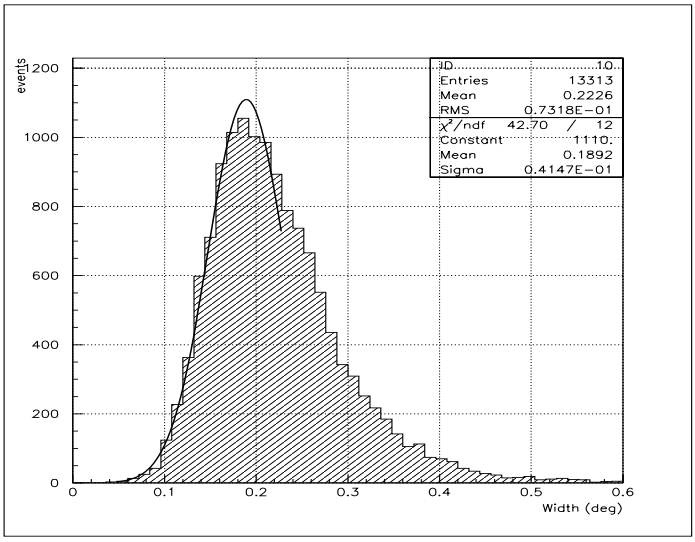

Figure 3.10: An example of the Gaussian fit of the peak of a width-like distribution. The MLV (Most Likely Value) of each sub-sample (zenith angle bin) has been found. The procedure exploits a Gaussian fit, as the one shown it the figure. In order to avoid the influence of the distribution tail, the fit is applied in a limited range. The mean value of the Gaussian fit is assumed to be the MLV_{par} while the σ of the fit is assumed to be the SAP_{par}. A minimum number of the events for each zenith angle bin is required in order to avoid large statistical fluctuations.

refer to it as :

$$SAPpar(ZA) \tag{3.14}$$

where SAP is a function of the zenith angle and par indicates the image parameter under study.

Here I describe how MLV_{Length} and MLV_{Width} had been measured. The data-sample under study had been divided in bins of zenith angle (1-3 degrees or less for larger samples). The extension of the bins had been set in

accordance with the statistics of the data-sample. The MLV of the distribution had been found for each zenith angle bin. The procedure exploits the Gaussian fit, applied into a limited range, in order to avoid the influence of the tail of the distribution (see Fig 3.10). The mean value of the Gaussian fit is assumed to be the MLV_{par} while the σ of the fit is assumed to be the SAP_{par}. The uncertainty of the measurement of the MVL position is assumed to be:

$$\delta MLV_{par} = \frac{SAP_{par}}{\sqrt{N_{events}}} \tag{3.15}$$

A minimum number of the events for each zenith angle bin is required in order to avoid large statistical fluctuations. The results of the measurements are shown in Fig 3.11 and Fig 3.12.

We can now describe the transformations of Width and Length in dependence on the zenith angle. The transformations can be split into two components:

1. a scale factor $K(ZA)$, which accounts for the transformations produced by large changes (in the order of 10°) at the zenith angle.

2. the local dependence on the zenith angle $l(ZA)$, which accounts for the small changes (in the order of 1°) of the zenith angle.

The expressions for K(ZA) and l(ZA) are the following :

$$K(ZA_{1,2}) \;=\; \frac{MVL(ZA_2)}{MVL(ZA_1)} \tag{3.16}$$

therefore

$$MVL(ZA_2) \;=\; K(ZA_{1,2}) \;\times\; MVL(ZA_1) \tag{3.17}$$

and

$$l(ZA) \;=\; \kappa \times ALT \;+\rho \tag{3.18}$$

where $K(ZA_{1,2})$ is the scale factor transforming $MVL(ZA_1)$ to $MVL(ZA_2)$, ALT is the altitude angle, which is equal to 90° - ZA, and is used to simplify the further notation. The l(ZA) is given in linear a approximation. Such approximation holds for a narrow zenith angle range used in the analysis of the data of the SN1006. The combination of the two components gives :

$$K(ZA_{1,2}) \;=\; \frac{\kappa \times ALT_2 \;+\rho}{MVL(ZA_1)} \tag{3.19}$$

where the MVL(ZA_2) is expressed as a local function of the altitude angle, therefore also of the zenith angle. In table 3.15 one can find the values of the parameters which will be used for the selection cuts at a large zenith angle. These values refer to the transformations of the Width and Length parameter, being $ZA_1 = 0\ ^\circ$ and $ZA_2 = 71\ ^\circ$.

The dependences of the Dist and Leakage parameters on the zenith angle were also studied. For distribution of the Dist and Leakage type (see Fig. 3.16) it is possible to define the following indicators:

- the average value of the distribution
- the fraction of the events which are above (or below) a given threshold.

Then the following quantities were measured:

1. the fraction of the events having Dist $< 1.05^\circ$
2. the fraction of the events having Dist $< 0.9^\circ$
3. the fraction of the events having Dist $> 0.1^\circ$
4. the fraction of the events having Dist $> 0.5^\circ$
5. the fraction of the events having Leakage < 0.1
6. the fraction of the events having Leakage $= 0$

The procedure for these measurements was similar the the previous one. The results are shown in table 3.17

The Size parameter is the total amount photo-electrons in the image. The Size parameter, for the same shower observed under two different zenith angles, changes. The scaling of the Size parameter is approximated by the following expression:

$$Size(ZA_2) \ = \ Size(ZA_1) \ \times \ \frac{d_1^2}{d_2^2} \ \times \frac{f(abs_1)}{f(abs_2)} \qquad (3.20)$$

where d is the distance between detector and shower core, f(abs) is the atmospheric absorption, the indices 1 and 2 indicate respectively the observations at zenith angle ZA_1 and ZA_2. The final effect of the Size rescaling is an energy threshold shift, which will be studied by means of the Montecarlo simualtions, for the telescope energy calibration.

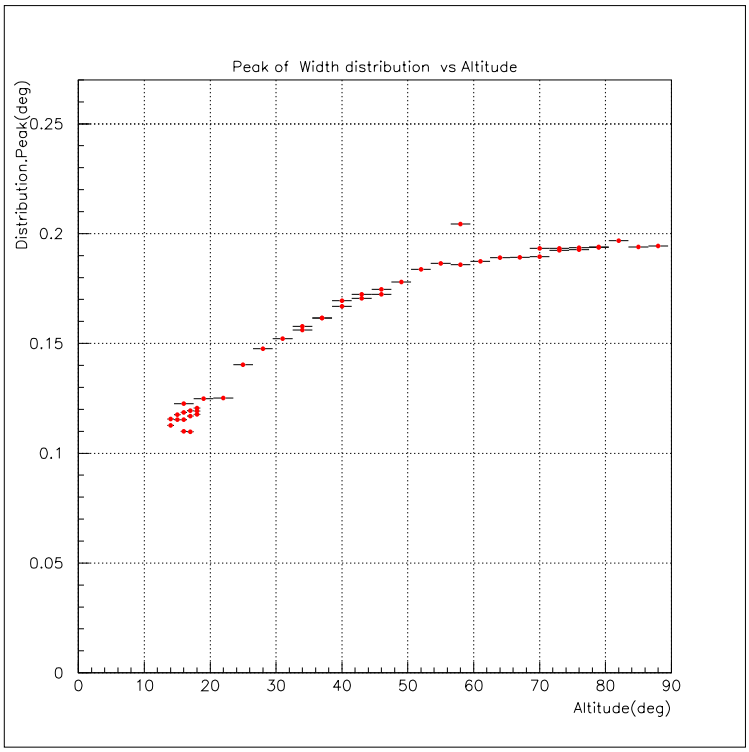

Figure 3.11: MVL (Most Likely Value) of the Width image parameter versus the altitude angle (90° - ZA) for experimental data (hadrons). It is possible to see how the most likely width of the events decreases from a small zenith angle (large altitude angle) to a large zenith angle (small altitude angle). The change is modest below 30° of the zenith angle (60° of altitude angle) while it is more important for larger zenith angles. In the figure the measurements for many different data samples at different experimental conditions are shown.

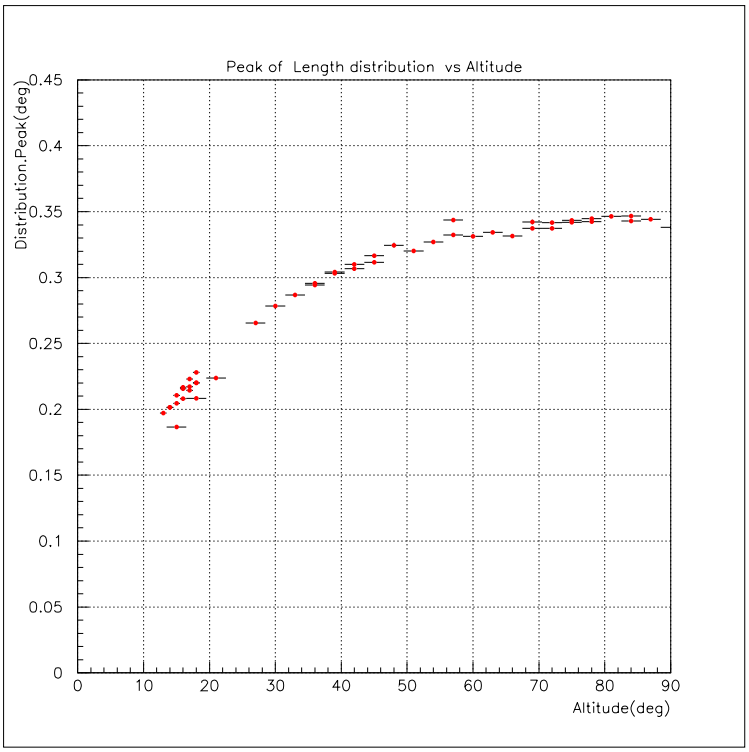

Figure 3.12: The MVL (Most Likely Value) of the Length image parameter versus the altitude angle (90° - ZA) for experimental data (hadrons). One can see how the most likely length of the events (maximum semi-axis of the image of the shower) decreases from a small zenith angle (large altitude angle) to a large zenith angle (small altitude angle). The effect is modest below 30° of the zenith angle (60° of altitude angle) while it is more important for larger zenith angles. In the figure the measurements for many different data samples at different experimental conditions are shown.

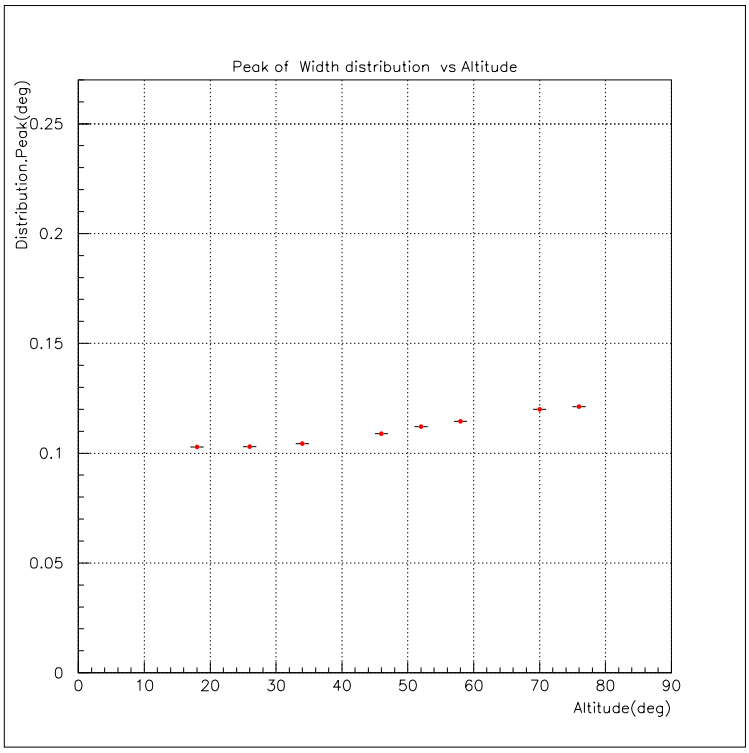

Figure 3.13: The MVL (Most Likely Value) of the Width image parameter versus the altitude angle (90° - ZA) for MonteCarlo simulation of γ events. For the Monte Carlo simulations of the γ events the Width decreases from 0° to $\approx$ 65° of the zenith angle (15° of altitude angle). The value shows a small dependence on the zenith angle. The most likely explanation is that the pixel size plays an important role. The MLV value for the last 2 bins of the zenith angle (first 2 bins of altitude angle) is just above 0.1°, while the diameter of the photo-multiplier in the camera of the CT1 is 0.244°. One can compare this figure with the related one for experimental hadronic events (see Fig 3.11).

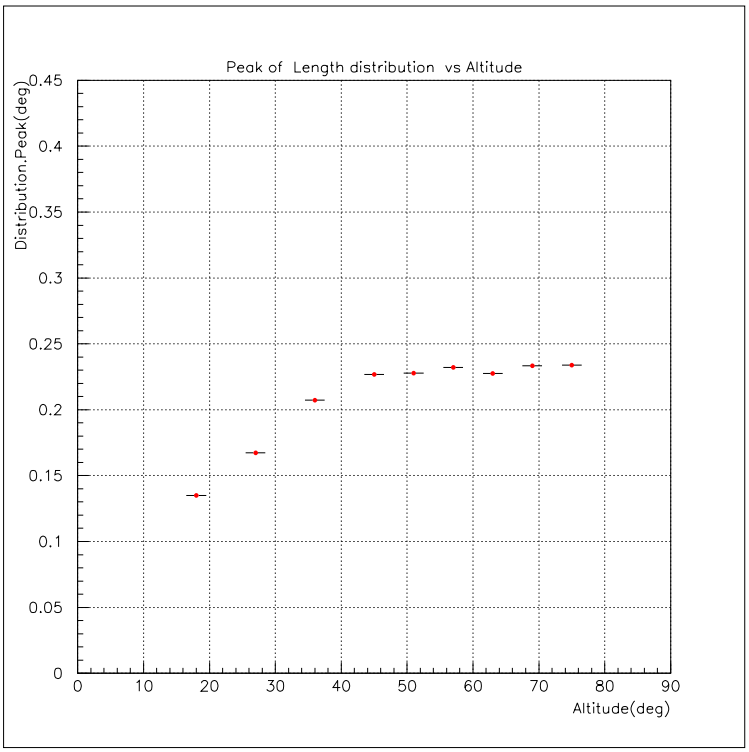

Figure 3.14: The MVL (Most Likely Value) of the Length image parameter versus the altitude angle (90° - ZA) for MonteCarlo simulation of γ events. One can compare this figure with the related one for experimental hadronic events (see Fig 3.12). For the Length of γ induced events the saturation effect due to the CT1 pixel size is not yet evident.

Parameter	MVL(0°) [°]	κ [°]	ρ [°]
Width	0.20	0.0017	0.090
Length	0.36	0.0053	0.130

Figure 3.15: The values of the parameters κ and ρ, which are used in the formula for the scaling factor K(ZA).

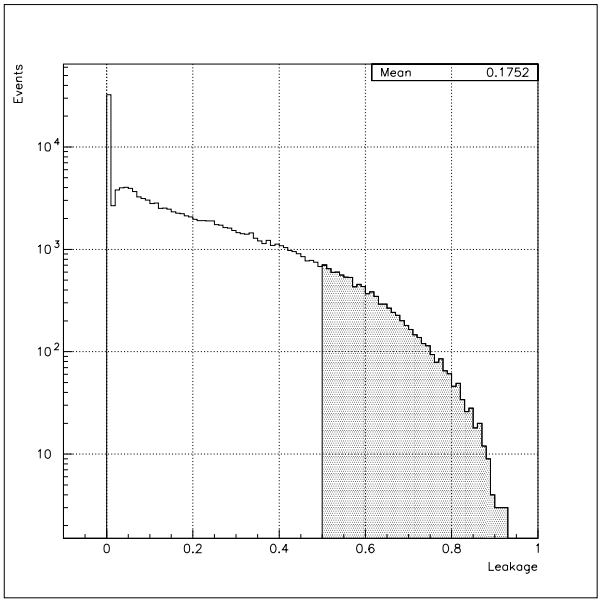

Figure 3.16: The distribution of the estimated Leakage parameter for experimental events. The shadowed part of the histogram covers the fraction of events which have Leakage larger than 0.5 (for example).

Z.A. range(°)	total events	Leakage<0.1	fraction	Leakage=0	fraction
0 - 10	64773	22389	0.3456	7499	0.116
10 - 20	58952	20973	0.3558	7532	0.128
20 - 30	19476	7211	0.370	2518	0.129
30 - 40	25487	10073	0.3952	3949	0.155
40 - 50	180425	78704	0.4362	34903	0.1934
50 - 60	33654	16456	0.489	8553	0.254
60 - 70	99709	65501	0.6569	50388	0.5053
70 - 80	58901	39686	0.6737	30306	0.5145
Z.A. range(°)	total events	Dist<1.05	fraction	Dist<0.9	fraction
0 - 10	64773	64773	1.000	36531	0.564
10 - 20	58952	58952	1.000	32815	0.556
20 - 30	19476	19475	0.999	10577	0.543
30 - 40	25487	25221	0.990	13495	0.530
40 - 50	180425	177958	0.986	93066	0.516
50 - 60	33654	33647	0.999	17196	0.511
60 - 70	99709	99708	1.000	56246	0.564
70 - 80	58901	58901	1.000	33271	0.565
Z.A. range(°)	total events	Dist>0.1	fraction	Dist<0.5	fraction
0 - 10	64773	64389	0.994	54748	0.845
10 - 20	58952	58605	0.994	49861	0.845
20 - 30	19476	19382	0.995	16578	0.851
30 - 40	25487	25338	0.994	21660	0.850
40 - 50	180425	179432	0.994	153582	0.851
50 - 60	33654	33448	0.994	28463	0.846
60 - 70	99709	99114	0.994	82069	0.823
70 - 80	58901	58572	0.994	48725	0.827

Figure 3.17: The study of some statistical indices of the distributions of Dist and Leakage parameters versus the changes in the zenith angle.

3.3.5 The muon background

In the following subsection I illustrate:

- why the muons (μ particles) are an additional background for observations at a large zenith angle;
- how it is possible to reject such background.

Cosmic rays generate a large number of secondary muons. As an example one of the most important interaction producing muons is :

$$N_{CR}\ N_{Atm}\ \rightarrow\ hadrons\ \rightarrow\ ...\pi^{\pm}\ \rightarrow\ ...\mu^{\pm}, e^{\pm}, \nu_{e,\mu}(\bar{\nu}_{e,\mu}) \tag{3.21}$$

where N_{CR} is a cosmic nucleus which acts as a projectile, N_{Atm} is a nucleus of the atmospheric gas, which acts as a target. The charged πs frequently decay in μs, electrons and neutrinos. The muons are highly penetrative, they can cross a thick layer of matter before they are stopped, therefore they have a high probability to reach the ground. These muons can pass across the camera and the PMs. In Fig 3.18 one can see a scheme of the interaction of the atmospheric muons with the PMs of the camera. Cherenkov light is produced when a muon passes across the glass envelope of the PMs. The light is guided often from the site of the production up to the photo-cathode, because the same glass envelope acts as modest quality a light guide. When the light arrives to the photo-cathode it can produce photo-electrons and generate a signal. A single muon can produce a sufficient high signal exceeding the trigger threshold in many PMs, then it can trigger the telescope. When the telescope points to large a zenith angle, the camera exposes the side to the maximum flux of the atmospheric muons. Therefore the atmospheric muons are an non-negligible background for observations with the IACTs at a large zenith angle. The PMs triggered by a single muon are aligned, therefore a muon produces a track-like image.

Muons can also produce Cherenkov light, which is in principle detectable by the telescope. The CT1 sensitivity is too low in order to detect such a Cherenkov emission from a single muon.

The interaction of atmospheric muons with the telescope has been studied with a direct measurement. The muon events were observed by means of the CT1. The telescope was operated at a large zenith angle with the lid of the camera closed (so-called muon-runs). With this operational mode there is no input of light from the external sources. The telescope is triggered only by the muons. The trigger rate is very low. The same measurement

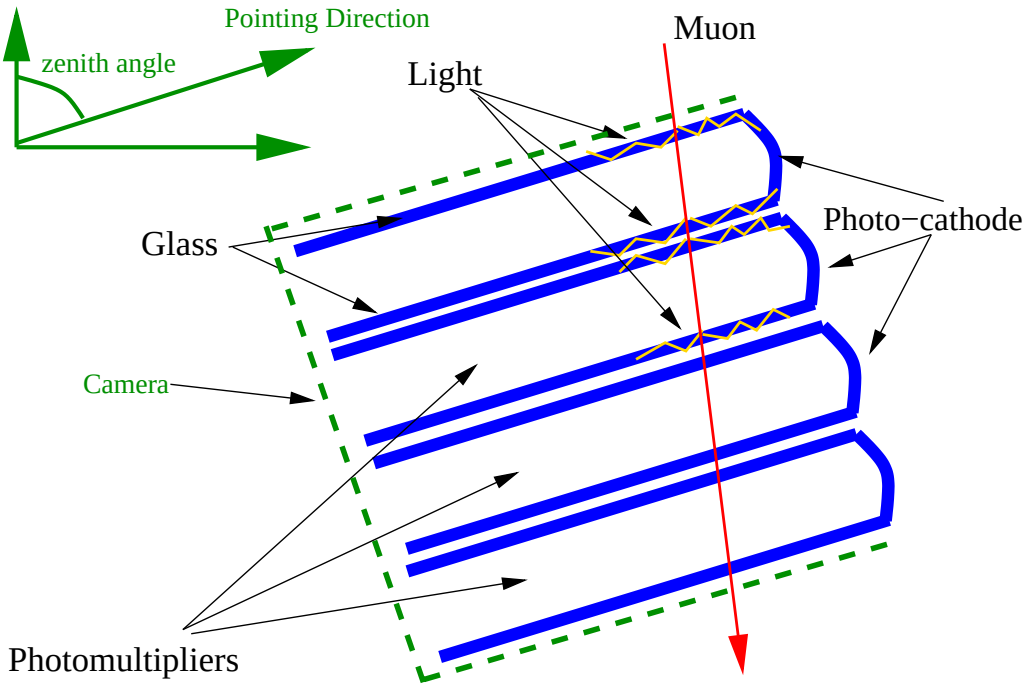

Figure 3.18: Scheme of the direct interaction of an atmospheric muon and the camera of a Cherenkov telescope. Cherenkov light (yellow lines) is produced when an atmospheric muon (the red arrow) passes across the glass envelope of the PMs. The same glass envelope acts as a light guide. Then the light can be guided up to the photo-cathode. If enough light arrives to the photo-cathode it produces photo-electrons and generates a signal. A single muon can produce a signal exceeding the trigger threshold in many PMs, then it can trigger the telescope. As seen in the figure the path of the muon is a straight line. Therefore the PMs triggered by muons will give a track-like image. In the figure the green reference frame shows the pointing direction of the camera (telescope).

also provides an estimate for the frequency of such events. The frequency of muon-induced events is 5.1×10^{-3} Hz

The muon background is present in the data taken for the study of the SN1006. Therefore I developed a method for the rejection of the muon

events. The method is based on the observation of the properties of the images (tracks) produced by muons. The properties of the muon events which will be used are the following:

- the topology of the event. In particular the number of core and boundary pixels which compose the image has been used.
- the light density of the event. The ratio of the event Length to the logarithm of the photo-electrons number in the image (Size) has been used.

In Fig 3.19 and 3.20 one can see the distributions of the core and boundary-pixels (pixels with a content of signal between 2.5 and 3 σ(NSB) and on the boundary of the image) in the sample of the experimental muon events. In the majority of the muon events there are no pixels classified as boundary. One can compare the distribution of the boundary pixels of the experimental muon events and the MonteCarlo simulations of the γ events in Fig 3.21 and 3.22. It is possible to conclude that a large fraction of the muon events can be rejected by requiring at least one boundary-pixel in an image. These cuts result in a gamma loss (1-ϵ_γ) in the order of 0.5. This loss affects only a subset of the data (the events without boundary-pixels), to which the muon cuts are applied. The efficiency of the muons cut is discussed in detail in subsection 3.3.6.

The light density of the muon events is the other quantity considered for the muons rejection. In Fig 3.23 one can see the plot of the quantity log(Size) versus the Length parameter. It is possible to see that the experimental muons cluster in a region of the plane in Fig 3.23. Instead the region occupied by the γ events (Monte Carlo simulations) is more extended. It is also possible to separate the region with the majority of the muons from the rest of the plane with a simple condition.

In conclusion, both conditions on topology and light density of the events can be used to reject the muon events. That has been done to obtain the cuts used in this thesis.

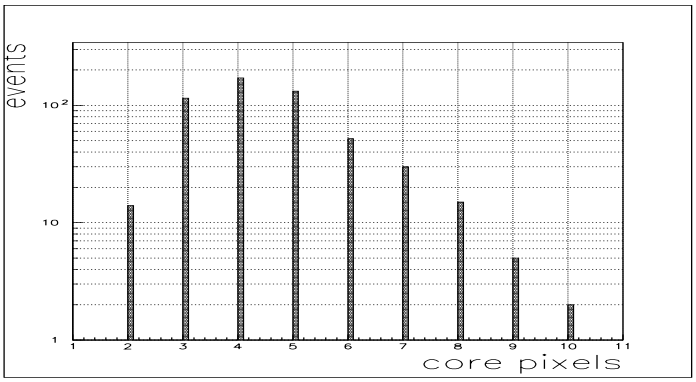

Figure 3.19: The distribution of core-pixels number for experimental muons. The experimental muons events have been acquired with the so-called muon-runs

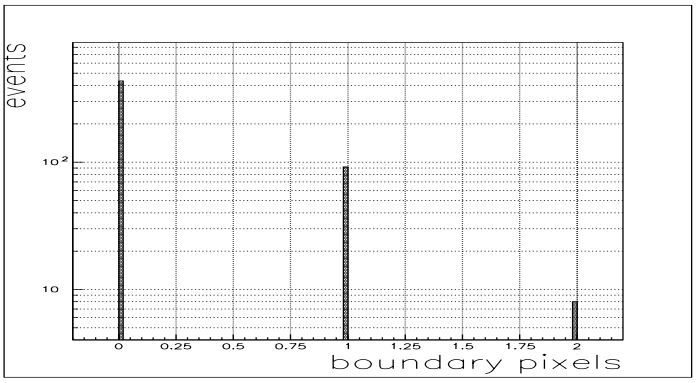

Figure 3.20: The distribution of the boundary-pixels number (experimental muons). The boundary-pixels have signals from 2.5 to 3 σ above the pedestals, and a neighbour core-pixel.

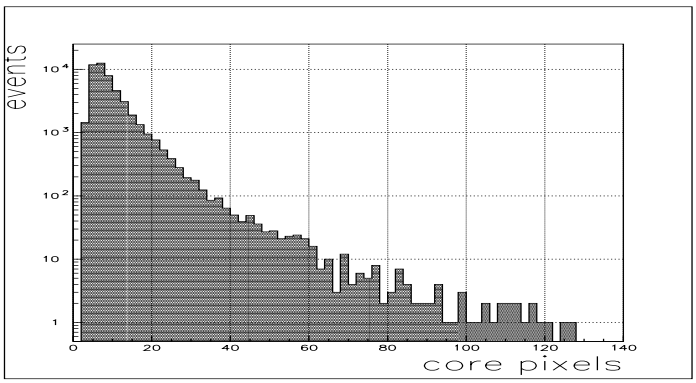

Figure 3.21: The distribution of the number of the core-pixels for the MonteCarlo γ events. The core-pixels have signals above 3 σ from the pedestals fluctuations, and have at least a neighbour above the same threshold.

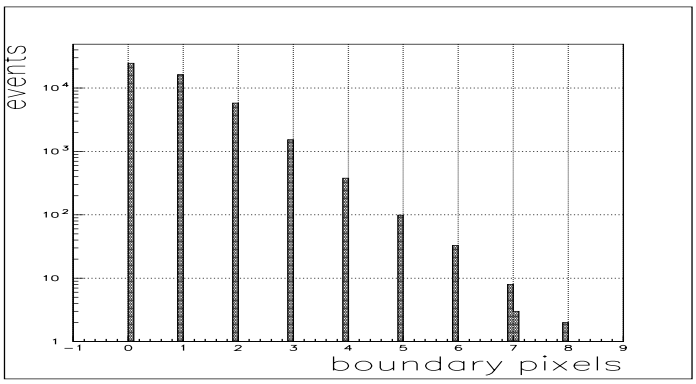

Figure 3.22: The distribution of the number of boundary-pixels for the MonteCarlo γ events. The boundary-pixels have signals within 2.5 and 3 σ above the pedestals fluctuations, and have at least a neighbour core-pixel.

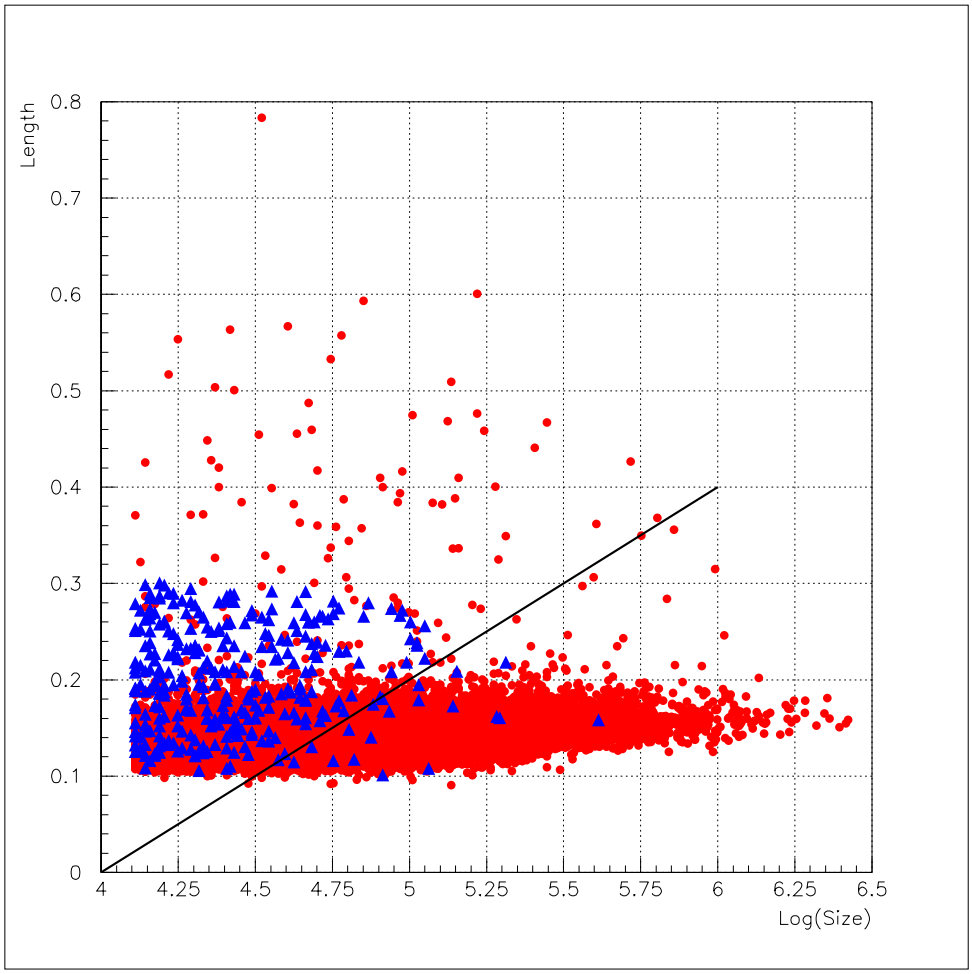

Figure 3.23: The scatter plot of the logarithm of Size parameter versus the Length parameter. In this plot the red dots are the MonteCarlo γ events at a large zenith angle, the blue triangles are from the experimental muon events. One of the possible conditions to separate the γ events and the muon events is shown with the black straight line.

Parameter	condition	identifier
Size	> 60 ph.el	DQ1
Dist	$< 1.05^{\circ}$	DQ2
Leakage	$= 0$	DQ3

Table 3.12: The data-quality global cuts. These selection cuts are applied on the Size, Dist and Leakage parameters. The Size and Dist cuts are used as standard for the analysis of the CT1 data. The Leakage cut requires the events to be fully contained in the camera of the telescope.

3.3.6 Selection cuts for the analysis

In this subsection I report the selection cuts used for the SN1006 data analysis. The results of the previous subsections have been used to derive these cuts. The selection cuts are composed of the following parts:

- data-quality global cuts;
- cuts for the rejection of the backgrounds;
- cuts dependent on the camera position.

The data-quality global cuts are applied to the data after the filtering process. They are cuts on the Size, Dist and Leakage parameters. These cuts reject data of low quality. The Size and Dist cuts are used as a standard for the analysis of the CT1 data. The Leakage cut has been introduced in accordance to the study shown in the subsection 3.3.4. In particular it has been required that the events should be fully contained in the camera of the telescope. The data-quality global cuts are listed in Tab 3.12. It is relevant in this context that the data-filtering requires at least two core-pixels, together with the other conditions. The two core-pixels threshold is an implicit data-quality selection.

The cuts for the rejection of the backgrounds are applied to the data after the global quality cuts. These cuts are divided into two branches:

1. the first branch: events with $\geq$ one boundary-pixel, strong hadron and muons suppression;
2. the second branch: events without boundary-pixels, looser muons suppression.

	Bound.Pix ≥ 1		
lower limit	parameter (units)	upper limit	identifier
0.066 $\times$ K($ZA_{0,71}$)	Width(°)	0.145$\times$ K($ZA_{0,71}$)	1B1
0.165 $\times$ K($ZA_{0,71}$)	Length(°)	0.280$\times$ K($ZA_{0,71}$)	1B2
0.3 $\times$ Length	Width(°)	0.63 $\times$ Length	1B3

Table 3.13: The first branch of the cuts for the rejection of the backgrounds. It is applied to the events with at least one boundary-pixel. They consist of the Tlow cuts multiplied by the scale factor K(ZA) (for an explicit calculation of the cuts values, at zenith angle=71° see Tab. 3.14). An additional condition on the ratio between Width and Length parameters is also applied. The last condition reject all the images which are too rounded. (The direction of the major axis of circular images is affected by a relatively large uncertainty)

The first branch of the cuts is applied to the events with at least one boundary pixel. These events have a low probability to be muons, as seen in subsection 3.3.5. In the first branch the selection cuts are the Tlow cuts multiplied by the scale factor K(ZA) (3.3.4). At a large zenith angle the images are more rounded than those at a low zenith angle, because of the effects previously discussed . The rounded images are affected by a large uncertainty in the direction of the major axis. Therefore an additional condition on the ratio between Width and Length is also applied. This condition rejects all the images which are too rounded. In table 3.13 the selection cuts of the first branch are listed.

The second branch is applied to the events without boundary-pixels. This branch consists of :

- a muon rejection based on the light density of the image
- a cut in Width

The selection cuts for the second branch are listed in Tab. 3.15. The events which satisfy the first *OR* the second branch are both accepted.

The third group (cuts dependent on the camera position) consists of just one cut. The cut is applied over the NDist (New Distance) parameter. As one can see in Fig 3.24 the NDist is the angular distance between the center of gravity of the image and a reference system over the camera plane, independently from where the system is centered. If the reference system

	Bound.Pix ≥ 1		
lower limit	parameter (units)	upper limit	identifier
0.0403	Width(°)	0.0887	1B1
0.106	Length(°)	0.179	1B2

Table 3.14: The explicit calculation of the first branch cuts for the Width and Length parameters, for a zenith angle = 71°. These values provide the order of magnitude of the cuts applied for the present analysis. It should be remarked that the cuts on Width and Length parameters are not constant, but *a function of the zenith angle.*

	Bound.Pix = 0		
lower limit	parameter	upper limit	identifier
	Length	0.2 × log(Size) - 0.8	2B1
	Width	0.09	2B2

Table 3.15: The second branch of the cuts for the rejection of the backgrounds. It is applied to the events without the boundary-pixels. They consist of a muon rejection condition based on the light density (ratio between Length and the logarithm of Size parameter) of the image and a selection condition based on the Width parameter.

is centered in the center of the camera then NDist coincides with the Dist parameter (as defined by Hillas). The cut over NDist is applied together with the False Source Method (FMS, see subsection 3.4.2) for the investigation of the extended sources or the off-axis ones. The cut selects a fraction of the data sample, which changes in dependence of the sky position (position over the camera plane) under study. Therefore the sub-samples used for the study of two different sky positions are not in general coincident.

The efficiencies for the γ, the hadrons and the muons have been studied in order to characterize the selection procedure. The results of the study of the efficiencies are reported in the following tables:

- Table 3.16. Efficiency of the cuts on the MC γs sample (ϵ_γ). The selection cuts have been applied one by one and then all together to a sample of the MC simulations of γ events. For the study of the large zenith angle range 10740 events at 72° of zenith angle and 2561 events at 65° have been used. The MC simulations have been treated with

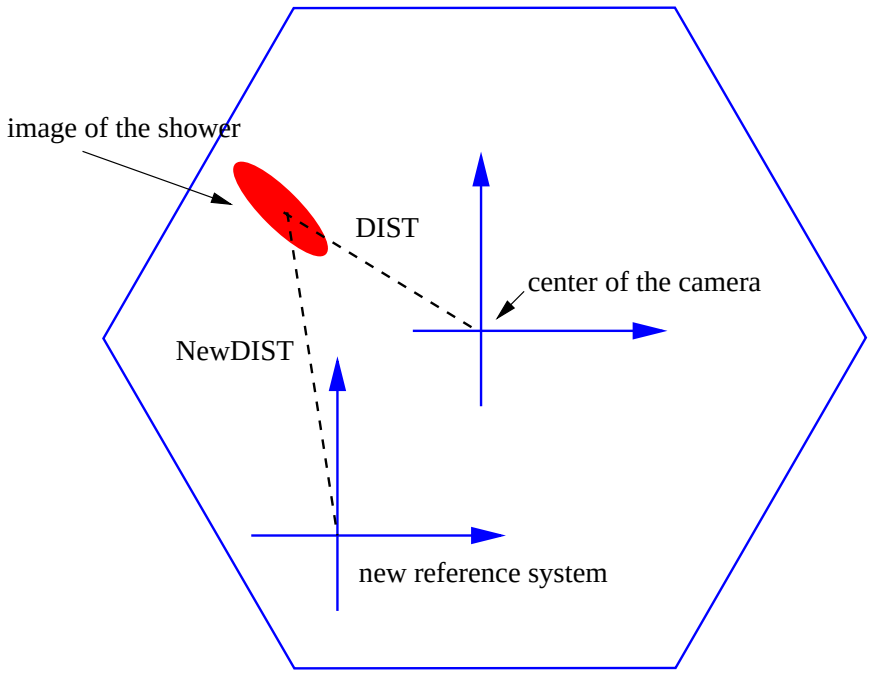

Figure 3.24: An illustration of the NDist (NewDist) parameter. The NDist parameter is the angular distance between the center of gravity of the image and a reference system placed over the field of view of the camera. As seen in the figure, NDist is analogous of the Dist parameter, but it is calculated in a generic reference system. If the reference system is the usual one (centered in the center of the camera) then NDist and Dist coincide.

the same NSB of the SN1006 sky location.

- Table 3.17. Efficiency of the cuts on the experimental hadrons sample (ϵ_{hadron}). A sample of 102261 hadronic events, observed with the CT1 at a large zenith angle (mainly distributed around 70°) has been used. The large zenith angle OFF data (experimental hadrons) have been taken on sky region with NSB similar to that of the SN1006.

- Table 3.18. Efficiency of the cuts on the experimental muons sample (ϵ_{μ}). 514 experimental muon events have been used to study the muon efficiency of the cuts. These events have been recorded by means of the CT1 and required more than 28 hours of observations. This sample is mainly distributed around 70° of zenith angle.

The Width parameter of the simulated γ events goes in a regime of saturation for the zenith angles larger than 65°, as seen in Fig 3.13 (MLV_{Width} saturation). The saturation is produced when the MLV_{Width} has an angular amplitude smaller than the pixel-grain of the camera (the radius of the pixel is 0.144°). The MLV_{Width} saturation affects strongly the gamma efficiency (ϵ_γ) for the selection cuts.

The effect of the MLV_{Width} saturation on the ϵ_γ can be measured. The method is the following:

1. the distribution of the Width parameter is rescaled (here the rescaling factor is 0.9, in order to reduce the saturation level of the 10%), i.e.

$$MLV_{Width}^{SCALED} = MLV_{Width}^{ORIGINAL} \times 0.9 \qquad (3.22)$$

2. the cuts are applied again and the new ϵ_γ has been obtained.

With this method it is possible to measure the gamma efficiency when the MLV_{Width} saturation would have occurred at a different (lower) value. At the same time the method gives an estimate of the systematic error of the gamma efficiency, in the case that the MonteCarlo simulations are predicting a wrong value for the MLV_{Width} saturation. The procedure gives as result a new set of γ efficiencies. They are listed in the table 3.19, in which is shown the efficiency of the cuts on the MC γs sample, after scaling of the Width parameter distribution with a factor 0.9. The same data sample as for table 3.16. has been used.

After the study of the efficiencies it is possible to list some conclusions:

1. A suitable selection procedure for the data analysis of the large zenith angle observations has been developed.

2. The procedure provides enough rejection power against the dominant backgrounds of hadrons and muons.

3. It also provides an acceptable γ efficiency in order to retain the eventual γ events, which are contained in the experimental sample.

4. The procedure is articulated in few branches which allow to increase the efficiency for γ events.

5. The pixel size affects already seriously the gamma efficiency ϵ_γ because of the saturation effect.

Cut section	Cut	parameter	starting γs	selected γs	ϵ_γ
Data-quality	DQ1	Dist	13210	11774	0.891±0.009
Data-quality	DQ2	Size	13210	12903	0.976±0.009
Data-quality	DQ3	Leakage	13210	12217	0.924±0.009
First branch	1B1	Width	5212	1076	0.206±0.006
First branch	1B2	Length	5212	4487	0.86±0.01
First branch	1B3	Width	5212	1836	0.352±0.008
First branch	1B1 & 2 & 3		5212	795	0.152±0.005
Second branch	2B1	Length	7997	3818	0.477±0.007
Second branch	2B2	Width	7997	2568	0.321±0.006
Second branch	2B1 & 2B2		7997	677	0.085±0.003
position dep.		NDist	13210	12336	0.933±0.008
signal region		Alpha	13210		
All sections			13210	667	0.051± 0.002

Table 3.16: Table of the cuts efficiency of on a sample of the MC γs. In the table the first column is the part of the cuts in which a single condition is applied; the second column is an identifier of the single condition; the third column gives the parameter on which the cut is applied; in the fourth column the number of events in the starting sample is written; the fifth column shows the number of surviving events; in the last column one can find the efficiency of the single cut. I fixed the center of the camera as a study-position for the NDist cut, therefore the efficiency for the cut on NDist is the possible maximum. The last row provides the information for the application of the whole selection strategy. (For the numerical values of the cuts see Tab 3.13,3.14,3.15)

An important comment is: The used cuts are clearly not the best ones, but are simple to apply. As long as one applies the same set of cuts to the data and MC events for the calculation of the energy threshold, fluxes and spectra, no *wrong* results will be obtained [1], except the errors will be larger.

[1] i.e. no artificial excess signal will be generated, however an existing small signal may be missed, as the errors will be increased

Cut section	Cut	parameter	starting hs	selected hs	ϵ_h
Data-quality	DQ1	Dist	102261	65446	0.640±0.003
Data-quality	DQ2	Size	102261	75940	0.743±0.003
Data-quality	DQ3	Leakage	102261	55402	0.540±0.003
First branch	1B1	Width	58233	14853	0.253±0.003
First branch	1B2	Length	58233	20647	0.354±0.002
First branch	1B3	Width	58233	35418	0.608±0.003
First branch	1B1 &2 &3		58233	9742	0.167±0.002
Second branch	2B1	Length	42120	6296	0.1494±0.002
Second branch	2B2	Width	42120	17394	0.4129±0.003
Second branch	2B1 & 2B2		42120	388	0.0092±0.0005
position dep.		NDist	102261	58070	0.567±0.002
signal region		Alpha	102261		
All sections			102261	58	0.00056±0.00007

Table 3.17: Table of the efficiency of the cuts on the experimental hadrons sample. The format of the table is the same as in table 3.16 (For the numerical values of the cuts see Tab 3.13,3.14,3.15)

Cut section	Cut	parameter	starting μs	selected μs	ϵ_μ
First branch	1B1	Width	96	49	0.5±0.1
First branch	1B2	Length	96	47	0.5±0.1
First branch	1B3	Width	96	49	0.5±0.1
First branch	1B1 & 2 & 3		96	17	0.18±0.05
Second branch	2B1	Length	418	14	0.033±0.009
Second branch	2B2	Width	418	332	0.79±0.09
Second branch	2B1 & 2B2		418	8	0.019±0.07
position dep.		NDist	514	514	1.0±0.1
signal region		Alpha	514	73	0.14±0.02
All sections			514	1	0.002±0.002

Table 3.18: Table of the efficiency of the cuts on the experimental muons sample. The format of the table is the same as in table 3.16 and in table 3.17 (For the numerical values of the cuts see Tab 3.13,3.14,3.15).

Cut section	Cut	parameter	starting γs	selected γs	ϵ_γ
First branch	1B1	Width	5796	1907	0.329±0.008
First branch	1B3	Width	5796	3030	0.52±0.01
Second branch	2B2	Width	7531	4123	0.547±0.009
All sections			13301	1210	0.091± 0.003

Table 3.19: Table of the efficiency of the cuts on the MC γs, with an artificially reduced (10%) saturation level. Only the relevant efficiencies are reported. The format is the same as for the three previous tables. table 3.16, 3.17 and 3.18.

Data	ϵ_γ	ϵ_h	Q value
original	0.051±0.002	0.00056±0.00007	2.2±0.3
width saturation test	0.091±0.003	0.00056±0.00007	4.0±0.5

Table 3.20: Table of Q values for the selection procedure. The Q values for the selection procedure are listed. In the first row the value obtained with the MC γs and experimental hadrons is reported. This is the Q value of reference for the performances of the selection procedure used in this thesis. In the second row the Q obtained with MC γ with an artificially reduced (10%) saturation level (see also Tab. 3.19) is reported. This table demonstrates the importance of the MLV_{Width} saturation. The Q value for an artificially reduced (10%) saturation level is not used for the analysis.

3.4 Search for off-axis sources

The traditional mode of operation for an imaging atmospheric Cherenkov telescope requires :

- to point towards the source under study, i.e. to have the source at the center of the field of view, where the sensitivity of the detector is at the maximum;
- to study the excess of the γ candidates coming from the center of the field of view.

It is not always possible to observe under above listed conditions . As an example it is not possible to have the source at the center of the field of view of the telescope when the position on the sky map is badly known or the source is extended. In other cases it is interesting to study an eventual excess of γ events coming from any point within the field of view of the telescope.

The position of the γ rays emission area, compared to the angular resolution of the detector, are important for the IACTs data analysis (expecially for this work).

Gamma rays travel in a straight line through the galaxy because they are unaffected by the galactic magnetic field. The arrival direction of the γ rays ($\bar{p}_{cosmic}$) coincides with the sky position where one sees the emitting source. An IACT measures the direction of the axis of the air shower ($\bar{p}_{shower}$) produced by the γ ray (see Fig. 3.25). The air shower has the axis lined up with the direction of the parent cosmic particle. Few exceptions come from a very irregular development of the shower (depending on the first interaction of the cosmic particle), or geo-magnetic effects for the shower of low energy cosmic rays. The shower axis orientation $\bar{p}_{shower}$ is measured with the resolution $\delta\Theta_{shower}$, which depends on the optical angular resolution but in general is not identical with it. The angle $\delta\Theta_{shower}$ defines the angular resolution with which one can resolve the arrival orientation of the γ rays. Therefore we expect to observe an excess of the γ-like events coinciding with the sky position of the point-like γ rays source, with a spread given by $\delta\Theta_{shower}$ (without considering other effects like inaccuracy in the pointing of the telescope, etc,..). We can distinguish between four main types of sources (see also Fig. 3.26):

- Point-like source: the telescope angular resolution for γ rays ($\delta\Theta$) is larger than the angular extension of the source (the emitting region of the astrophysical object). In this case the spread of the arrival

orientations is dominated by the detector uncertainties and it is not possible to resolve structures of the source.

  - Point-like on-axis source: when a point-like source stays at the center of the field of view of the telescope. Usually this position offers the maximum of the sensitivity.
  - Point-like off-axis source: when a point-like source is not at the center of the field of view of the telescope. In this case an analysis for the on-axis sources may underestimate the γ rays flux from the source or miss it at all.

- Extended source: when the emitting region has angular size larger than $\delta\Theta$. In this case it is possible to resolve structures of the source. A moderately extended source can still be observed on-axis.

3.4.1 Effects of the displacement of the source

The position of the γ rays source in the field of view of the telescope produces important effects on the distributions of some image parameters. These effects have to be considered when one searches for off-axis or extended sources. The same effects also make ineffective an on-axis sources analysis, when applied to off-axis sources. The most important of effects are:

1. Effects on the Alpha parameter.

   The Alpha parameter measures the angular distance between the major axis of the shower image and the supposed incoming direction of the γ rays. Events coming from the putative source have small Alpha (Alpha $\approx$ 0). If one measures the Alpha parameter for a putative position while the real source is in another position then the effect arises (see Fig. 3.27). The γ rays events will have Alpha, which is spread from 0 to large values ,and which clusters around a value different from zero. Therefore the majority of the γ events will stay in a region outside of the *signal region* (= small Alpha, for example Alpha $< 12.5\ ^\circ$). In Fig. 3.29 it is shown the distribution of the Alpha parameter for a strong source observed deliberately off-axis (the source is the Mkn501 during a strong flare, this sample of experimental data is described in 3.4.3, where it is extensively used.). The excess of γ events is spread at low Alpha values (0 to 35-40°). In Fig 3.29 the blue line is an estimate of the background. The events in excess are those above the blue line. The excess has a significance larger than 10 σs. Nevertheless

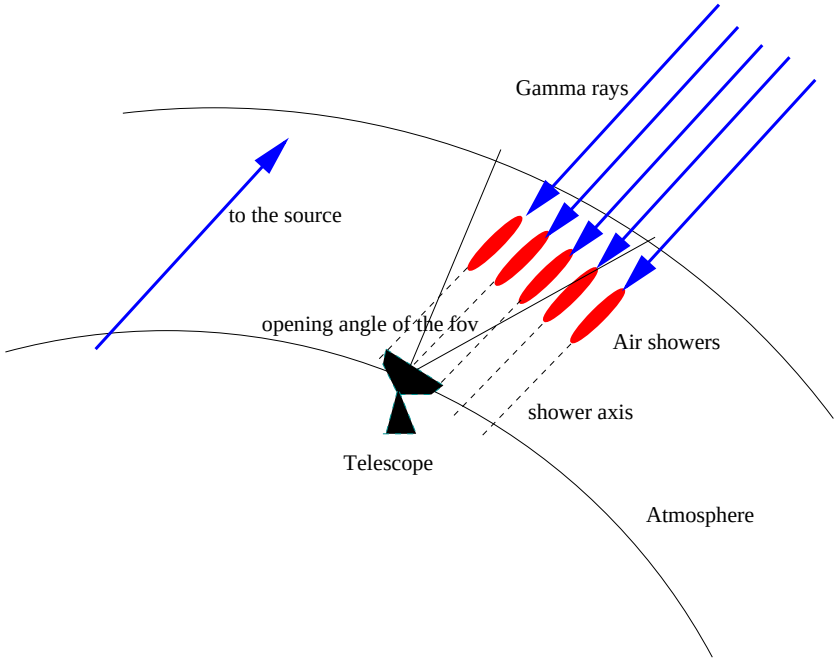

Figure 3.25: An illustration of the γ ray orientation and the shower axis. Gamma rays come from an astrophysical source. They have trajectories almost parallel because of the distance of the source (their spread is due to the angular extension of the source). An IACT measures the Cherenkov light coming from the air showers. Therefore this instrument does not measure directly the incoming direction of the γ rays. It, instead, measures the orientation of the axis of an air shower. This axis is coincident with the orientation of the momentum of the cosmic particle which initiated the shower. The angular resolution for the incoming direction of the γ rays is $\delta\Theta_{shower}$, which is the angular resolution for the measurement of the shower axis orientation

the majority of the signal is significantly outside the region (Alpha $<$ 12.5°), which is usually considered for the on-axis analysis. With the standard analysis, the excess is fitted with a Gaussian, which is centered in Alpha = 0. Then the majority of the excess will be ignored by the standard analysis for the point-like sources on-axis.

2. Effects on the distribution of the NDist parameter.

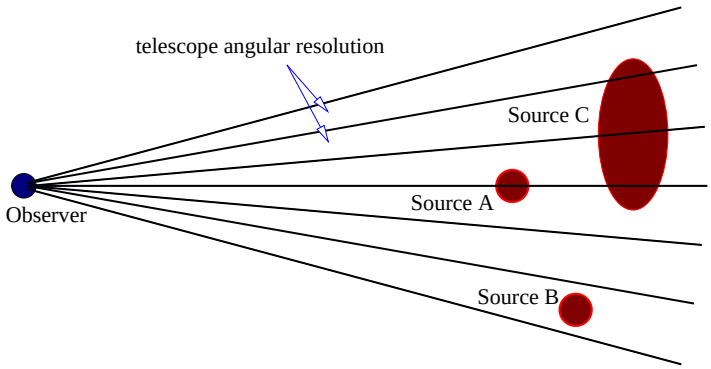

Figure 3.26: Here 3 different sources (A,B and C) are illustrated. The telescope field of view (FOV), projected up to the sources, is also shown. The FOV is subdivided in smaller angles, which represent the telescope angular resolution ($\delta\Theta_{shower}$). Source A is a point-like source on-axis, because it is contained in one of the small angles and stays in the FOV center. Source B is a point-like source off-axis, it is not at the FOV center. Source C is an extended source because the extension is larger than $\delta\Theta_{shower}$, and partially off-axis.

In Fig. 3.30(panel corresponding to D=0) one can find the distribution of the Dist parameter. The Dist parameter is angular distance between the image core and the source when the source is at the FOV center (on-axis observation). The NDist(x,y) parameter is angular distance between the image core and the source, when, instead, the source is not at the FOV center (off-axis observation, see also Fig. 3.24). The NDist distribution changes significantly with the location (x,y), i.e. with the source displacement, because of geometrical effects, as one can see in 3.30 (panels corresponding to D=0.3,...,1.5). The changes in NDist parameter imply effects on the images shape:

- the Impact parameter increases with the <NDist(source)>;
- the Length parameter may increase with the <NDist(source)>;
- the Width parameter is instead independent from the <NDist(source)>, therefore the ratio $\frac{Width}{Length}$ decreases with the <NDist(source)>. It means that the event-ellipses are more elongated.

3. Rejection of showers affected by Multiple Coulomb Scattering

For small Impact parameter the shower Cherenkov light maximum falls out of the mirror (consequence of the Cherenkov angle). The observed light come for mainly from the shower tail (see subsection 2.6.1, Fig. 2.3 and also subsection 3.3). In this case the events are reconstructed badly and it is needed to reject them. The rejection is performed with a cut on the Dist parameter, in case of the on-axis sources. For the off-axis sources,because their Impact parameter is related to NDist and not to Dist, a cut on NDist has to be used.

4. The leakage of the showers.

   A shower is affected by leakage if a fraction of the image lies outside the camera. For sources observed on-axis the leakage depends on the Dist parameter. That is because the further the image is from the center of the camera, the higher is the probability to be affected by leakage. The leakage depends also on the dimensions of the shower, because the larger is the image of the shower and the higher is the probability of leakages. If a source is off-axis the images of the γ showers will be affected by leakage in accordance with their Dist value. But, again, as in the point 3, the Impact parameter is related to the NDist parameter and not to the Dist. Therefore the distribution of the leakage as a function of the Impact parameter is different for the sources on-axis and for those off-axis.

3.4.2 The False Source Method and the implementation

The False Source Method (FSM, see [39],[40],[41]) is an analysis for the search for the γ rays sources off axis (an alternative method can be found in [50]). It is the method that I implemented for analyzing the data from SN1006. The working principles of this analysis are the following :

1. the Alpha parameter can be calculated in respect to any point over the field of view of the telescope, and not necessarily for the center of the camera. Alpha(x,y) (which is an Alpha calculated in respect to a generic point (x,y)) is the angle between the major axis of the shower image and the straight line between the point (x,y) and the center of gravity of the event.

2. The genuine γ rays are oriented towards the source (see Fig.3.27);

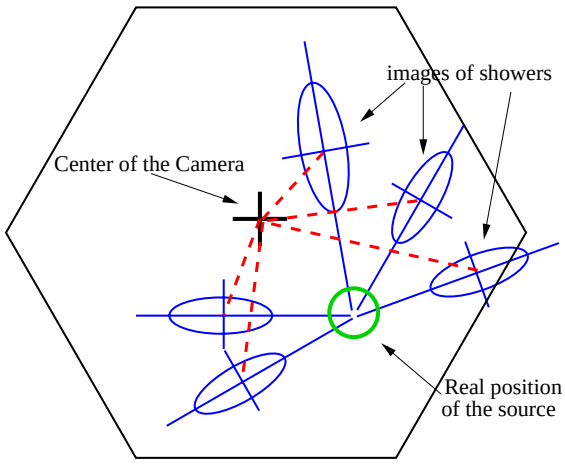

Figure 3.27: An illustration of the orientation of the γ events towards the real source. In the figure one can see: a) the center of the camera (black cross), at the center position it is supposed to be the source with the basic analysis for IACTs; b) the images of the γ events (blue ellipses) oriented towards the real source; c) the position of the real source in the field of view (green circle), it may correspond to the source B in Fig 3.26; d) the Alpha parameter for these events, which is the angle between the major axis of the ellipses and the red dashed lines. One can see that the value of the Alpha for these events is not small.

3. If the source is located in the position (x_0,y_0), then Alpha((x_0,y_0)) is sensitive to that. In particular Alpha((x_0,y_0)) will have a bump at the low values.

Therefore the FSM is analogous to the basic data analysis but many positions are tested as a putative source of the γ rays and not only the center of the camera. A grid of putative sources is defined over the field of view of the camera. The core of the FSM is a loop, at each cycle of which a putative position is considered. The output of the FSM is a scan of the field of view of the telescope. For each considered position it is possible to obtain a measurement of the excess of the γ events (events which are selected as γ events after the subtraction of the residual background) and the significance of such excess. Sky maps for the excess and for the significance are also obtained.

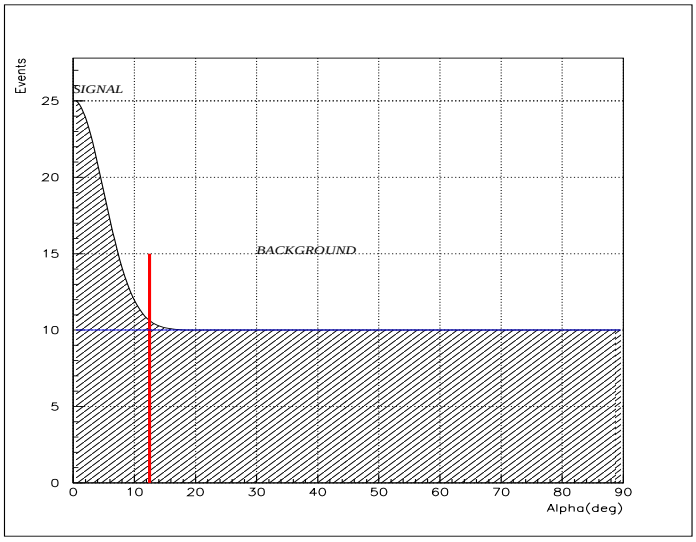

Figure 3.28: An illustration of the Alpha parameter distribution, for a source on-axis. The excess of events is present on the left of the red line (Alpha between 0 and 12.5°) and above the blue line.

The following list describes the implementation of the False Source Method for the analysis discussed in this thesis.

- application of the selection procedure on raw data.

  The FMS procedure used the data after the rejection dominant background of hadrons and the muon background. All the selection cuts listed in section 3.3.6 are applied, except for the ones on the NDist and Alpha parameters. Those parameters have to be recalculated for each position under study.

- loop over the grid of the putative sources.

  The core of the FSM consists of this loop. At each step of the loop one of the putative sources is considered. These source positions are

distributed over the camera plane in a regular orthogonal grid. The spacing between different knots of the grid is chosen in accordance to the angular resolution of the telescope for the γ rays sources. An estimate of the expected angular resolution of the CT1 for the γ rays sources is given by the following relation:

$$\delta\Theta \approx 2 \times \frac{\bar{dist}}{cos(\delta Alpha)} \times sin(\delta Alpha) \approx 0.11^{\circ} \quad (3.23)$$

where $\delta\Theta$ is the angular resolution for the γ rays sources, $\bar{dist}$ is the average value of the Dist parameter (≈ 0.5 for 70° of zenith angle, from samples of experimental events.), δAlpha is the uncertainty in the measurement of the direction of the major axis of the shower (here it is assumed that $\delta\text{Alpha} = 6.25^{\circ}$ = half of the signal region defined by selection cuts).

- recalculation of the Alpha and the NDist parameters.

  For each position (x_{knot},y_{knot}) under study the parameters Alpha(x_{knot},y_{knot}) and Ndist(x_{knot},y_{knot}) are calculated. The calculation is performed by means of basic trigonometry.

- cuts on the NDist and the Alpha parameters.

  A cut on the NDist parameter is applied for each position (x_{knot},y_{knot}). At this point, the distribution of Alpha(x_{knot},y_{knot}), for the events surviving the previous selection procedure, is obtained. The distribution of the Alpha parameter can be divided into two regions:

  1. the *signal region*, at low Alpha values ($< 12.5^{\circ}$ for this analysis, see Fig 3.28). The signal region is populated by events pointing towards the position under study. The eventual γ rays coming from this putative source will cluster in the signal region.
  2. the *background (or control) region* for Alpha between 25° and 80°. The control region is populated by events which do not point to the position under study. These events are very likely to be part of the background.

  The last cut is applied on the Alpha parameter. This cut selects only the events which lie in the signal region. The selection procedure is completed with the cut in the Alpha. The surviving events are named *ON events*. This name reminds that these events are part of a sample of data taken with the telescope pointing *ON* the source.

- extraction of the signal (or events excess).

  The signal (events excess) is composed by those events which satisfy the following requirements:

  1. to survive the selection procedure, therefore they are likely to be γ events;
  2. to lie in the signal region of the Alpha distribution, then these events point to the putative source;
  3. to exceed the number of the events which are part of the background and which satisfy the point 1 and 2 just by chance. (Those background events which mimic γ events are named *residual background*, see section 3.5)

  The signal is calculated in accordance to the following formula:

$$N_{Signal} = N_{On} - N_{Off} \tag{3.24}$$

  where N_{Signal} is the number of the signal events, N_{On} is the number of the selected events from the data sample ON source, N_{Off} is the number of the events of the residual background. The term OFF events reminds that these events are part of a sample of data taken with the telescope NOT pointing at the source. It should be note that exist other methods to determine N_{Off}, if the camera has a circular symmetric sensitivity (see section 3.5).

  The estimate of the residual background is an important step in the analysis chain. In this implementation I used two different methods, which are independent and which give results in agreement each other. These two methods are described in details in section 3.5.

- computation of the significance.

  The FSM provides a measurement of the signal for each of the studied positions. These signals can be generated by a source or by statistical fluctuations. Therefore the significance of the events excess with respect to the expected residual background is computed. The calculation of the significance is performed by applying the theory developed by Li & Ma [51], which is widely used for the γ rays astronomy (for another approach see [52]). The formula considered in the Li & Ma theory is as follows:

$$S = \frac{N_{On} - \alpha N_{Off}}{\sqrt{\alpha \times (N_{On} + N_{Off})}} \quad , \quad \alpha = \frac{t_{On}}{t_{Off}} \tag{3.25}$$

where S is the significance, α (to not be confused with the Alpha parameter) is the renormalization factor between the On and Off observations, N_{On} is the number of events observed with the detector On source, N_{Off} is the number of events observed with the detector Off source, t_{On} is the duration of the observation On source, and t_{Off} is the duration of the observation Off source. The above formula is valid for α in the range between 0.5 and 1.5. Another formula, a more conservative one, has been also used in the implementation of the FSM. Which is :

$$S = \frac{N_{On} - N_{Off}}{\sqrt{N_{On} + 2 \times N_{Off}}} \tag{3.26}$$

The last formula has been used in case of less precise estimates of the background.

- distributions and sky-maps of signal and significance.

  The FSM provides the distributions of the Alpha parameter, signals and the significances for 729 putative sources. The main graphical output consists of :

  1. the distribution of the signals (events excesses);
  2. the sky map of the signals;
  3. the distribution of the significances;
  4. the sky map of the significances.

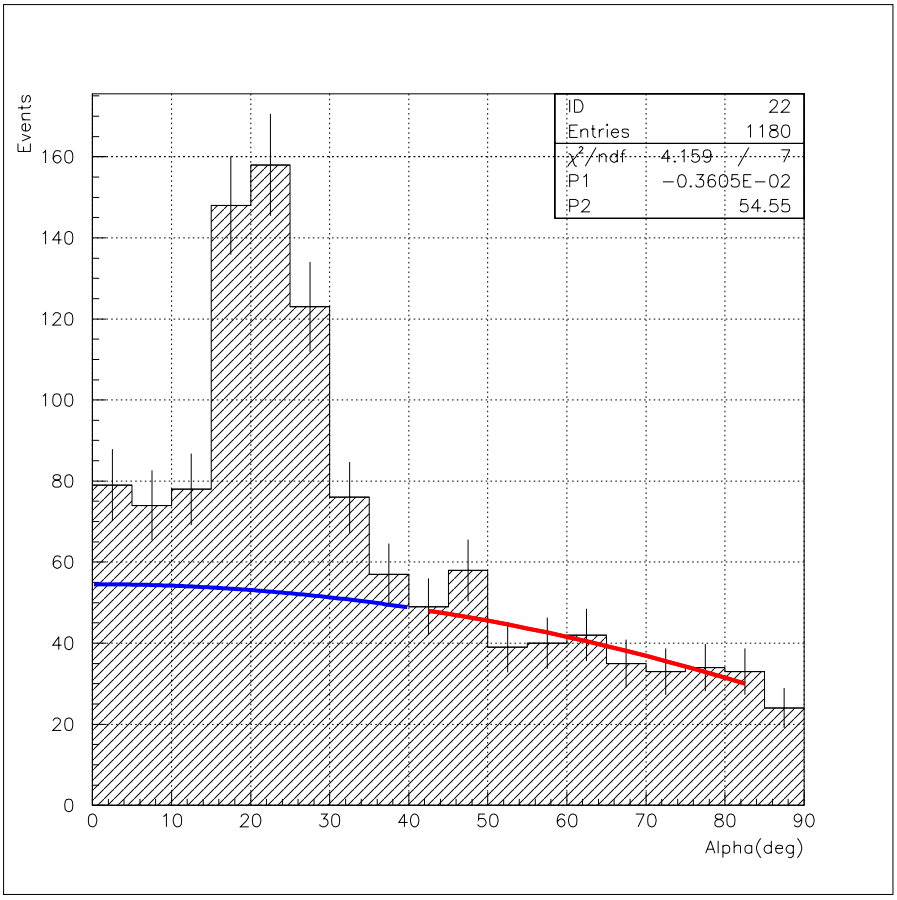

Figure 3.29: The distribution of the Alpha parameter for a strong source observed deliberately off-axis (the data are described in 3.4.3). The signal from the γ source is distributed between 0 and 40° of Alpha, while for a point-like sources on-axis it creates a bump at low Alpha values (alpha $<$ 12.5°). The excess of γ events is obtained with the subtraction of the residual background, fitted with a simple second order polynomial function, without linear term, in the range 40 to 80° (red curve) and extrapolated in the range 0 to 40° (blue curve). The fit parameter for the residual background are reported on the figure. The significance of the excess is above 10σs. Nevertheless majority of this signal would be ignored by the analysis for the point-like sources on-axis.

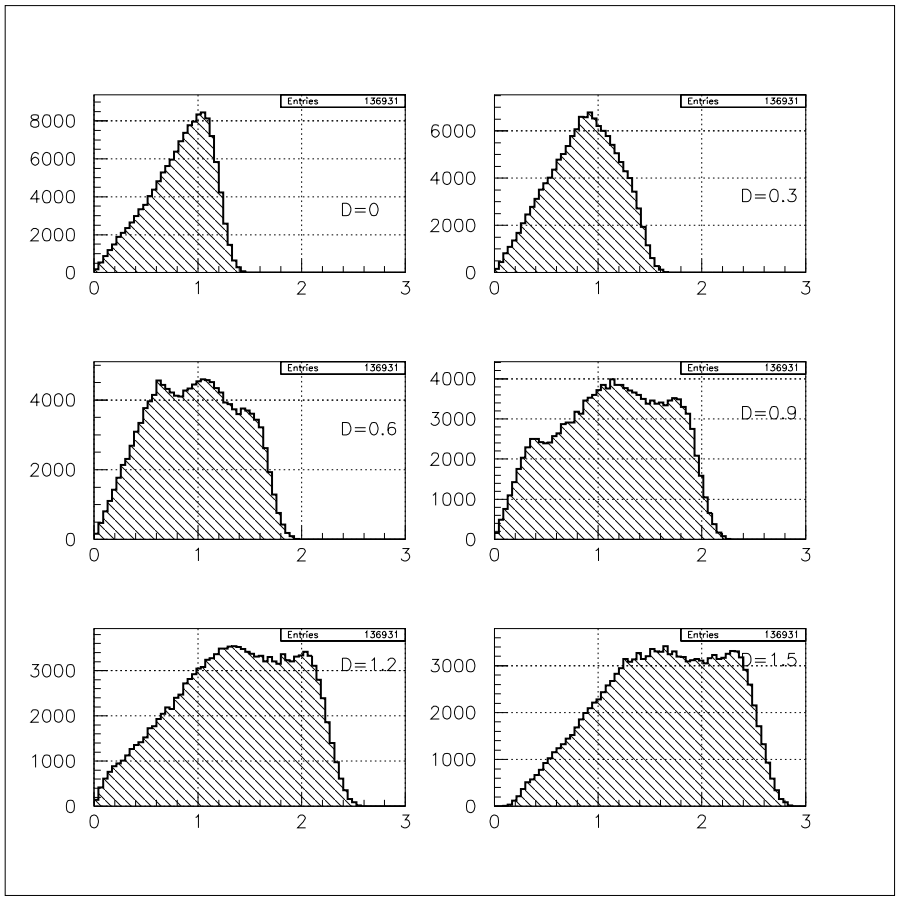

Figure 3.30: Examples of the distribution of the NDist parameter, for six putative source positions, at different displacement (D) from the FOV center. The NDist(x,y) is the angle between the image center of gravity and the location (x,y) over the camera plane. When the location (x,y) is in the center of the camera, then the NDist(0,0) parameter is equivalent to the Dist parameter (as defined by Hillas, see also Fig 3.24). In the six panels, the distributions of NDist for locations with different displacements (indicated as D in the panels, they are expressed in degrees) from the center of the camera are shown. The distribution becomes broader and goes to higher values as the displacement increases.This is expected, in accordance with the geometrical effect. These distributions are made with samples of experimental hadrons. The geometrical effect is expected to work in the same manner for the γ events

3.4.3 FSM analysis tested with experimental data

The reliability of the FSM analysis has been tested. At first the software, that I developed to implement the full analysis, has been checked. After that I investigated the eventual problems in the method. In this subsection I report the final test, which consists of the analysis of an experimental data samples. The main aims of this test are to show that:

- the analysis is capable to find a signal from off-axis sources;
- the analysis does not report fake signals.

Two different data samples have been used:

1. Mkn501 data.

   This data sample consists of observations of the Active Galactic Nucleus (AGN) Mkn501. In 1997 the Mkn501 has undergone strong flares. During a flare the flux of TeV γ rays was highly enhanced and it was possible to detect the sources in a short time with an high significance. During one of these flares, the Mkn501 was deliberately observed off-axis. The source was observed shifting 0.25° both on Right Ascension and in Declination (x and y axes in the CT1 field of view) the telescope. The shift was performed in order to simulate the observation of an off-axis source as well as to test the separation power of two equally strong sources (one off-axis and one on-axis) This observation provided us with a remarkable opportunity to study real γ rays coming from an off-axis source and in a large number. The sample is composed of 63228 events, taken mainly at 10° of zenith angle.

2. OFF-data at large zenith angle.

   The second data sample consists of observations of a dark region of the sky, where there are no sources (OFF-data). The OFF-data used have been observed at large zenith angle, comparable to that of the SN1006. The sample is composed of 136931 events.

The Mkn501 sample contains events at low zenith angle, therefore the Tlow cuts have been used. After that the FSM routine has been applied. For the OFF-data, the final large zenith angle cuts and then the FSM have been used.

The results of the analysis are shown in Figures from 3.31 to 3.40. From these results it is possible to conclude:

1. a signal has been found in the Mkn501 data sample.

2. The Mkn501 signal consists of 177 events and the statistical significance is of more than 12 σ.

3. The signal is, as expected, off-axis and it is at the location of the AGN Mkn501 (see both signal and significance sky maps: Fig.3.33 and 3.34).

4. Both the distribution of the signal and the significance (Fig.3.35, Fig.3.36) have the bulk of that data following a Gaussian distribution around zero. But in both distributions there are data which lie significantly outside the Gaussian distribution. They correspond to the positions where the signal has been found.

5. No signal has been found in the OFF-data, as it was expected.

6. The alpha distribution for the OFF-data, relative at the same region where the Mkn501 signal has been found, is fully consistent with the residual background (Fig.3.32, a so-called *flat distribution*). This excludes camera-dependent effects for that region.

7. Both the OFF-data distributions of the signal and the significance (Fig.3.39, Fig.3.40) follow a Gaussian distribution, which is consistent with no signal observed.

8. Both the OFF-data sky maps of the signal and the significance (Fig.3.37, Fig.3.38) show no signal, but only random fluctuations.

9. The results of the test are in full agreement with what was expected.

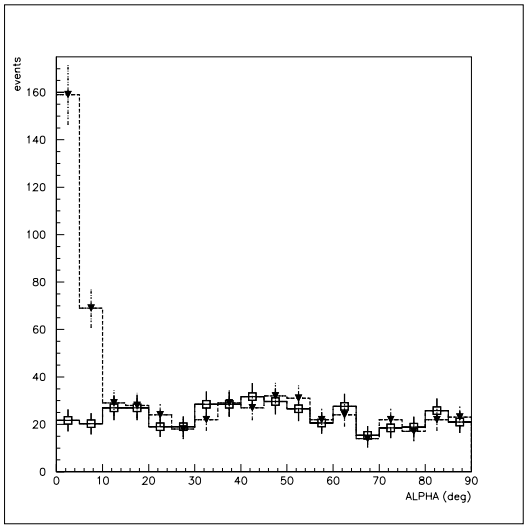

Figure 3.31: The distribution of the Alpha parameter (Mkn 501) for the position of the source. The black triangles are the events after the selection (ON events), the empty squares are the residual background.

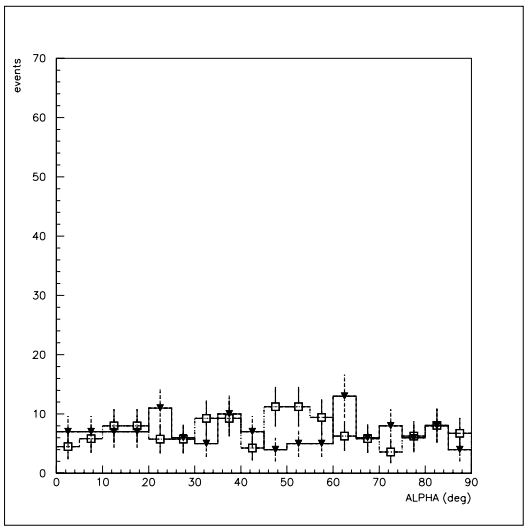

Figure 3.32: The distribution of the Alpha parameter (OFF-data). This distribution is for the same region of the field of view as in Fig.3.31. The black triangles are the events after the selection (ON events), the empty squares are the residual background. Please note the y axis scale is not the same as for the previous plot.

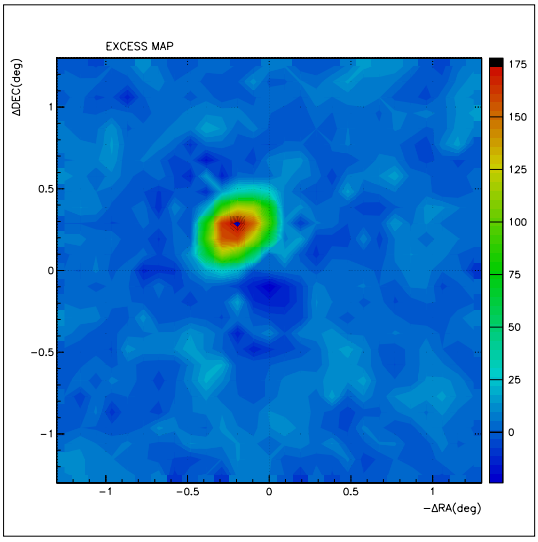

Figure 3.33: The sky map of the events excess (Mkn 501).

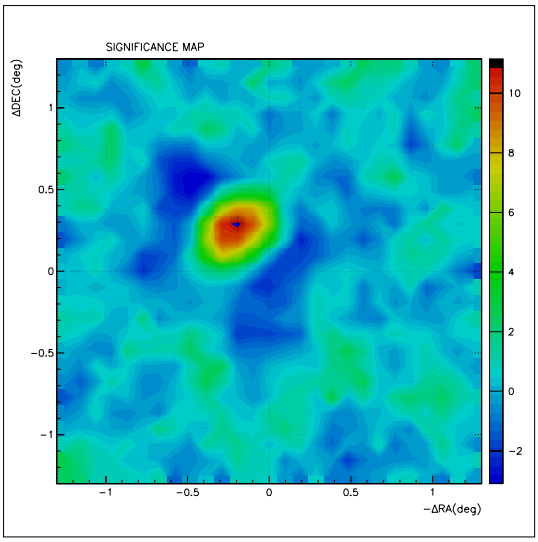

Figure 3.34: The sky map of the signal significance (Mkn 501).

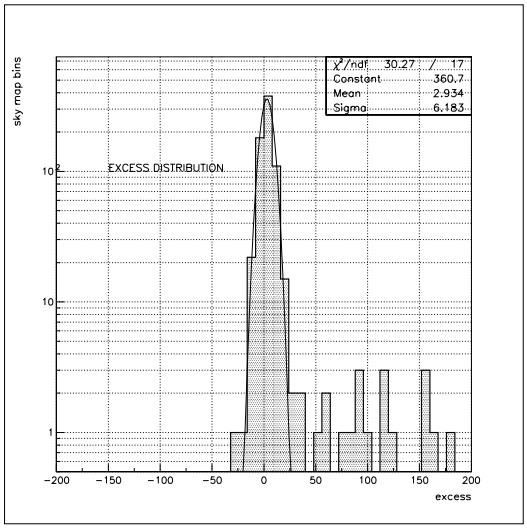

Figure 3.35: Distribution of the events excess, for the FSM sample (Mkn 501, off-axis sample). Here the excess produced by the Mkn 501 is clearly outside the Gaussian fit (above 50).

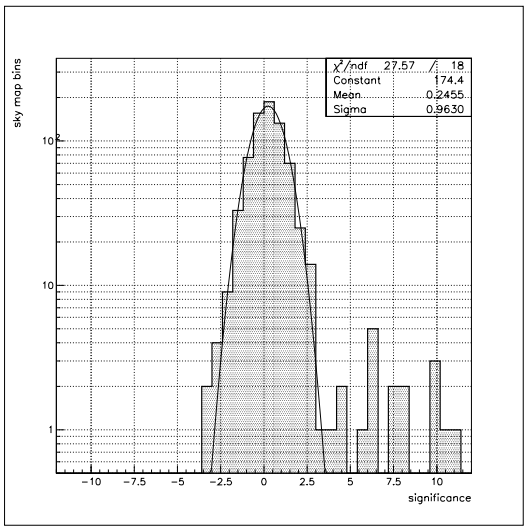

Figure 3.36: Distribution of the signal significance, for the FSM sample (Mkn 501, off-axis sample).

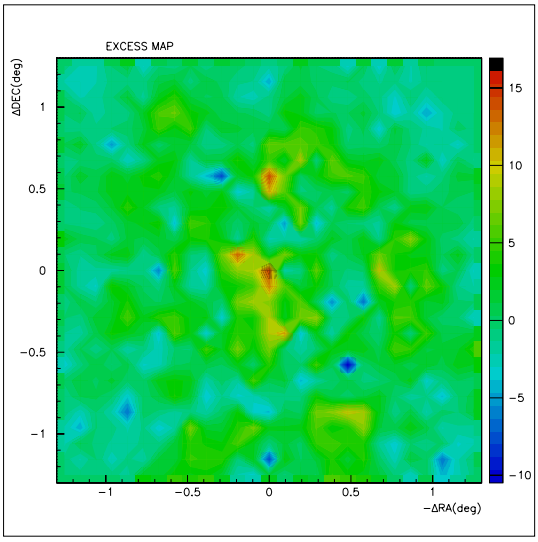

Figure 3.37: The sky map of the events excess (OFF-data).

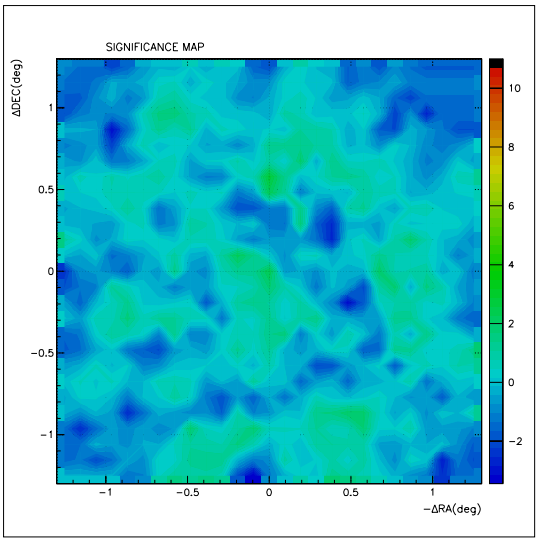

Figure 3.38: The sky map of the signal significance (OFF-data).

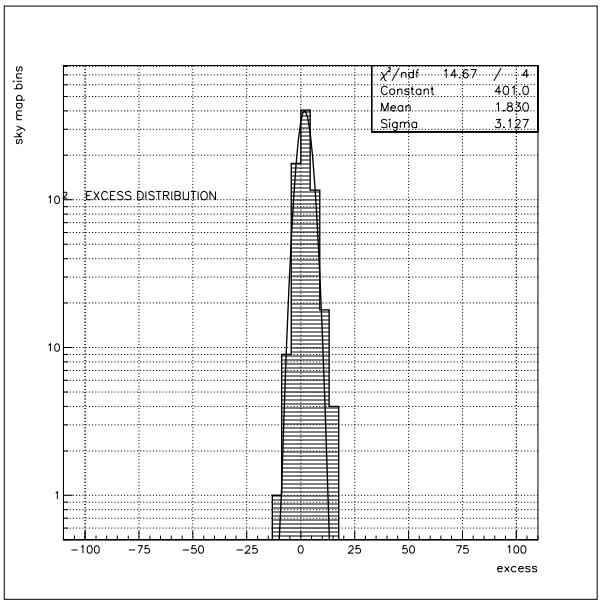

Figure 3.39: Distribution of the events excess (OFF-data).

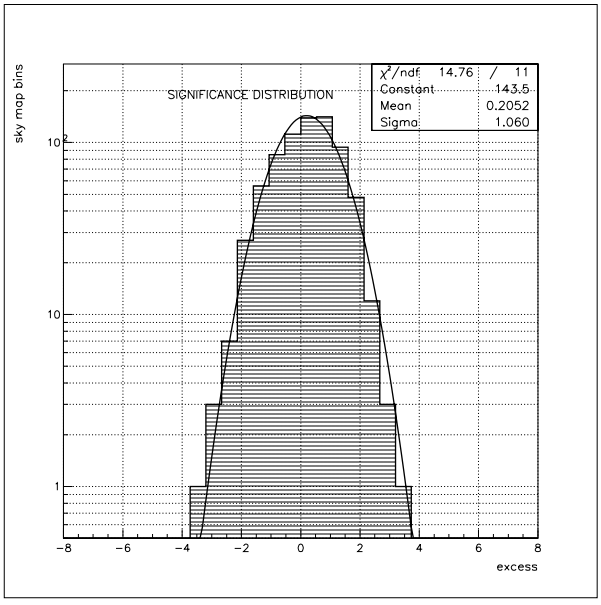

Figure 3.40: Distribution of the signal significance (OFF-data).

3.5 Residual background

The residual background is composed of those background events (hadrons and muons in the SN1006 case) that satisfy just by chance the selection criteria. The main reasons, for which the knowledge of residual background is important for the IACTs analysis, are:

1. A small number of collected γ events from the TeV γ rays sources.

   An IACT, operated in the TeV energy range, collects a small number of γ rays from a source in a given time. For example a raw estimate of the number of γ rays collected form the Crab Nebula is:

   $$\frac{dN_\gamma}{dt}(E > 1\ TeV) \ = \ \Phi \ \times \ A_{eff.} \ \approx \ 25\ hour^{-1} \tag{3.27}$$

   $$\frac{dN_\gamma}{dt}(E > 0.7\ TeV) \ \approx \ 44\ hour^{-1} \tag{3.28}$$

   where $\frac{dN_\gamma}{dt}$ is the γs differential rate, $\Phi = 1.75 \times 10^{-11} cm^{-2} sec^{-1}$ is the integral flux of γ rays from the Crab Nebula and $A_{eff.} = 4 \times 10^8 \mathrm{cm}^2$ is the typical effective collection area for an IACT at a low zenith angle. The differential rate multiplied by the γ selection efficiency (ϵ_γ) gives the differential rate after selection (*after cuts*).

2. A large number of collected background events.

   An estimate for the differential rate of hadrons is:

   $$\frac{dN_h}{dt} \ = \approx \ 2.5\ Hz \ \approx \ 9000\ hour^{-1} \tag{3.29}$$

   .

3. A non negligible number of the *residual background* events, if compared to the γ ray events, also after the proper background suppression.

   Point 3 is a combined effect of points 1 and 2. For example, if we assume the Supercuts analysis as a reference, then the estimate for the residual background is:

   $$\left(\frac{dN_h}{dt}\right)_{residual} \ = \ \epsilon_h \times \ \frac{dN_h}{dt} \approx 52\ hour^{-1} \tag{3.30}$$

   where $(\frac{dN_h}{dt})_{residual}$ is the residual background differential rate, ϵ_h is the hadron efficiency of the Supercuts and $\frac{dN_h}{dt}$ is the hadron differential

rate assumed in point 2. The residual background differential rate should be compared to the γs one.

From the previous comparison one can conclude that it is necessary to evaluate the residual background and to suppress it.

A common method of evaluation for the residual background is to observe a sky region (the so-called control position) in which there are no sources present. Then the residual background can be directly obtained. There are two items related to the previous method:

- The time to be spent on observing the control position should be equal or comparable to that spent on observing the source. Therefore the time needed for an observation increases of a factor ≈ 2.
- The background differential trigger rate depends on the observed sky region, this is because of zenith angle, stars density, and other factors. Therefore the residual background measured at the control position can be different from that expected at the source location. Systematic effects can arise from this difference. The most demanding condition is the observation at large zenith angle.

3.5.1 Fit of the Alpha parameter distribution

The *fit of the Alpha distribution* is a method to evaluate the residual background. The Alpha distribution is divided into the *signal region* and into the *background region* (see 3.4, 3.4.2). The method consists of the fit of the background region, with a residual background model, as shown in Fig.3.41. A simple model consists of a second order polynomial function (in Alpha), without the linear term (the gradient in Alpha=0 should be zero, as consequence of the folded Alpha distribution):

$$N(Alpha) \;=\; N_0 \;+\; \lambda \;\times\; Alpha^2 \tag{3.31}$$

where N(Alpha) is the the residual background as a function of the Alpha parameter, N_0 is the background level at Alpha = 0 and λ is a parameter, which is evaluated with the fit procedure. It describes a uniform (nearly *flat*) distribution of the Alpha parameter, as expected for the cosmic rays events, because of their isotropic distributed incoming direction. The second order term accounts for the non-uniform detection efficiency over the FOV, which shows up as a non-uniform Alpha parameter distribution. After the fit, the residual background model can be extrapolated in the signal region. This method does not need dedicated observations of a control region. It

is also possible to avoid the systematic effects arising because of different trigger rates with the source and the control dedicated observations.

3.5.2 The *Ring* background

The so-called *Ring background method* is another procedure to evaluate the residual background for an off-axis source. The Ring background method can be resumed with the following steps:

- Definition and study of the source position.

  In the following analysis, the source position is defined as: the location of the investigated astronomical object. Such a sky position is projected somewhere over the telescope field of view. The source position is known with some uncertainties, for example the pointing errors. Data used for the study of the source position are selected and analyzed as described in the previous sections. The NDist cut (see section 3.3.6) divides the data sample into two independent sub-samples (Fig.3.42) . They are:

  1. the events which satisfy the condition

     $$NDist_{min} < NDist(X_0, Y_0) < NDist_{max} \tag{3.32}$$

     where the NDist parameter is calculated with respect to the source position (X_0,Y_0) under study. These events are used only for the study of the source position.
  2. the events which do not satisfy the above mentioned relation. They can be used to study one or more control positions.

- Definition and study of one or more control positions (C.P.s).

  One or more control positions are chosen over a ring (Fig.3.43). This ring is centered around the camera center. The mean radius of the ring is equal to the distance source position-camera center. In this way, the telescope sensitivity is almost constant over the ring. In fact, the CT1 sensitivity has, at first approximation a radial symmetry. The sensitivity has a maximum around the geometrical center of field of view, and drops radially. A minor dependence on the zenith angle difference (i.e. 3°) across the camera is also present. The region around the source is excluded from the ring, in order to avoid contamination with the eventual signal.

- Integration of all the Alpha parameter distributions of the C.P.s (Ring Alpha distribution).

  All the control positions are studied. With this implementation, each event is used, but *only one time*. Therefore an event may be used either only for the source, or only for one of the control positions. Few control positions are enough to use all the events which are left after the analysis of the source position. The Alpha parameter distribution is obtained for each of the control positions (C.P.s). After that, all the Alpha distributions are summed up to a single one (Ring Alpha distribution).

- Normalization of the Ring Alpha distribution to the source one.

  The Ring Alpha distribution is normalized to the source Alpha distribution. In order to perform the normalization, the following ratio is calculated:

$$R_{Norm} = \frac{Alpha_{Bck}(Ring)}{Alpha_{Bck}(Source)} \tag{3.33}$$

  where Alpha$_{Bck}$(Ring) is the number of events in the background region of the Ring Alpha distribution, Alpha$_{Bck}$(Source) is the number of events in the background region of the source Alpha distribution. R$_{Norm}$ is therefore the ratio between the number of background events observed in the Ring region and those observed at the source. Then the expected residual background at the source position is:

$$N_{Residual} = R_{Norm} \times Alpha_{Sgn}(Ring) \tag{3.34}$$

  where Alpha$_{Sgn}$(Ring) is the number of events in the signal region of the Ring Alpha distribution.

In Fig. 3.44 three examples of the residual background evaluation with the Ring method are shown. The used sample contains OFFdata (pure background) at a low zenith angle. The Tlow cuts have been applied. After that, a source position has been defined for each of the three examples (respectively at 0.2, 0.4 and 0.6° from the camera center). The data sample is made of pure background events, then, by definition, the source Alpha distribution contains only the residual background. Therefore the Ring Alpha distribution should reproduce the source Alpha distribution, in order to evaluate properly the residual background. In table 3.21 the statistics for

Source-Camera center Angle (°)	Alpha$_{Bck}$(Ring)	Alpha$_{Bck}$(Source)	N$_{Norm}$
0.2	5778	9702	0.595±0.009
0.4	5089	13801	0.369±0.006
0.6	4088	15016	0.272±0.004

Table 3.21: The statistics for the examples given in Fig.3.44. Alpha$_{Bck}$(Ring) is the number of events in the background region of the Ring Alpha distribution, Alpha$_{Bck}$(Source) is the number of events in the background region of the source Alpha distribution. R$_{Norm}$ is the normalization ratio factor.

the three examples are listed. The other two examples of the Ring method are shown in section 3.4.3 (Fig. 3.31 and 3.32). From the previous discussion and from the performed tests, it is possible to conclude that:

1. The Ring background method is a reliable technique for the estimation of the residual background.

2. This method does not need dedicated observation for the estimation of the residual background.

3. The systematic effects, related to eventual different trigger rates for the source and for the control dedicated observations, are avoided.

4. An higher statistics can be obtained, in respect to the Alpha fit method, which allows a better evaluation of the significance of an eventual signal.

5. The symmetry of the Ring region allows one to integrate background over the ϕ angle (polar angle in the camera field of view) and to get rid of the possible camera asymmetries, which are generated mainly by the statistical fluctuations.

6. The Ring method can not be applied for sources at a distance from the camera center $< 0.11°$

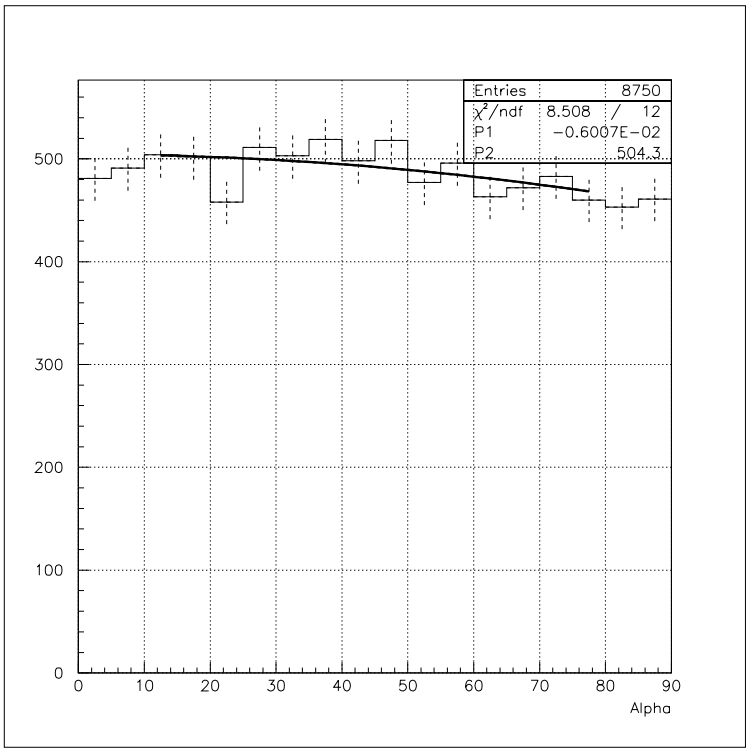

Figure 3.41: Example of a fit of the Alpha parameter distribution. A similiar Alpha distribution and fit is obtained for each of the grid points used with the FSM. Here, the Alpha parameter distribution of a sample of experimental hadrons, after the selection procedure (without cut in Alpha), is fitted with a residual background model. The model is described in the text. Here, N_0 is indicated as P2 and λ as P1. The black solid line shows the fitting function.

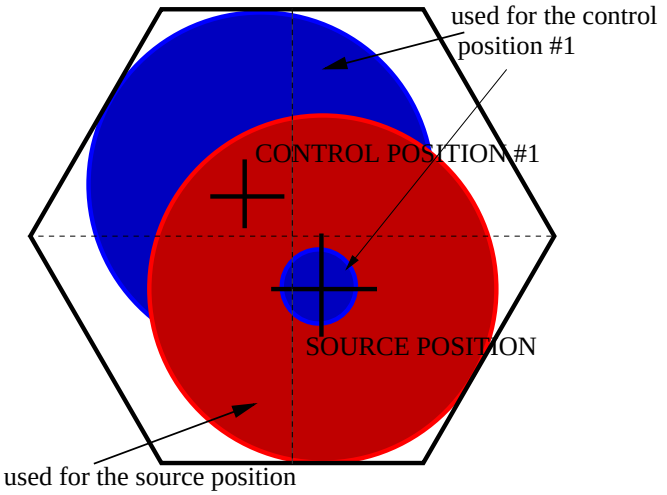

Figure 3.42: An illustration of the source and the control position subsamples. The events with center of gravity (c.o.g.) in the red region are selected by the NDist cut (referred to the source position) and are used to study only the source position (the black lower cross).The events with center of gravity (c.o.g.) in the blue region can be used for the control position #1, because they are not selected by the NDist cut (referred to the source position) . The regions dimensions and shapes are modified for the illustration. Note that the method requires a minimum separation between source and control position.

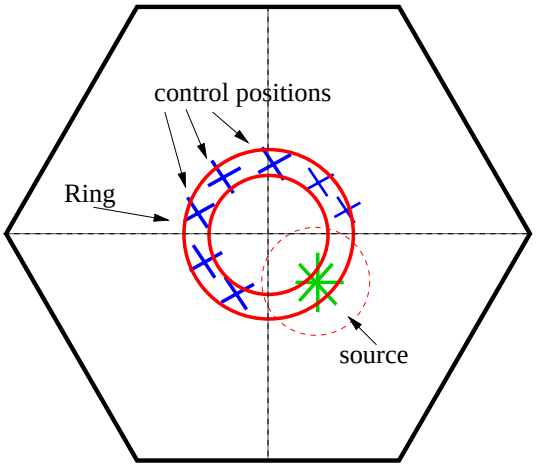

Figure 3.43: An illustration of the source and control positions configuration. The control positions (blue crosses) lie over a ring (red double circle), which is centered in the the field of view center. The mean radius of the ring is equal to the distance between the source position (green asterisk) and the camera center. This configuration allows to have a constant sensitivity over the ring. (The CT1 sensitivity has a maximum at the center of the camera and drops radially.) The region around the source is excluded from the ring, in order to avoid contamination with the eventual signal.

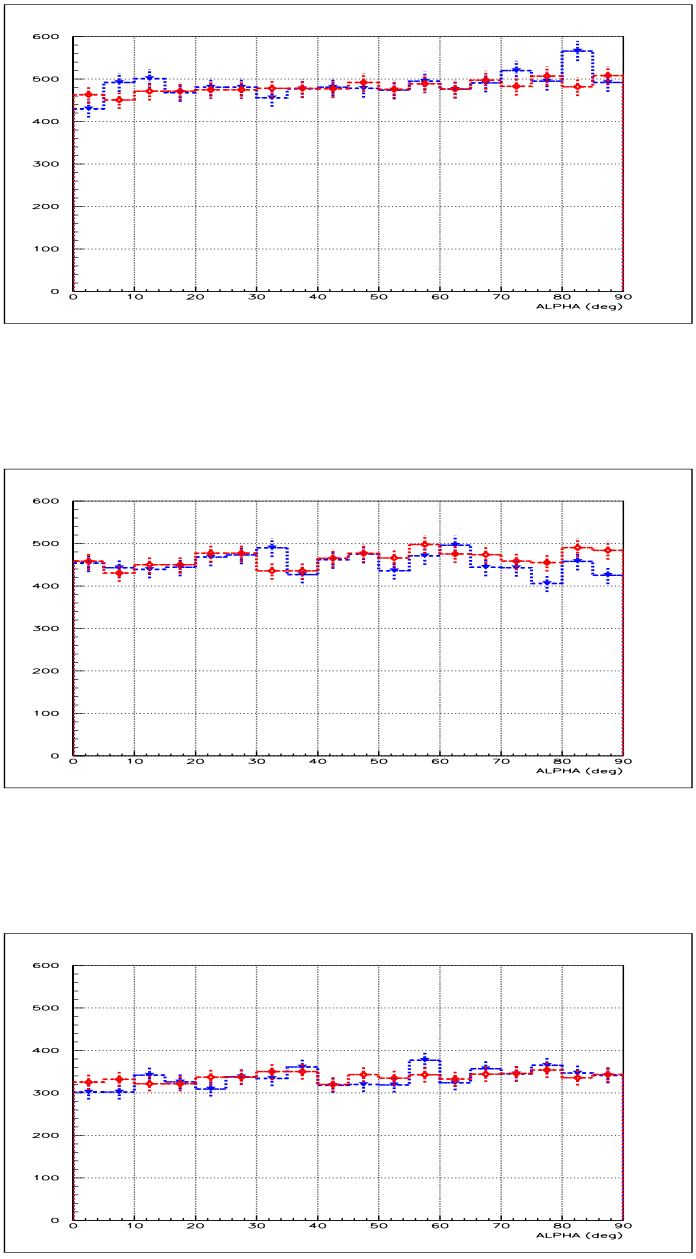

Figure 3.44: The capability of the Ring method in reproducing the residual background is shown with these three plots. The blue histograms are the Alpha distribution of the source and the red ones are the Ring Alpha distribution. There is no signal in the sample (i.e.pure hadronic background). Therefore red and blue histograms have to coincide, as it can be seen in the figure. The three source positions are (from the bottom to the top) at 0.6, 0.4 and 0.2° from the camera center.

3.6 Calibrations

One of the purpose of this study is the measurement of the energy distribution of γ rays coming from the source. In order to perform such a measurement few calibrations are needed. These calibrations are obtained using MC simulations of the TeV γ rays at different energies. The most important parameters and relations, obtained with the calibrations are:

1. the relation to reconstruct the Impact parameter and the energy of the individual γ candidates.
2. the effective collection area as a function of the γ energy;
3. the effective collection area for the calculation of the integral flux of the source;

3.6.1 Monte Carlo simulations

Monte Carlo simulations of γs and hadrons events have been widely used, in order to perform the present analysis.

The CT1 analysis group produced an archive of Monte Carlo simulations to be used for the experimental data analysis (Dr. D. Sobczynska is the principal contributor to these activities). The main goals of the Monte Carlo simulations are:

- to reproduce the Cosmic Rays air showers;
- to reproduce the detector response;
- to allow the calibrations and the optimizations, which are needed for the telescope data analysis.

The full chain for the Monte Carlo simulations production can be summarized in the following steps (see also [47]):

1. The air showers are simulated by means of the code CORSIKA ([49], [53]), from the release 5.62 to more recent ones. With this code the properties of the primary particles, which generate the shower, can be chosen. In particular the primary type (γ or hadron), the zenith angle, the energy range and distribution, the Impact parameter range are given as input to the program. The Earth's magnetic field and the Rayleigh and Mie scattering are taken into account by the code, by means of specific models. The most important output from this step is the Cherenkov light produced by the showers.

2. The simulations produced by means of CORSIKA are used as input to a program which simulates the detector. The following parts are considered in order to simulate the detector:

   (a) The Reflector. The geometry of the reflector is reproduced, the mirror imperfections and reflectivity are included.

   (b) the Camera. The camera also is reproduced. The Winston cones, the photocathode quantum efficiency and its fluctuations, and the photoelectron collection efficiency are included.

   (c) the electronics for the data acquisition.

3. The NSB (Night Sky Background) is added to the Cherenkov light produced by the showers. This NSB noise is obtained by using direct measurements with the CT1 telescope. Therefore for each source the specific NSB, which is measured at the same Declination and Right Ascension of the source (and at the same time), is used.

4. The output of the step three is subsequently analyzed by means of the same software chain, which is used for experimental data.

The CT1 Monte Carlo simulations archive has been used to perform many investigations, for example [54] (which is the recently published analysis of the Mkn421 experimental data from 2001).

3.6.2 Effective collection area

The calculation of the Effective collection area is related to the study of the integral and differential γ rays energy spectrum. The γ rays flux is defined as :

$$\Phi(E) = \frac{d^2N}{dA\ dt} \approx \frac{N(E)}{A_{coll}(E)\ T_{expo}} \tag{3.35}$$

where $\Phi(E)$ is the integral flux, N(E) is the number of particles (γs) with energy E collected during the time T_{expo} over the collection area A_{coll}(E). The collection area A_{coll}(E) is written as a function of energy because of the efficiency of the particles collection being dependent on the particles energy. In general the collection area is also a function of the zenith angle (A_{coll}(E,θ)). For the SN1006 case, the observations were made within a narrow zenith angle range (the majority of events are in 2 degrees). The MC simulations (z.a. = 72°) match this range with sufficient accuracy. Therefore it is possible to simplify the following discussion and to omit the

variation in θ. The differential flux is the derivative of the integral one, in respect to the energy:

$$\frac{d\Phi(E)}{dE} = g(E) \tag{3.36}$$

here the differential flux is indicated by the function g(E), which, for many TeV γ sources, is approximated as a power law $C \times E^{-\delta}$, where C is the scale constant and δ is the spectral index (photon index). A detector, having a collection area A_{coll}, operated for a time T_{expo}, collects, therefore, the following number of particles:

$$\Delta N = \int_{E_0}^{E_1} g(E)\ A_{coll}(E)\ T_{expo}\ dE \tag{3.37}$$

where the collected particles have energy in the range $[E_0,E_1]$. E_0 is commonly indicated as the energy threshold, while E_1 is set to infinity, as the number of collected particles decreases fastly with the energy. For the calculation of the integral flux it is needed to define an *effective collection area*:

$$< A_{coll} > = \frac{\int_{E_0}^{E_1} g(E)\ A_{coll}(E)\ dE}{\int_{E_0}^{E_1} g(E)\ dE} \tag{3.38}$$

which is the weighted sum of the collection areas at different energies. In this sum the weights are given by the expected fraction of particles of a given energy. Therefore the *effective collection area* for the integral flux depends on the assumed differential flux g(E) and on the energy threshold. In accordance to the previous definitions it is possible to calculate the variation of particles integral flux in the energy range $[E_0,E_1]$, with ΔN and $<A_{coll}>$, as:

$$\Delta\Phi(E_0 < E < E_1) = \frac{\Delta N(E_0 < E < E_1)}{T_{expo}\ < A_{coll} >} = \int_{E_0}^{E_1} g(E)\ dE \tag{3.39}$$

The effective collection area given by the geometrical collection area multiplied by the efficiency of the particle collection at Impact parameter r and Energy E

$$A_{coll}(E) = \int_{I_0}^{I_1} P(E,r)\ r\ dr \approx \sum_j P(E,r_j)\ (r_{j+1}^2 - r_j^2) \tag{3.40}$$

where P(E,r_j) is the probability to detect (after all cuts) a particle of energy E and Impact parameter r_j. Contrary to simple expectation P(E,r_j) is not 0 or 1, because of the statistical nature of the shower development. In the last term of the equation, the discrete variables are used and therefore the integral is substituted by the sum over the index j, which runs over all the relevant Impact parameter bins. The calculation of the *effective collection area* for the integral flux, with the discrete variables, becomes:

$$< A_{coll} > \approx \frac{\sum_i \Big(g(E_i)\ (E_{i+1} - E_i)\ \sum_j P(E_i, r_j)\ (r_{j+1}^2 - r_j^2) \Big)}{\sum_i g(E_i)(E_{i+1} - E_i)} \tag{3.41}$$

where the index i runs over all the relevant energy bins, the index j runs over all the relevant Impact parameter bins. Using the previous definitions, a formula for the calculation of the differential flux is :

$$\frac{d\Phi(E_i)}{dE} \approx \frac{d}{dE} \int_{E_{dw}}^{E_{up}} g(E)\ dE \approx \frac{1}{\Delta E} \frac{\Delta N(E_i)}{T_{expo}\ A_{coll}(E_i)} \tag{3.42}$$

where ΔN(E$_i$) is the number of the collected events in the i^{th} energy bin, A$_{coll}$(E$_i$) is the collection area for the i^{th} energy bin, T$_{expo}$ is the exposure time, and ΔE is the energy bin amplitude.

The effective collection area can not be calculated analytically. The standard method is to calculate it with MC simulations. I used the following procedure:

- The MC simulations have been pre-processed using the same NSB light level as with the experimental data under study.
- The trigger and the cuts efficiency have been calculated as a function of the Impact parameter and the Energy, for the MC events (P(E$_i$,r_j) in the previous discussion).
- The effective collection area as a function of the energy (A$_{coll}$(E$_i$)) has been calculated (as discussed above).
- The effective collection area for the integral flux ($< A_{coll} >$) has been calculated for the various spectral indices and at a fixed energy threshold.
- The change in the acceptance as a function of the camera position has been included in the calculation and the effective collection area

has been obtained also as a function of the distance form the camera center.

- The effective collection areas have been directly evaluated with MC simulations, which have maximum Impact parameter of 500 meters. (MC simulations with a larger Impact parameter require a prohibitively high amount of CPU-time). The maximum Impact parameter used will be considered for the calculation of the fluxes.

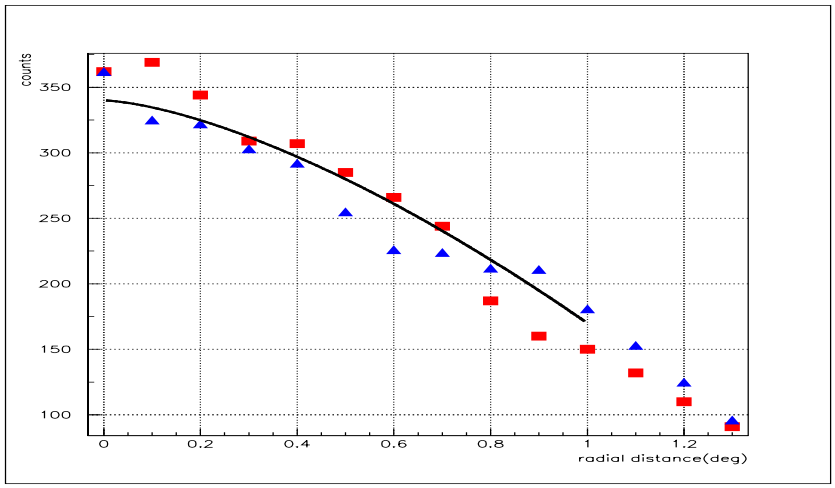

Figure 3.45: The radial acceptance profile. Here two experimental acceptance profiles, obtained from two different radial paths are shown (SN1006 data after selection cuts) with the red boxes and the blue triangles. The calculated acceptance, is also shown with the black line.

The MC data sample used was composed of 28630 events before trigger, from which 10689 passed the trigger condition. The simulations have been done at 72° of zenith angle, spanning between 5 and 50 TeV in energy, and between 0 and 450m (with a tail up to 500m) in Impact parameter.

The effective collection areas after the trigger and after the selection cuts can be found in Fig. 3.46. The energy threshold E_0, in this context, is

index δ	$< A_{coll} >$ (m^2)	$< A_{coll} >$ (m^2)	$< A_{coll} >$ (m^2)
	E_0=10 TeV	E_0=18 TeV	E_0=25 TeV
-1.0	37054	48791	49497
-1.5	34018	48985	50805
-2.0	30772	48953	52084
-2.5	27579	48708	53321
-3.0	24643	48279	54504

Table 3.22: The effective collection areas as function of photon index and energy threshold.

defined as the energy at which the differential rate has its maximum; where the differential rate is the rate at which the γ rays are detected (this is the conventional definition used in ground-based γ astronomy).

The differential rate is given by multiplying the effective collection area times the source differential flux (g(E) $\times$ A_{eff}(E)). It is, in general, weakly dependent on the assumed differential flux (g(E)) of the source. The differential rates for 5 different source differential fluxes are shown in Fig. 3.47.

The effective collection areas ($< A_{coll} >$) for the integral flux calculation for different energy thresholds (E_0) and spectral indexes are summarized in table 3.22.

The *camera radial acceptance profile* is shown in Fig. 3.45. The camera acceptance changes with the distance form the camera center because of the edge effects and the position-depended cuts, which have been applied for analysis. There is an additional small effect in ϕ, which is produced by the hexagonal shape of the PMs arrangement in the camera. Within 0 and 1° of radial distance the acceptance can be approximated by the function:

$$R(\delta) \;=\; \frac{Acc(\delta)}{Acc(0)} \;=\; (1 - 0.5\ \delta^{1.5}) \qquad (3.43)$$

where R(δ) is ratio between the acceptance at an angular off-set δ and the maximum acceptance (at the camera center).

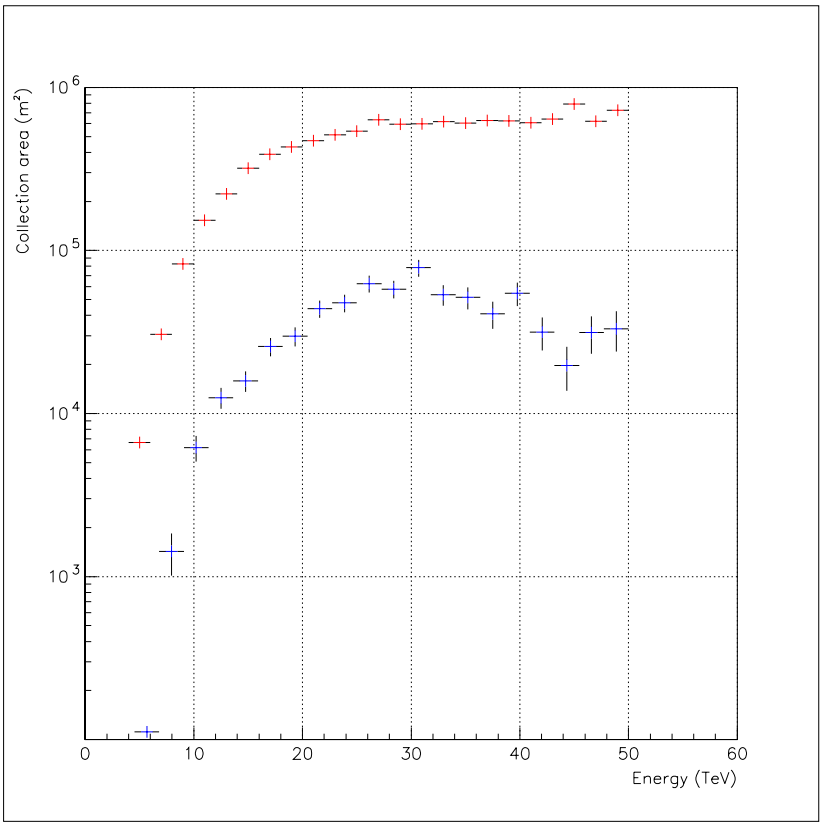

Figure 3.46: The effective collection area for γs , as a function of the energy, for a zenith angle of 72°. The red points are the effective collection area after the trigger. In this case the selection criterium is the harware trigger of the telescope. The blue points are the effective collection area after the selection cuts, as described in section 3.3

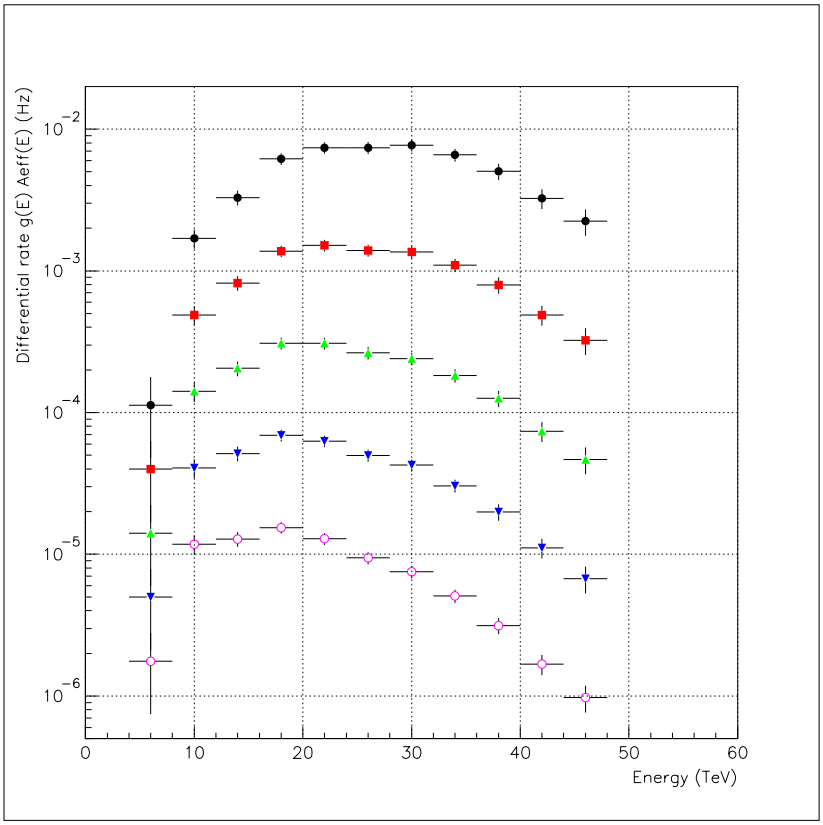

Figure 3.47: The differential rate, as an energy function, for a zenith angle of 72°. The differential rate is given by the effective collection area multiplied by the source differential fluxes (g(E) × A_{eff}(E)). Here are the differential rates for 5 different source differential fluxes in the form of C×$E^{-\delta}$. For all of them, the scale constant C is set to $10^{-7} m^{-2} sec^{-1}$. The spectral indices are (from top to bottom) -1.0 for the black dots, -1.5 for the red full squares, -2.0 for the green up-pointing triangles, -2.5 for the blues down-pointing triangles and -3 for the violet empty circles. It is possible to see that the maximum differential rate moves up from 30 TeV, with spectral index -1.0, to 18 TeV, with spectral index -2.0 and smaller.

3.6.3 Energy and Impact parameter reconstruction

The purpose of the energy calibration is to obtain a measurement of the energy for each of the selected γ events. There are no available calibrating sources for the IACTs. Therefore the energy calibration is achieved by means of the MC simulations and cross-checking the measured energy spectrum of few *standard candles* (Crab Nebula, for example).

For the SN1006 data analysis, the energy calibration procedure was the following:

- definition of the reconstruction formulae for the Impact parameter and the energy;
- fixing of the free parameters in the formulae, by means of minimization routine;
- comparison of the reconstructed Impact parameter and the energy for a sample of MC simulations.

The reconstruction of the Impact parameter is based on the following empirical formula:

$$Imp \;=\; (a\ Dist \;+ b\ Length + d) \times h(\theta) \;= \tag{3.44}$$

$$=\; \alpha_{Imp}\ Dist \;+ \beta_{Imp}\ Length + \delta_{Imp} \tag{3.45}$$

with

$$\alpha_{Imp} \;=\; a \times h(\theta)\ ,\ \beta_{Imp} \;=\; b \times h(\theta)\ ,\ \delta_{Imp} \;=\; d \times h(\theta) \tag{3.46}$$

where Imp is the estimate of the Impact parameter; Dist and Length are two image parameters, h(θ) is the dependence on the zenith angle θ and α_{Imp}, β_{Imp} and δ_{Imp} are the free parameters to be fixed by means of the minimization procedure. This linear combination exploits the geometrical relations between the Impact parameter and the Dist and Length parameters, as illustrated in Fig.3.48. The observations of the SN1006 have been performed within a narrow zenith angle range, as already mentioned for the effective collection area calculations. The energy calibrations have been performed with the MC simulations of the γ events at zenith angle of 72°, which well match the observations. Therefore the factor h(θ) is constant and is integrated into the free parameters. At first the Impact parameter is calculated, subsequently it is used for the energy reconstruction:

$$En \;=\; (f\ Size \;+ g\ Imp + m) \times l(\theta) \;= \tag{3.47}$$

$$= \alpha_{En}\ Size \ + \beta_{En}\ Imp + \delta_{En} \tag{3.48}$$

with

$$\alpha_{En} \ = \ f \times l(\theta)\ ,\ \beta_{En} \ = \ g \times l(\theta)\ ,\ \delta_{En} \ = \ m \times l(\theta) \tag{3.49}$$

where En is the estimate of the energy, Size is the image parameter, Imp is the Impact parameter, α_{En}, β_{En} and δ_{En} are the free parameters to be fixed by means of the minimization procedure.

The formula for the energy reconstruction is a linear combination of image parameters and the Impact parameter. The formula terms are explained by the following points:

1. The total amount of Cherenkov light produced by a shower is, at the first order, proportional to the shower energy (energy of the parent primary particle). With a telescope one samples a fraction of the shower light, i.e. the Size parameter is related to the initial energy. Below 1 TeV the radial dependence of the shower light-pool is mainly flat, up to 130m. Therefore the measured light is a good energy estimate. In case of partial leakage of the shower image, it is needed to use the the Size density (Size divided by Width $\times$ Length) instead of the Size parameter. With the present analysis, the events fully contained in the camera (no Leakage) are selected, therefore it is possible to use the Size parameter.

2. The Impact parameter introduces a correction for the shower position (distance from the detector) and inclination. At energies higher than 1 TeV the light distribution has a strong radial dependence. Therefore one must use the Impact parameter and the radial distribution function, in order to determine the energy.

3. The constant term is used for an eventual energy scale bias.

4. For the dependence on the zenith angle (the factor l(θ)), a similar argument, as for the Impact parameter (the h(θ) factor), has been applied.

The fixing of the free parameters of the Impact parameter and energy formulae has been performed with a minimization routine. The *MINUIT* package, of the CERN Program Library, has been used. The minimization has been performed on the function:

$$f(X)_m \ = \ \Delta(X)^2 \ + RMS(X) \tag{3.50}$$

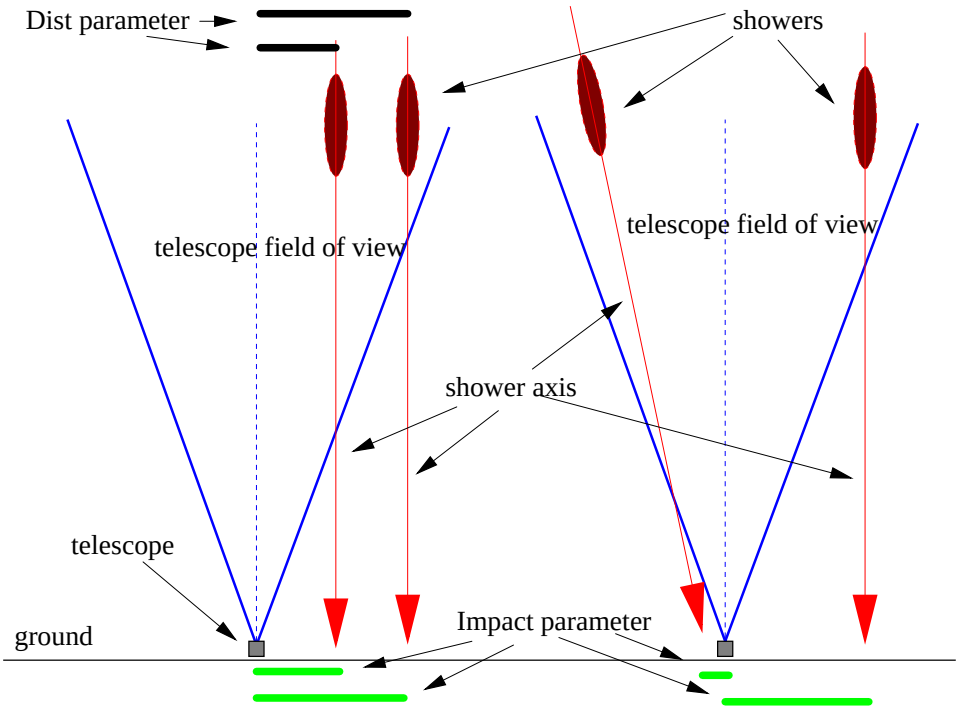

Figure 3.48: The Impact parameter reconstruction. In the picture the telescope is represented by a gray box, the telescope field of view by the blue lines, the showers by the red ellipses, and the showers axes by the red arrows. On the left the geometrical relation between the Impact parameter (green thick lines) and the Dist parameter (black thick lines) is illustrated . On the right the relation between the Impact parameter (green thick lines) and the Length parameter is shown. The Length parameter is not shown in the figure, as it is a function of the shower longitudinal development and of the shower inclination.

with:

$$\Delta(X) = \frac{\sum_i^N (X_{recon} - X_{MC})_i}{N} \tag{3.51}$$

$$RMS(X) = \frac{\sum_i^N (X_{recon} - X_{MC})_i^2}{N} \tag{3.52}$$

where X stays for the Impact parameter or energy, X_{MC} is the MC value, X_{recon} is the calculated value with the above Impact parameter of energy formulae. The minimization consists of the following steps:

α_{Imp}	β_{Imp}	δ_{Imp}
m deg^{-1}	m deg^{-1}	m
667 $\pm$ 65	132 $\pm$ 65	-30 $\pm$ 16

Table 3.23: The table of the parameters for the Impact Parameter estimation. The parameters values are obtained with a minimization procedure on a MC simulations sample.

α_{En}	β_{En}	δ_{En}
TeV ph.e^{-1}	TeV m^{-1}	TeV
0.215 $\pm$ 0.018	-0.079 $\pm$ 0.063	22 $\pm$ 18

Table 3.24: The table of the parameters for the Energy estimation. The parameters values are obtained with a minimization procedure on a MC simulations sample.

- A sample of MC simulation is used for the minimization. To those events the same NSB light of the SN1006 observations is added.
- The events are selected with the same cuts used for the real data.
- The selected events are used for calculating the f(Imp)$_m$ and f(En)$_m$ functions.
- The calculations are iterated because the minimizing program spans the free parameters space for the Impact parameter and energy formulae.
- As a final result a set of free parameters, which provide the minimum value for the f(Imp)$_m$ and f(En)$_m$ is obtained. These values are listed in tables 3.23 and 3.24.

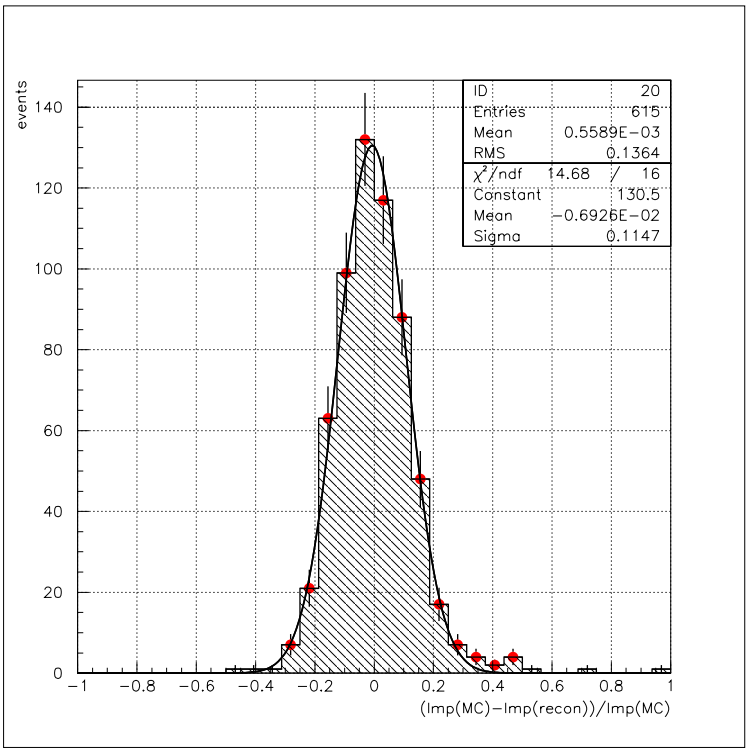

Figure 3.49: Comparison of the simulated and the reconstructed Impact parameter. Here the percentage difference between the *true*(MC) Impact Parameter and the reconstructed Impact Parameter, for a sample of simulated γ events, is plotted. The data can be described by a Gaussian distribution with $\sigma = 0.11$.

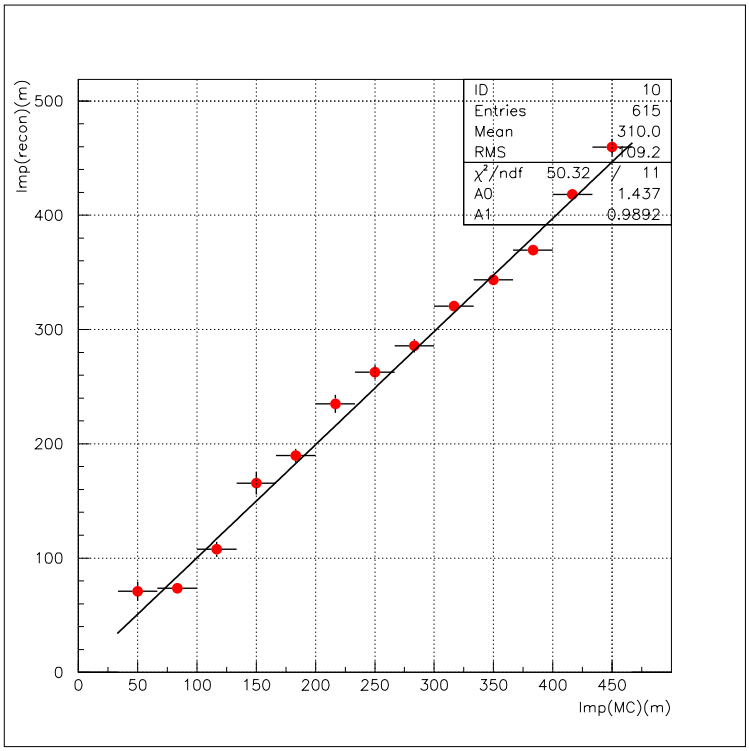

Figure 3.50: Comparison of the simulated and the reconstructed Impact parameter. The correlation is well described by a linear function with slope = 0.98 and offset of 1.4m.

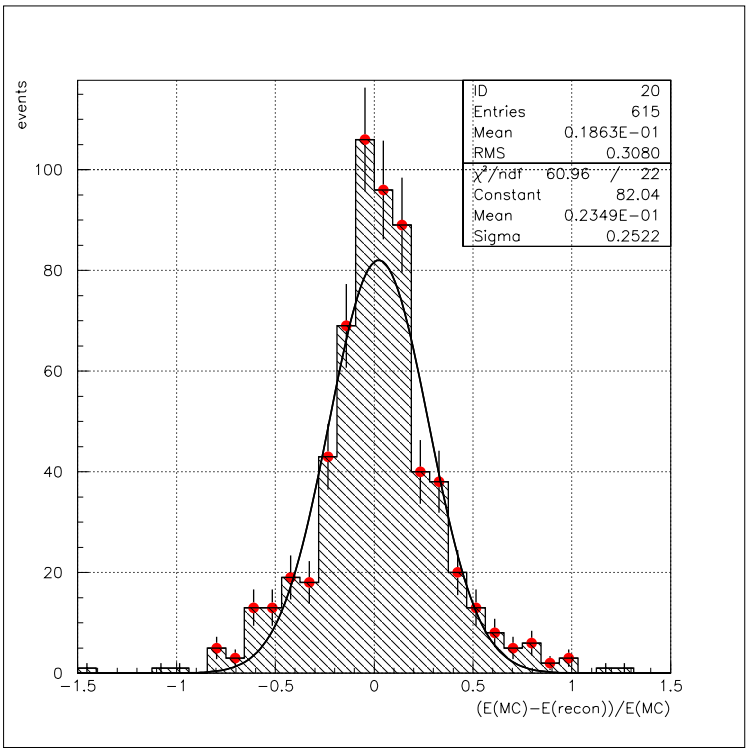

Figure 3.51: Comparison of the simulated and the reconstructed Energy. Here the percentage difference between the *true*(MC) Energy and the reconstructed Energy, for a sample of simulated γ events, is plotted.The data can be described by a Gaussian distribution with $\sigma = 0.25$.

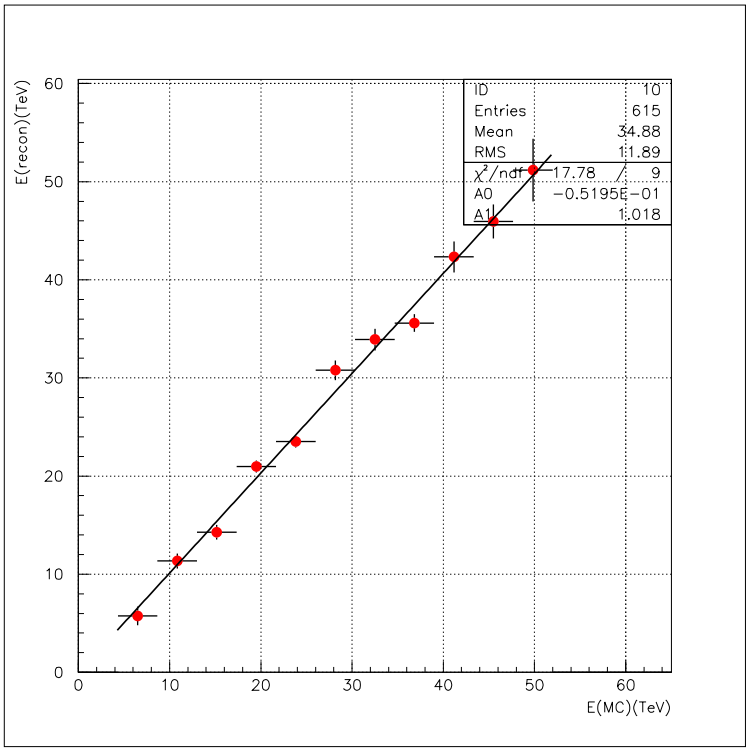

Figure 3.52: Comparison of the simulated and the reconstructed Energy. The correlation is well described by a linear function with slope = 1.018 and offset of 0.0051 TeV .

Chapter 4

Results and Discussion

This chapter reports the results and conclusions. At first the main questions, which are under study, are listed. A summary of the study procedure is given in subsection 4.1.1, and the results are given in subsection 4.1.2. The results are discussed in section 4.2, they are also compared to the other experimental observations and some of the theoretical models.

4.1 Results on the SN1006

We have been searching for a possible emission of TeV γ rays because it would be an indirect evidence of the charged particles acceleration by the SNR blast waves. Therefore the main question related to my thesis is:

- *are TeV γ rays emitted by the SN1006 remnant ?*

In case of a positive answer a further investigation on the acceleration mechanism and on the charged parents of the γ rays can be done. The emitting region and the γ rays flux are related to the acceleration mechanism. The type of accelerated charged particles (electrons or nuclei) can be studied by means of the energy distribution of the non-thermal radiation, emitted at radio, X and γ ranges. Therefore two other main questions have been considered:

- *is it possible to locate the emitting region within the SN1006 sub-structures (North-East cap, South-West cap, central region) ?*
- *what is the eventual integral flux of TeV γ rays from the SN1006 ? and the differential one ?*

These questions have been the motivation for this data analysis of the CT1 observations of SN1006.

4.1.1 The study procedure

The statistics of the used data and MC sample used for the SN1006 study are listed in table 4.1. From the table it is possible to see that:

1. The observation was restricted to a narrow zenith angle range between 71 and 73°.

2. A deep exposure ($\approx$ 220 hours) of the source has been performed. It should be noted that the used 668 runs ($\approx$ 0.33h each run) have been selected. Some other runs (less than 100 [1]) have been rejected because they have been taken during non-optimal atmospheric conditions, as also considered at second point of the following summary.

A summary of the used methods (as discussed in detail in the previous chapters) is reported below:

- In order to reject accidental noise triggers and samples recorded during non optimal atmospheric conditions the preprocessing and the filtering of the data have been performed, as described in section 3.1. For the SN1006 data taken during optimal atmospheric conditions the average trigger rate after filter (see 3.1) is (0.5$\pm$0.1)Hz.

- The dominant background of hadronic events has been rejected with the selection cuts for large zenith angle, discussed in detail in sections 3.3. The selection cuts are mainly based on the study of the experimental hadronic events, spanning the full zenith angle dynamical range (from 0 to more than 73°) A specific study of the muon background has been performed (subsection 3.3.5) and a rejection cut for muons has been developed.

- The sky maps of the events excess and of the excess significance have been obtained[2]. The sky maps have been produced by means of the

[1] A fraction of the rejected runs data is actually available only on the original tape archive (spread across 3 years of other observations). The work copy has been lost because of a severe failure of the storage device. This situation prevents the presentation of a more precise statistics about the rejected runs.

[2] All the sky maps are obtained from a two dimensional distribution with angular resolution of 0.1 degree, by means of the default P.A.W. smoothing function for contour plots.

FSM (False Source Method, in section 3.4). For the sky maps, the residual background has been obtained with the *Alpha fit* method. The significance has been computed with the most conservative of the formulae shown in subsection 3.4.2. Both sky maps are shown in Fig. 4.2 and 4.3. Also, the distribution of the signal and of its significance have been obtained, for a grid in the FOV, and they are shown in Fig. 4.4 and 4.5.

- The pixels anode currents are sensitive to steady light sources, for example the stars. The anode currents have been analyzed and two stars, relatively bright, have been found in the field of view (κ Cen and β Lup). With these two stars it was possible to have an independent and precise (less than 0.12 °) sky position reference (see section 3.2).

An event excess with significance greater than 5 σs (γ rays signal) has been found at the North-East cap of the SNR shell (see Fig. 4.2 and 4.3)

- The events excess at the North-East cap has been studied. The Alpha plot has been extracted and the residual background has been evaluated with an independent method (*Ring* method).

- The significance has been calculated again, in respect of the better estimated background. It has been corrected for a number of trials performed to find the signal. The hypothesis under test is: does a significant event excess come from the North-East cap of the SN1006 remnant? Therefore, the trials number is the number of sky map positions needed in order to scan the North-East cap of the SNR shell.

- The integral flux of the γ rays from the North-East cap has been calculated, using the method described in section 3.6. The integral flux has been calculated for many different indices of the assumed differential energy spectrum (in the form of a pure power law).

- The differential flux has been obtained. The energy of the events, likely to be γs (those events in the signal region of the North East cap Alpha distribution), has been reconstructed (subsection 3.6.3). Then an unfolding procedure has been applied, to correct the effects of the coarse energy binning. The number of particles in the obtained energy spectrum was normalized to the number of γ candidates excess. Events with Impact parameter larger than 500m have not been used, because 500m was the largest Impact parameter available for the calculation of the effective collection area.

epoch	data type	statistics	runs	<z.a.>[°]	rms(z.a.)[°]	min(z.a)[°]
1999	exp.	142054	303	71.8	1.3	70.6
2000	exp.	105475	204	72.0	1.5	70.6
2001	exp.	98491	161	71.2	0.7	70.6
	MC (γ)	10673		72		72

Table 4.1: The statistics of the used data sample. The epoch indicates the period of observations. The data are either experimental (exp.) or MC simulations, all of them after the trigger. The number of data acquisition runs is reported. Each run lasted 20 minutes.The total accumulated observation time was 222.7 hours. Both number of event and number of run are after the rejection of the data collected during non optimal atmospheric conditions. Three columns describe the zenith angle (z.a.) distribution, giving the average z.a, the z.a. distribution rms and the minimum z.a.

- A similar analysis has been performed for the South-West cap and the central region of the shell. No signal has been found in these locations. Upper limits at the γ rays integral flux from these regions have been calculated. The South-West cap is extended over many sky map positions, therefore the average of the events excesses and the rms of their distribution have been used to obtain the upper limit; the same was done for the central region. The upper-limits are based on the average number of counts in the sky map bins, which cover the investigated region. Therefore no trials are considered.

4.1.2 The Results in detail

The results of the present work are:

1. **The detection of TeV γ rays from the North-East cap of the SN1006 remnant.**

2. The TeV γ rays emission is detected as an excess of events. The excess consists of 103$\pm$17 events. The residual background consists of 225$\pm$9 events.

3. In accordance to Lee and Ma [51] (see section 3.4.2) **the excess significance is 5.1 σs**. The pre-trials significance was 5.6 σs.

4. The integral flux Φ_γ as a function of the photon index Γ, ranging from -1.0 to -3.0, and of the energy threshold E_{th} is reported in table 4.3. The integral flux with Γ = -2.0 (the photon index favored by the γ energy spectrum fit) is

$$\Phi_\gamma(\mathbf{E{>}18{\pm}2\ TeV}) = \mathbf{(2.35 \pm 0.39)\ \ 10^{-13} cm^{-2} s^{-1}}. \quad (4.1)$$

The energy threshold (E_{th}) for the same photon index is 18±2 TeV.

5. **A systematic uncertainty $\delta\Phi_{syst.} = 30\%$** has been considered for the fluxes calculations. A detailed discussion of the considered systematic errors is presented in subsection 4.2.1. With the inclusion of the systematic errors, the integral flux, for Γ = -2.0, becomes:

$$\Phi_\gamma(\mathbf{E{>}18{\pm}2\ TeV}) = \mathbf{(2.35 \pm 0.4_{stat} {+} 0.7_{syst.})\ 10^{-13} cm^{-2} s^{-1}}. \quad (4.2)$$

6. The differential flux, in the form of a pure power law $C_{scale} \times E^{-\Gamma}$, is:

$$\frac{d\Phi}{dE} = \mathbf{(0.30 \pm 0.15) \times 10^{-11} \times \left(\frac{E}{TeV}\right)^{-1.9\pm0.2}\ TeV^{-1}\ cm^{-2}\ s^{-1}} \quad (4.3)$$

The errors include the statistical ones, and those for the energy reconstruction. A 30 % systematic error is not included. The differential flux and the power law fit are shown in Fig. 4.8. It should be noted that for a 5σs effect the calculation of a differential spectrum is barely possible.

7. No signal (events excess with significance larger than 5σs) has been found at the South-West cap and at the central region location (see table 4.2). It is therefore possible to set an upper-limit for the integral flux from the South-West cap:

$$\Phi(\mathbf{E{>}18TeV})_{\gamma,SW} < \mathbf{0.83\ 10^{-13} cm^{-2} s^{-1}} \quad (4.4)$$

at a confidence level of 95%, under the assumption of a power law with photon index Γ=-2.

The upper limit for the SNR central region is:

$$\Phi(\mathbf{E{>}18TeV})_{\gamma,center} < \mathbf{0.66\ 10^{-13} cm^{-2} s^{-1}} \quad (4.5)$$

also this at a confidence level of 95%, under the assumption of a power law with photon index Γ=-2.

region	Num.Pos.	average excess	excess rms	max significance
		counts	counts	σs
SW cap	5	1.8	21.5	2
center	16	0.3	22.6	1

Table 4.2: The average events excess and the excess rms at the South-West cap and at the central region of the SN1006 remnant.The number of sky map position which have been considered for each region is reported in the column Num.Pos.

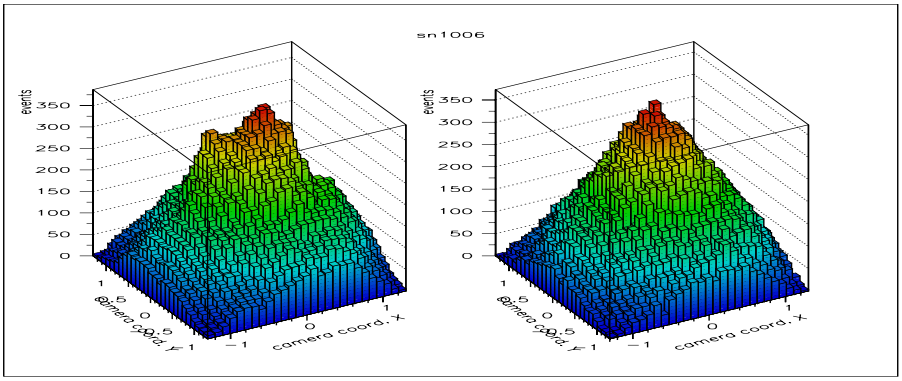

Figure 4.1: The lego plots for the ON-data after cuts (left plot) and the estimated residual background (right plot). The plots show the distribution of the events over a section of the sky plane (affected by the camera acceptance). In the ON-data it is already visible a structure, which corresponds the excess of events at the NE cap of the SN1006 shell.

photon index	E_{th}	Φ	$\delta\Phi_{stat}$
	TeV	$10^{-13}cm^{-2}s^{-1}$	$10^{-13}cm^{-2}s^{-1}$
-1.0	22±2	2.40	0.39
-1.5	22±2	2.15	0.36
-2.0	18±2	2.35	0.39
-2.5	18±2	2.21	0.36
-3.0	18±2	1.72	0.29

Table 4.3: The table of the integral flux (Φ_γ) and its statistical uncertainty. The integral flux depends on the assumed differential flux. For many TeV γ ray sources the differential flux is still to be measured in detail. An exception is Crab, studied up to $\approx$ 100 TeV. Therefore it is assumed a differential flux in the form of a pure power law $C_{scale} \times E^{-\Gamma}$, where C_{scale} is a scale factor and Γ is the photon index. Here the integral flux is calculated for Γ going from -1 to -3. Also the corresponding energy threshold E_{th}, as a function of the assumed photon index, is listed. The stability of the results in the region -2.5$<$ Γ $<$ -1.5 implies that an error on the assumed photon index will generate only a small error in the flux evaluation.

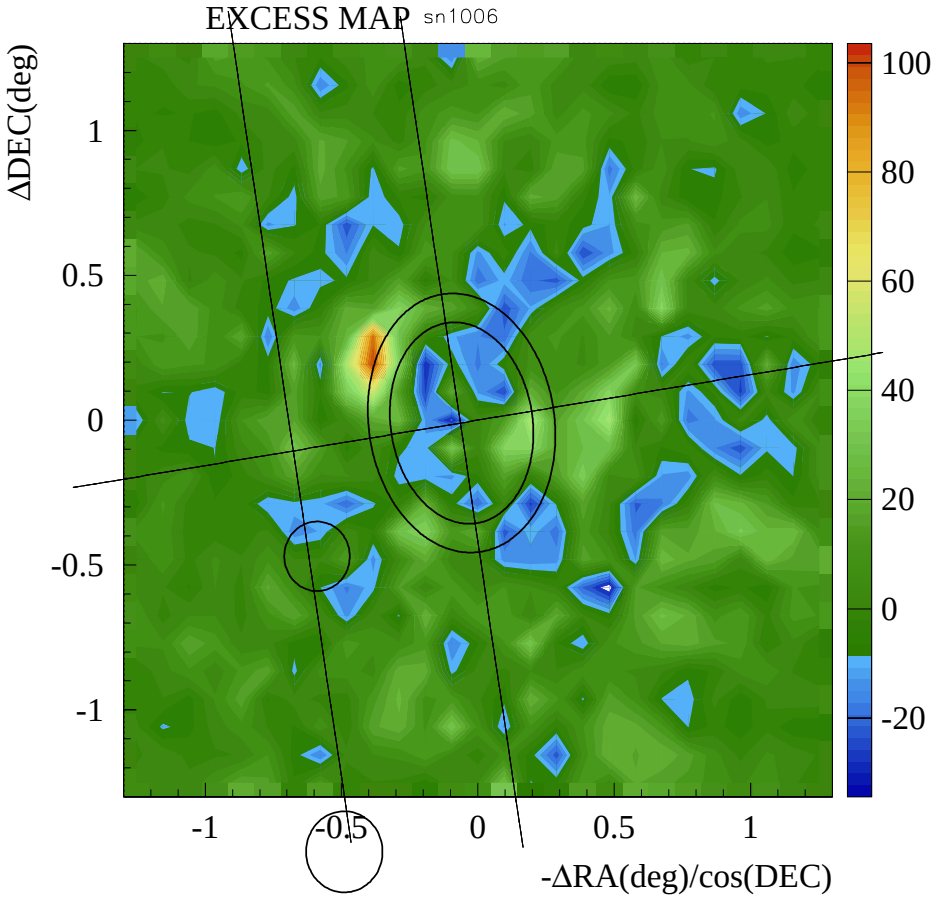

Figure 4.2: The sky map of the event excess. The Declination and the Right Ascension directions (the two inclined axes) have been reconstructed by means of two observed stars: κ Cen (the black circle in the map, close to (-0.5,-0.5)) and β Lup (the black circle out of the map, on the bottom). In the map it is evident a maximum, located in the North-West region of the SN1006 shell (the black double ellipse). This maximum consists of 103$\pm$17 events.

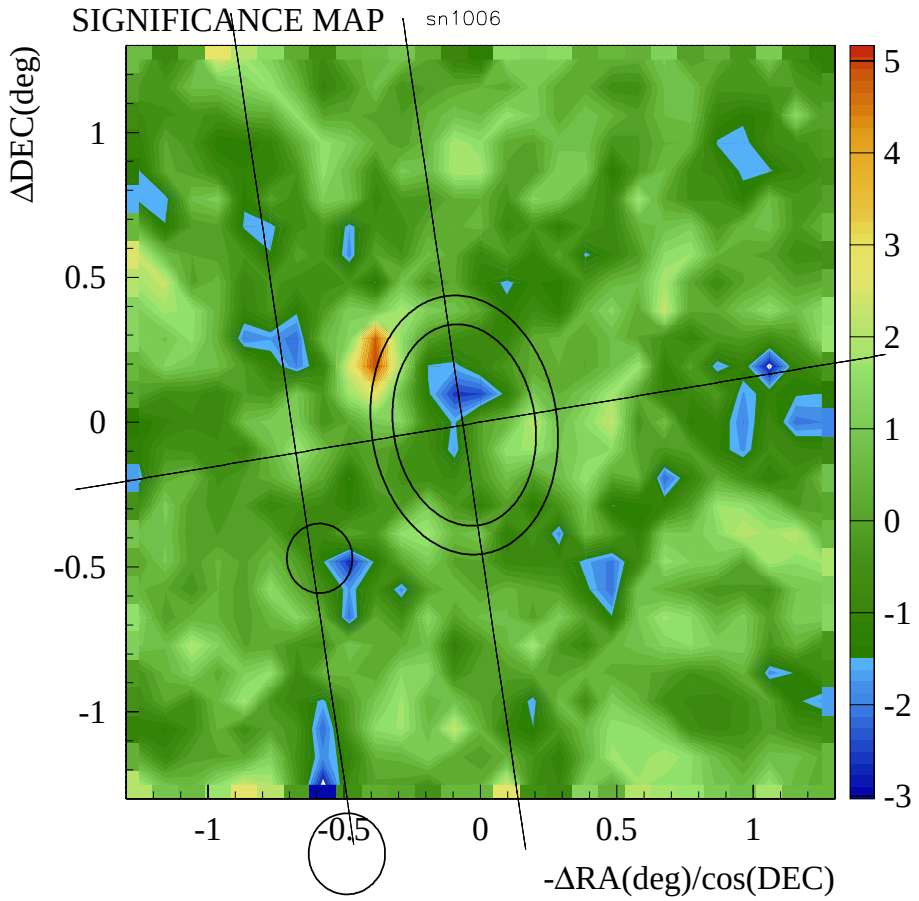

Figure 4.3: The sky map of the excess significance. The Declination and the Right Ascension directions (the two inclined axes) have been reconstructed by means of two observed stars: κ Cen (the black circle in the map, close to (-0.5,-0.5)) and β Lup (the black circle out of the map, on the bottom). In the map it is evident a maximum, located in the North-West region of the SN1006 shell (the black double ellipse). This maximum has a significance larger than 5 σs.

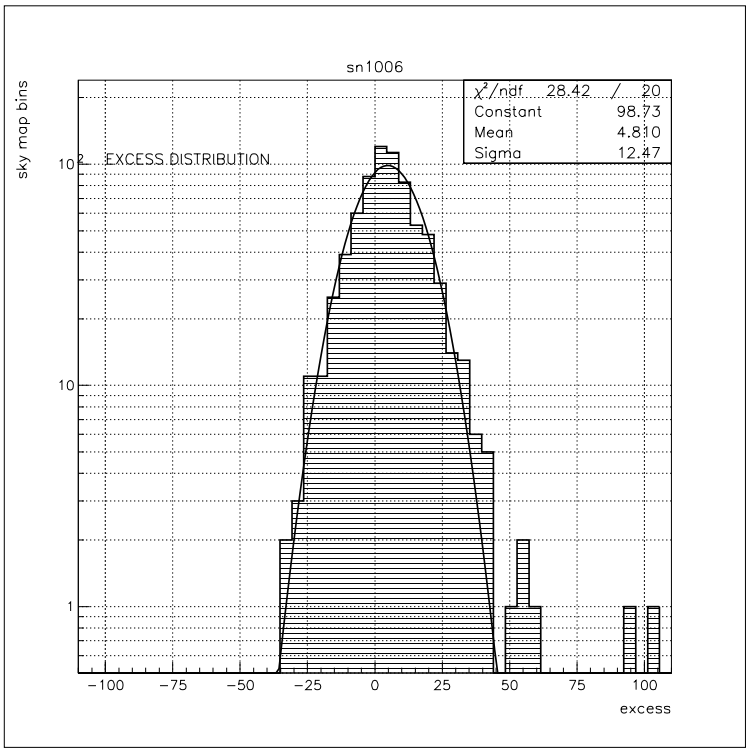

Figure 4.4: The events excess distribution for the local sky map around SN1006. The data are well described by a Gaussian distribution with σ=12.5. But some positions have events excess ($\approx$ 100)well outside the Gaussian distribution.

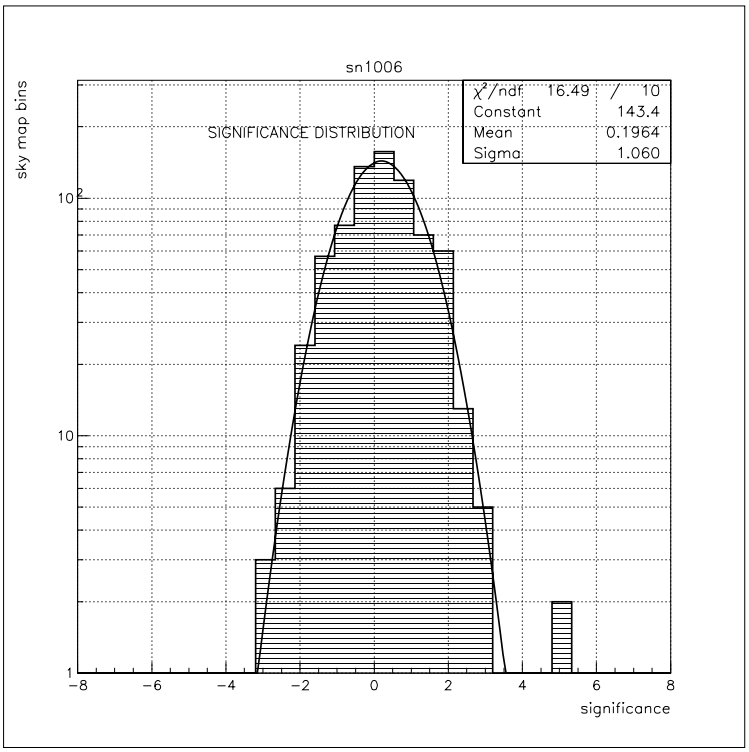

Figure 4.5: The excess significance distribution for the SN1006 sky map. The data are well described by a Gaussian distribution with σ=1.060. But two positions are outside the Gaussian distribution, and have significance higher than 5 σs.

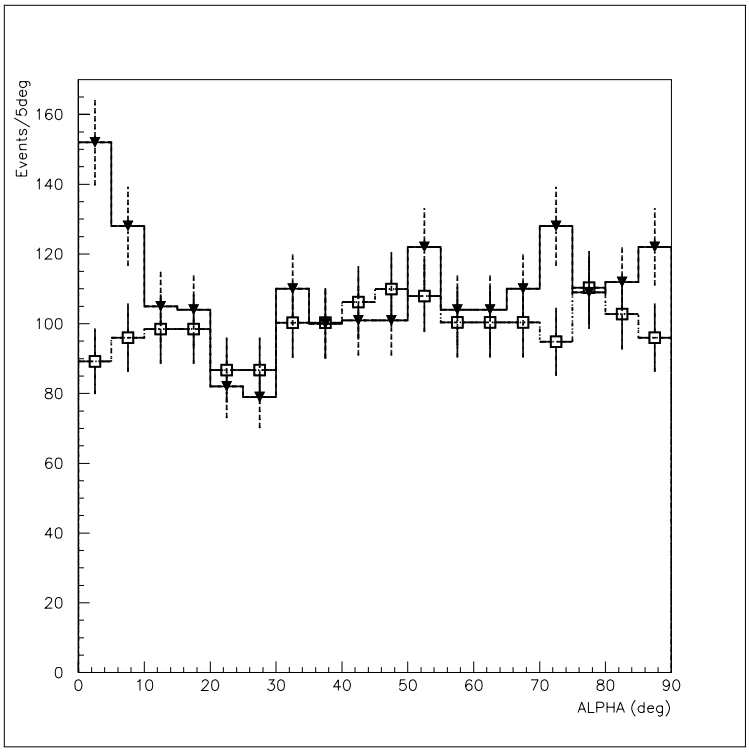

Figure 4.6: The Alpha parameter distribution for one of the two positions (-0.4,0.2, camera coordinates) with highest significances. The black triangles are the source data, the empty boxes are the ring background data. A clear peak is present at the signal region (Alpha$<12.5^{\circ}$).

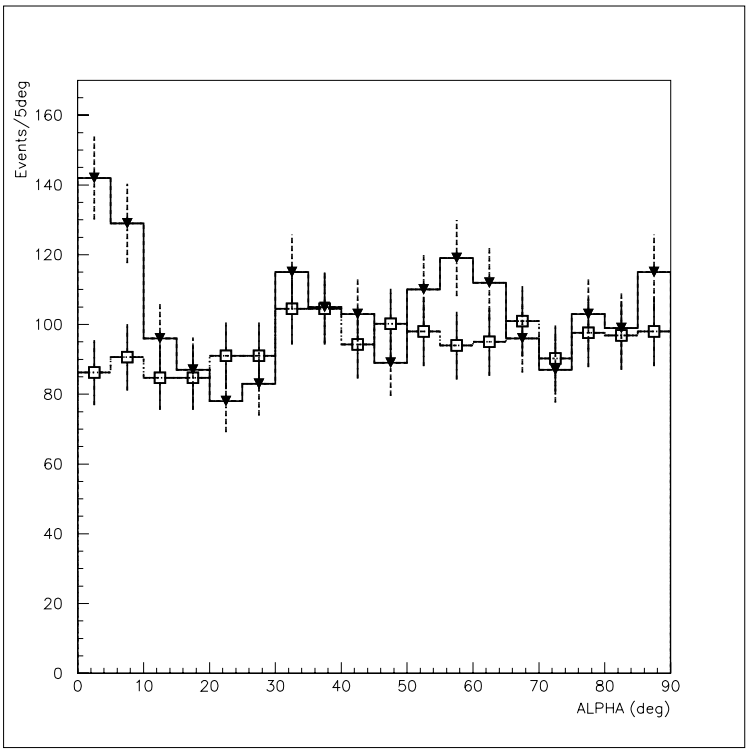

Figure 4.7: The Alpha parameter distribution for one of the two positions (-0.4,0.3, camera coordinates) with highest significances. The black triangles are the source data, the empty boxes are the ring background data. A clear peak is present at the signal region (Alpha<12.5°). Note that there is an overlap of data between this and the plot in Fig.4.6

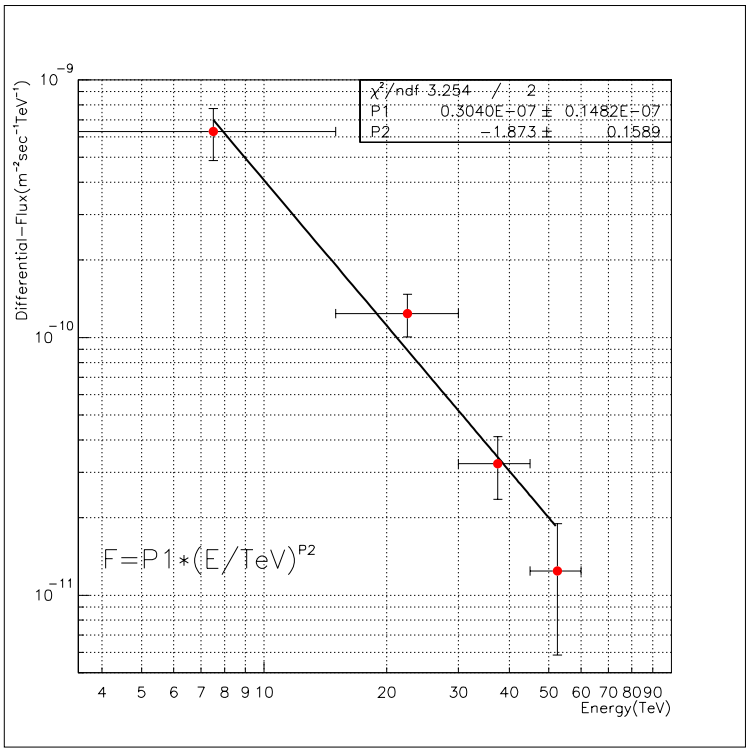

Figure 4.8: The Differential Flux versus the Energy. Here the differential flux from the North-West cap of the SN1006 is shown. Data are grouped in 4 energy bins. The differential flux is fitted with a pure power law:$\frac{d\Phi}{dE} = (0.30 \pm 0.15) \times 10^{-11} \times (\frac{E}{TeV})^{-1.9 \pm 0.2}\ cm^{-2} s^{-1} TeV^{-1}$. The reduced χ^2 of the fit is $\frac{3.25}{2}$.The errors include the statistical ones, and those for the energy reconstruction. A 30 % systematic error is, instead not included.

4.2 Discussion of the Results

Here below are the direct implications of the SN1006 data analysis. From the TeV γ ray sky map the following considerations can be drawn:

- With the CT1 sensitivity, the TeV γ rays are detected only from a small region. This region is located at the North-East part of the SN1006 remnant shell (see map in Fig.4.2). The location has a precision of 0.12°. It coincides with one of the three main regions, which are defined by the X-rays observations:

  - North-East shell cap, dominated by non-thermal X rays emission;

  the other two, which are not detected in the γ range, are

  1. South-West shell cap, also dominated by non-thermal X rays emission and opposite to the North-East cap;
  2. the Central region, with thermal X rays emission.

- 8 close sky map locations have events excess higher than 37 events, and among them 3 have more than 60 events (being the events excess distribution σ = 12.5 events), with this analysis. The emitting region might be moderately extended. Structures long few tens of arc-min and large few arc-min are seen at other wavelengths (see [29] for example). However, it is not possible to resolve structure of this angular size with the CT1 angular resolution, which is in the order of 0.1°.

- The region of maximum γ rays brightness is limited at the shell and does not extend inside the central region.

The following conclusions can be drawn from the calculated integral and differential energy spectrum:

- A pure power law, with photon index Γ= -1.9$\pm$0.2 fits the differential energy spectrum (reduced χ^2= $\frac{3.25}{2}$). Any further spectral analysis is limited by the small statistics.

- Up to 40TeV a cut-off in the energy spectrum of the γ emission is unlikely.

- The detected γ rays are of the highest energy one has ever detected from the SN1006 remnant.

4.2.1 The main systematic errors

Here I discuss the main systematic errors for the SN1006 data analysis.

The main source of systematic errors may be a not-so-detailed knowledge of the atmospheric transmission (for example see [55], [56]). A small atmospheric transmission change, which lasts during the data taking time, determines a systematic change for the air-showers Cherenkov photons collection. Therefore the Cherenkov photons collection and the shower image extention (Width and Length parameters) predicted by MC simulations may slightly differ from the real ones. Then the following quantities are affected:

1. the selection cuts γ efficiency (ϵ_γ), then the determined γ rays flux;
2. the energy reconstruction.

For the relevant wavelengths, the atmospheric transmission is determined by:

- Rayleigh scattering;
- ozone and O_2 absorption;
- aerosol (Mie) scattering (this is the most critical one).

These effects, shortly introduced in section 2.4 (see also [35]), depend on metereological (see [57]) and geographical factors (for example, at La Palma the Sahara desert sandstorms), and are difficult to be controlled. The expected change in the image extension can be calculated from the atmospheric transmission change:

$$\frac{\delta K_{trans}}{K_{trans}} \approx \frac{\delta W_{image}}{W_{image}} \quad , \quad \frac{\delta \epsilon_\gamma}{\epsilon_\gamma} \approx 10 \frac{\delta W_{image}}{W_{image}} \tag{4.6}$$

where K_{trans} is the atmospheric transmission, W_{image} is the Width parameter of an air shower image, the relation is linear at a first approximation; the γ efficiency (ϵ_γ) variation is obtained by means of the study in subsection 3.3.6. Nevertheless the reduction of the image extension is limited by the *saturation* effect, reported in subsection 3.3.4.

Some very large changes in atmospheric transmission are estimated in [55] to be between -6 % and +4% for vertical observations. In Table 4.4 are reported the systematic errors on the γ efficiency (ϵ_γ) and the energy reconstruction as function of the atmospheric transmission change. The values in [55] are extreme, then ± 0.03 are preferred. The positive atmospheric transmission changes (better transmission) are not so likely.

$\frac{\delta K_{trans}}{K_{trans}}$	$\frac{\delta E}{E}$	$\frac{\delta \epsilon_\gamma}{\epsilon_\gamma}$
-0.06	-0.06	+0.60
-0.03	-0.03	+0.30
0.03	0.03	-0.30
0.04	0.04	-0.40

Table 4.4: Table of the systematic errors, induced by the atmospheric transmission changes, on γ efficiency ϵ_γ and energy.The values in [55] are extreme, therefore ± 0.03 are preferred.The positive atmospheric transmission changes (better transmission) are no so likely.

Experiment	Scale constant at 1TeV	Spectral Photon Index
	10^{-11} cm^{-2} s^{-1}TeV^{-1}	
Cangaroo	1.1±0.4	-2.3±0.2
HEGRA CT1	0.3±0.15	-1.9±0.2

Table 4.5: Comparison table of the CANGAROO and HEGRA CT1 experimental results on the SN1006 remnant.

4.2.2 Comparison with the other observations

Here I compare the results, obtained with the HEGRA CT1 data, with those of other experiments.

TeV γ rays from the SN1006 remnant have been detected for the first time by the CANGAROO collaboration [25]. The CANGAROO collaboration published a differential flux of:

$$\frac{d\Phi}{dE} = (1.1 \pm 0.4)10^{-11} \times (\frac{E}{TeV})^{-2.3\pm0.2}\ cm^{-2}s^{-1}TeV^{-1} \qquad (4.7)$$

The CT1 data analysis results for the integral and the differential fluxes are not in contrast with those reported by CANGAROO. The photon index ranges reported by CANGAROO and by this work do not overlap, but they marginally touch. The CT1 results predict a harder ($<1\sigma$) spectrum than the CANGAROO data. The scale constants (i.e. the flux at 1 TeV) also do not overlap. The CT1 results allow lower fluxes, at low energy (i.e. some TeV), than those permitted by CANGAROO results. The location of the emitting region and its morphology is in agreement for both the CT1 and

the CANGAROO detections. It should be noted that the CANGAROO collaboration can observe the source at low zenith angle, because their telescopes are located in the southern hemisphere. Therefore the CANGAROO observations have a much lower energy threshold and a larger statistics than CT1.

The HESS collaboration, which has recently started to operate a system of IACTs in Namibia, has been also observing the SN1006 remnant [58]. They used 2 IACTs, operated in a stand alone mode, with low energy threshold energy (100-250 GeV),and cumulated exposure for 7 hours. The HESS collaboration reports up to now no evidence of γ emission. No upper-limit on the integral flux has been published yet (December 2003). Before the publishing of the HESS results, is not possible to draw any conclusion.

4.2.3 Signal variability

There might be a time dependence on the γ ray flux. The time-dependence of the excess events has been studied, also in relation to the comparison with the CANGAROO and HESS results. The following data have been used for the study:

1. *Excess events from the NE cap position*, which survived the selection procedure (γ candidates) and have Alpha parameter < 12.5 °, (Alpha calculated respect to the NE cap position).

2. *Background events* (type I), which survived the selection procedure but have Alpha parameter between 25 and 75°, (Alpha calculated respect to the NE cap position).

3. *General background events* (type II), which have Alpha $> 15°$, (Alpha calculated respect to the camera center), and satisfy the data quality requirements.

The acquisition rate of the background events is expected to be constant. Therefore the ratio R=$\frac{background}{excess}$ has been used to measure the excess acquisition rate. Two different background types have been used, in order to cross-check the results and to recognize the eventual systematic errors. In Fig. 4.9 the normalized ratio R is shown versus the time. From this study it is possible to conclude that:

- a constant function fit is favoured respect to the first order polynomial function one (see table 4.7 for the fit parameters and the reduced χ^2).

E.R.$_{ext}(pc)$	V$_{switch}$	$\tau_s(years)$
6.8±3.4	c	20±10
0.2	c	0.6
0.04	c	0.13

Table 4.6: Table of the variability time scale in dependence of the emitting region extension. Here τ_s is the time to stop the emission process in years, E.R.$_{ext}$ is the emitting region extension in parsec. Three alternative E.R. are considered. V$_{switch}$ is the velocity of the signal which travels across the source and switches off the emission.

- the γ rays events rate has been stable during the three years of data collection, with maximum flux variation in the order of -5.8 $\frac{\%}{year}$.

Therefore no major changes in the γ rays flux have been seen until the MJD $\approx$ 52125.

A theory-driven estimate of the variability time-scale may be obtained from the emitting region extension. The time required to switch off a source is approximately:

$$\tau_s = \frac{E.R._{ext}}{V_{switch}} \tag{4.8}$$

where τ_s is the time for switching off the source, E.R.$_{ext}$ is the emitting region extension V$_{switch}$ is the velocity of the signal which travels across the source and switches off the emission. For the SN1006 multi-TeV emitting region it is possible to assume one of the following alternatives:

- E.R.$_{ext}$ = 6.8±3.4 pc. This value is the (maximum) extension of the emitting region detected with CT1 and with a significance over 5 σs . The associated error come from the SN1006 distance uncertainty (0.6 pc) and from the CT1 angular resolution (3.3pc).

- E.R.$_{ext,max}$ = 0.2 pc and E.R.$_{ext,min}$=0.04. These values come from the extension of the filaments, which emit non-thermal X rays (see [30]). These filaments (a single one or many of them) may be related to the TeV γ emission.

In table 4.6 are shown the values for the τ_s, in dependence of the alternative emitting region extensions and assuming V$_{switch}$ equal to the light speed.

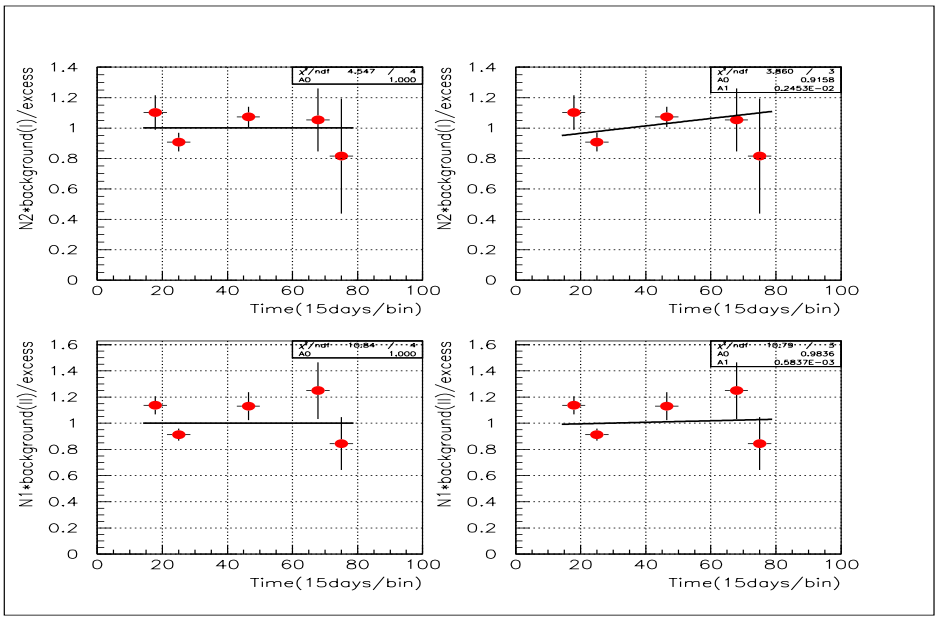

Figure 4.9: The ratio $\frac{background}{excess}$ after normalization (constants N1 and N2) versus the time. The background acquisition rate is expected to be constant. Therefore the ratio R=$\frac{background}{excess}$ has been used to measure the excesses acquisition rate. Two different background types have been used (background type I and II) in order to cross-check the results and recognize the eventual systematic errors. The renormalization constants are N1=59.0, N2=3.27. The time range is between 51000 and 52500 MJD.

background type	fit function	$\frac{\chi^2}{n.d.f.}$	par1	par2
type I	constant	1.1	1.00	
type I	polin. 1^{st} order	1.3	0.9	0.0024
type II	constant	2.7	1.00	
type II	polin. 1^{st} order	2.7	0.98	0.0006

Table 4.7: Table of the fit parameters and the reduced χ^2 for the study of the signal variability.

4.3 Comparison with the models

Below the CT1 results are compared to some models for SN1006 γ emission. They are derived from general models for the SNRs and the GCRs acceleration. Here is a short description of some models:

1. One of the first models is the D.A.V. (Drury, Aharonian, Völk) [59]. It describes the acceleration of GCRs by the SNR shock waves. The CRs seeds are considered to be *test particles* and different from the ISM (*two fluids approach*). The γ rays are produced only with CR-ISM nuclei interaction, via π_0 decay. The model forecasts a maximum of γ rays emission at the Sedov phase, and requires a relatively high ISM density.

2. The Inverse Compton scattering on CMBR and local IR and bremsstrahlung of CR electrons on ISM protons have been included in [60].

3. Subsequently [61] introduced an energy cut-off for the CRs acceleration in the SNR. This limit comes either from the size of the accelerator region, or from the age of the SNR and from the magnetic field intensity.

4. It has been found by [62] that the the CRs seeds modify the shock and form a so-called *shock precursor*, with a non-linear process. Then a curved energy spectrum arises.

Aharonian and Atoyan [63] published a study which considered both an eventual Inverse Compton (IC) and π^0 origin for the TeV γ rays detected by CANGAROO. Conclusions in case of IC case:

- the magnetic field intensity is < 10 μG;
- the shock velocity is > 3000 $\frac{km}{sec}$;
- because of the electron penetration the TeV emission is extended in the inner region of the SNR. This penetration d(E_e) is estimated to be between the full shell radius and a lower limit at:

$$d(E_e) \;=\; \sqrt{2\ D(E_e)\ t_0} \;\approx 0.75(\frac{E_e}{10TeV})^{\frac{1}{2}}\ pc \qquad (4.9)$$

  where E_e is the electron energy, D is the diffusion coefficient for the electrons, t_0 is the diffusion time.

- the energy spectrum is hard between 1 and 10TeV and much steeper above 10TeV.

Conclusions in case of π^0 decay:

- the magnetic field intensity can be higher than 100μG;
- a very fast shock is not required;
- the TeV emitting region coincides with the rim.

They also added that the spatial measurements are an effective test to understand the origin of the TeV γ emission. In this respect we state that the γ emitting region, as seen by CT1, is not significantly extended into the central region and is limited to the rim. The angular resolution of the CT1 (0.1°) does not allow to a spatial measurement so precise as those made with X rays and radio instruments.

More recently Berezhko et al. [64] published another study, where the π^0 origin for the TeV emission is favoured. In this work they consider:

- a magnetic field of 100μG is required for a good fit of the synchrotron emission (from radio and X rays observations);
- then the π^0 component in the TeV γ rays emission dominates over the IC component;
- the γ emission from π^0 can extend up to almost 100TeV (case of efficient proton acceleration);
- the IC component can account for the whole emission only with a magnetic field $<$ of 10μG;
- the γ emission from IC can extend up to $\approx$ 10TeV (case of low magnetic field);

Therefore these authors remark that γ rays of energy higher than 10TeV would imply evidence for hadronic origin. In this respect we should state that: the majority of the γs detected by CT1 have energy $>$ of 10TeV. And also: the CT1 measurements exclude a cut-off in the γ energy spectrum at least up to 45TeV.

4.3.1 Outlook

The SN1006 remnant has been intensively studied during last years (see section 1.5, and also [65]). In the very high energy γ ray range, observations of the remnant, from hundreds of GeV up to many tens of TeV have been performed. Nevertheless these works can be improved:

1. The differential energy spectrum can be better measured with the Cherenkov telescopes of new generation (CANGAROO III, HESS, MAGIC, VERITAS). The Southern hemisphere telescopes can provide information in the energy range from 100GeV to few TeV. They can study a possible *turn over* in the differential energy spectrum, below the few TeV region. The upper energy range, from few TeV to many tens of TeV can be covered by the Northern hemisphere telescopes, which can use the large zenith angle observations. The feasibility of such large zenith angle studies is shown by the present work.

2. The location of the emitting region can be obtained with better precision. In order to achieve such a result, Cherenkov telescopes, which are operated in the so-called stereo mode or telescopes with a very fine pixel grain, can be used. The improved precision in locating the emitting region will allow a better comparison of the very high energy γ rays results with the X rays ones.

3. The study of the long term source variability can be performed, with the periodical observation of the SN1006 remnant.

4. The improvement of the so-called γ/hadron separation power of the analysis, i.e. the finding of more and more refined and effective analysis methods, expecially for large zenith angle observations.

Appendix A

Diffusive Shock Acceleration

In this appendix are summarized the concepts, developed by many authors, about the acceleration of charged particles by means of shock waves. The pincipal references are [31], [14], [16] and [66]. In section 1.3, it was considered that the charged particles, like electrons and nuclei, can be accelerated by the shock waves of the SNRs. The Diffusive Shock Acceleration (DSA) is currently the most favoured process for the particle acceleration. In 1949 Enrico Fermi introduced a mechanism for the acceleration of the Cosmic Rays [1]. The original Fermi's mechanism is today known as the 2^{nd} order Fermi acceleration process. The 2^{nd} order process is not efficient enough to explain the acceleration of Cosmic Rays. The DSA, instead, is based on the so-called 1^{st} order Fermi's process. It provides an adequate efficiency and easily leads to the correct Cosmic Rays energy spectrum. The 1^{st} and 2^{nd} orders Fermi's acceleration processes can be summarized in the following way:

- 2^{nd} order acceleration process happens when charged particles interact with moving clouds of plasma and with the magnetic field present in the plasma. This interaction leads either to a gain or to a loss of energy of the charged particles. The variation of the particles energy is small ($\frac{\Delta E}{E} \propto \beta^2$, where β is the ratio between the shock velocity and the light velocity, and it is always less than 1).

- 1^{st} order acceleration process happens when charged particles interact with a supersonic pressure disturbance (*shock wave*), which moves into a region full of plasma. Every time a relativistic particle passes the shock front, it gains energy. The gain in the energy is larger ($\frac{\Delta E}{E} \propto \beta$), compared to the 2^{nd} order process.

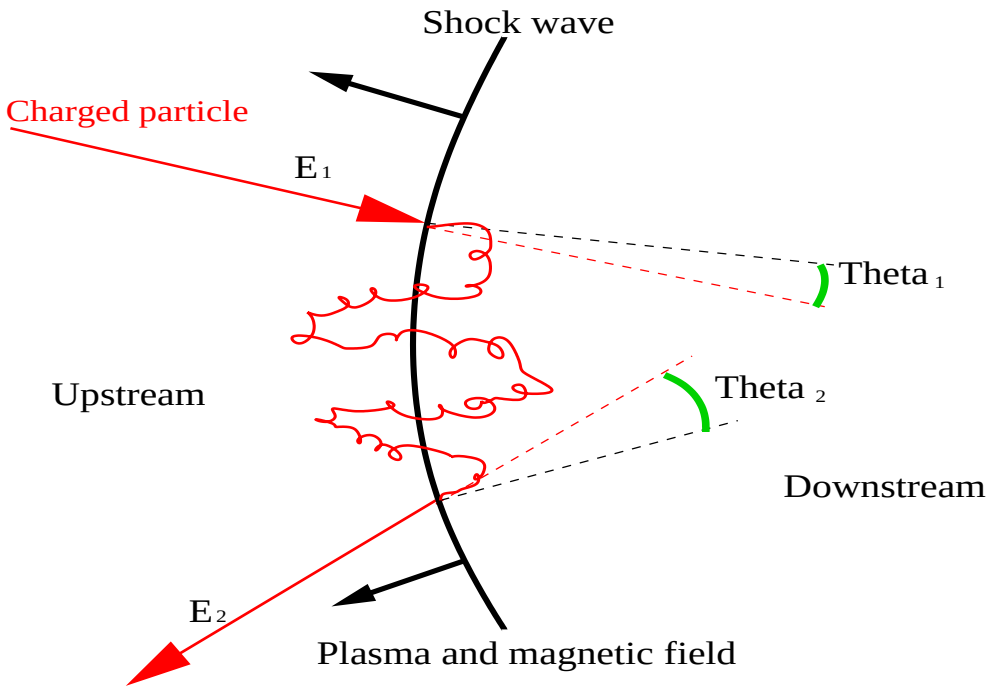

Figure A.1: The illustration of a charged particle, which interacts with a shock wave. A charged particle moves into a region full of magnetized plasma. Coming from upstream, it enters the downstream region. The particle suffers many scatterings by the magnetic field associated with the plasma. These scatterings are *collision-less* and as a result the particle does not loose energy. Because of the scatterings, the particle is likely to cross the shock front many times. At each crossing the particle gains energy.

I will refer to Fig.A.1 in order to describe the 1^{st} order acceleration process. A shock wave (a supersonic disturbance of the pressure level) moves with a velocity $\bar{v}_{shock}$ in respect to the plasma frame. The shock wave divides two regions:

- the already shocked plasma (downstream) on the back of the wave front;
- the region of the plasma (upstream) towards which the shock moves.

A charged particle of energy E_1, coming form the upstream region, enters the downstream region. The particle trajectory and the shock propagation di-

rection make an angle θ_1. In the downstream region, the particle is scattered by the irregularities of the magnetic field (the so-called Alfven waves), which is associated with the plasma. These scattering interactions are collision-less (elastic) and the particle does not loose energy (except possibly for radiative processes like the synchrotron radiation of the electrons).

1. The variation of the energy.

   Because of the scatterings, the particle crosses the shock front many times, and at each crossing its energy changes. In fact

$$E_1^{'} \;=\; \gamma E_{ent}\;(1 \;-\; \beta\; cos\theta_1) \tag{A.1}$$

$$E_2 \;=\; \gamma E_1^{'}\;(1 \;+\; \beta\; cos\theta_2) \tag{A.2}$$

$$\frac{E_2 - E_1}{E_1} \;=\; G \;= \frac{1 \;-\; \beta\; cos\theta_1 \;+ \beta\; cos\theta_2 \;-\; \beta^2\; cos\theta_1 cos\theta_2^{'}}{1 \;-\; \beta^2} - \;1 \tag{A.3}$$

   where E_1 is the starting energy of the particle, E_2 is the particle energy after the process, $E_1^{'}$ is the particle energy downstream, θ_1 and θ_2 are the entering and escaping angles, $\beta = \frac{V}{c}$ and V is the velocity of the downstream plasma in respect to the upstream plasma. For a shock wave, it holds (averaging θ in the range 0-90°) :

$$cos(\theta_1) \;\approx \frac{2}{3} \;\;,\;\; cos(\theta_2) \;\approx -\frac{2}{3} \tag{A.4}$$

   therefore

$$G \;\approx\; \frac{1 + \frac{4}{3}\beta + \frac{4}{9}\beta^2}{1 - \beta^2} \;- 1 \;\approx\; \frac{4}{3}\beta \tag{A.5}$$

   After each crossing of the shock front, the particle gains energy proportional to the velocity of the shock.

2. The energy spectrum.

   A charged particle is likely to cross the shock many times before leaving the *accelerator region*. It is possible to calculate the differential energy spectrum of the accelerated particles in the following way:

$$N_k \;=\; N_0 \;\times\; P^k \;\;,\;\; E_k \;=\; E_0 \;\times\; G^k \tag{A.6}$$

$$\frac{N}{N_0} \;=\; \Big(\frac{E}{E_0}\Big)^{\frac{log(P)}{log(G)}} \tag{A.7}$$

therefore

$$\frac{dN}{dE} \;=\; E^{-s} \tag{A.8}$$

and

$$s \;=\; 1 \;-\; \frac{log(P)}{log(G)} \tag{A.9}$$

where N_0 is the total number of particles, P is the probability to cross the shock again, N_k is the number of particles which have made k crossings, E_0 is the starting energy of the particles, E_k is the energy at the k^{th} crossing and G is the energy gain at each crossing. For a shock wave it holds :

$$P \;\approx 4\frac{V_{down}}{c} \quad , \quad G \;\approx \frac{4}{3}\frac{V_{up} - V_{down}}{c} \tag{A.10}$$

whit $V_{up} \approx$ -2 V_{down}, for strong shocks.

$$s \;\approx\; 1 - \frac{4\frac{V_{down}}{c}}{\frac{4}{3}\frac{V_{up}-V_{down}}{c}} \;\approx\; 2 \tag{A.11}$$

where V_{up} and V_{down} are the plasma velocities up and downstream. The 2^{nd} order Fermi's acceleration process, as shown with the previous calculation, produces also energy spectra in the form of a power laws with spectral index -2 . It should be noted that after the diffusion in the galaxy, affects the spectral index. This effect arises because the high energy particle escape more easily the galactic magnetic field, while the low energy particles are better contained. Therefore a particles differential flux, with initial spectral index of -2.0, can arrive at the Earth with a spectral index of -2.7.

3. Estimate of the maximum energy range.

   The maximum energy achieved by a particle depends on the number of shock crossings. Therefore the maximum energy is related to the probability to be contained in the accelerator and the time needed for a crossing. The acceleration rate is:

$$\frac{dE}{dt} \;=\; \frac{G \times E}{T_{cycle}} \tag{A.12}$$

   where T_{cicle} is the needed time for a shock crossing. An estimate for T_{cicle} is :

$$T_{cycle} \;=\; \frac{4}{c}\Big(\frac{D_{up}}{V_{up}} + \frac{D_{down}}{V_{down}}\Big) \tag{A.13}$$

where D_{up} and D_{down} are the diffusion coefficients up and downstream, V_{up} and V_{down} the respective plasma velocities.

$$D \approx \frac{1}{3} V\lambda \approx c \times r_{Larmor} \approx \frac{E\ c}{Z\ e\ B} \rightarrow \tag{A.14}$$

$$E_{max} < \frac{3}{20} \frac{V_{down}}{c} Z\ e\ B\ (V_{down} T_a) \tag{A.15}$$

where T_a is the maximum age of the accelerator, Z is the charge of the particle, r_{Larmor} is the Larmor radius of the particle, B is the magnetic field, at the acceleration site. For the case of the SNRs:

$$E_{max} < Z \times 3 \times 10^4\ GeV \tag{A.16}$$

with T_a=1000y, B=3μG, V_{down}=5$\times$ 10^6m/sec.

Appendix B

Cosmic Rays

Cosmic rays are an intense radiation of extra-terrestrial origin. Here are summarized the basic characteristics of the this radiation (see also [67] and [31]). The Cosmic Rays intensity is in the order of 1 $\frac{particle}{cm^2\ s}$. Cosmic ray particles can arrive either directly from their cosmic source (primary component) or they can be produced *in flight*, by the collisions of primary cosmic rays with the particles of the galactic medium (secondary component). Primary cosmic rays are mainly nuclei (86% H, 11% He, 1% heavier nuclei), electrons (1%) and photons, while other particles, such as positrons or anti-protons, are likely to be a part of the secondary component (i.e. produced with the interaction of high energy nuclei or electrons). The eventual primary component of anti-particles or also anti-nuclei is a matter of study. The non-detection of anti-nuclear matter ($\bar{H}e$, $\bar{L}i$, ..) is related with the asymmetries of the fundamental interactions acting during the primordial bariogenesis.

Cosmic rays energy spectrum extends over many orders of magnitude from 10^6eV to 10^{20}eV. The differential energy spectrum of cosmic rays has its peak at energies of 10^8eV - 10^9eV. At these energies, they are dominated by the radiations emanated by the Sun, which activity undergoes a period of $\approx$11 years. Such periodicity can be seen in the cosmic rays of low energy as a *solar modulation*. Above its peak, the spectrum is well described in terms of pure power law.

$$\frac{d\Phi}{dE} \propto E^{-\Gamma} \tag{B.1}$$

where Γ is the absolute value of the spectral index. The spectral index changes 3 times in the range from 10^6eV to 10^{20}eV. Such changes are linked with the cosmic rays sources.

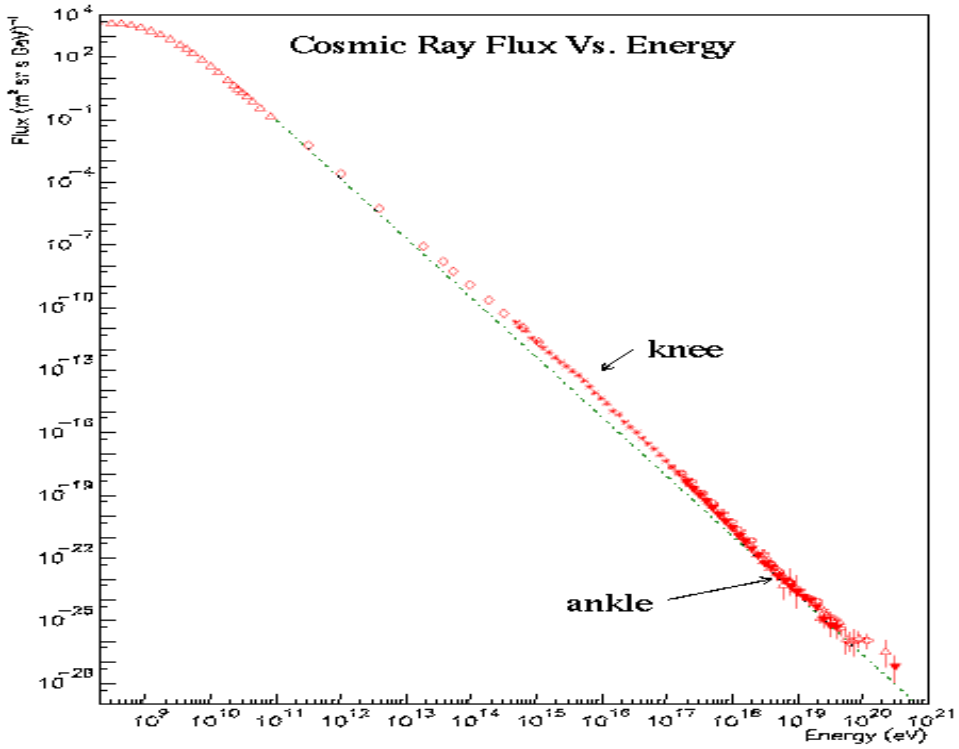

Figure B.1: The differential flux of cosmic rays (nuclei) in the energy range from 10^7 to 10^{13} eV/n (10MeV/n - 10TeV/n). The chemical composition is outlined. It is possible to see the peak of the spectrum and, above, the unbroken power law with the spectral index $\Gamma \approx 2.7$

1. below 3×10^{15}eV (the *knee*) Γ is ≈ 2.7, this component is thought to be of galactic origin;
2. between 3×10^{15}eV and 3×10^{18}eV (the *ankle*) Γ is ≈ 3, the upper limit in the acceleration energy for the galactic cosmic rays sources could generate this steepening of the spectrum;
3. above 3×10^{18}eV Γ is again smaller than 3; an extra-galactic source of the UHE cosmic rays could be responsible for sustaining such particle flux.

At energy higher than 10^{20}eV the interaction of Cosmic Rays and the Cosmic Microwave Background Radiation (CMBR, black body with temperature of 2.74K) becomes important. This is the so-called Greisen-Zatsepin-Kuzmin

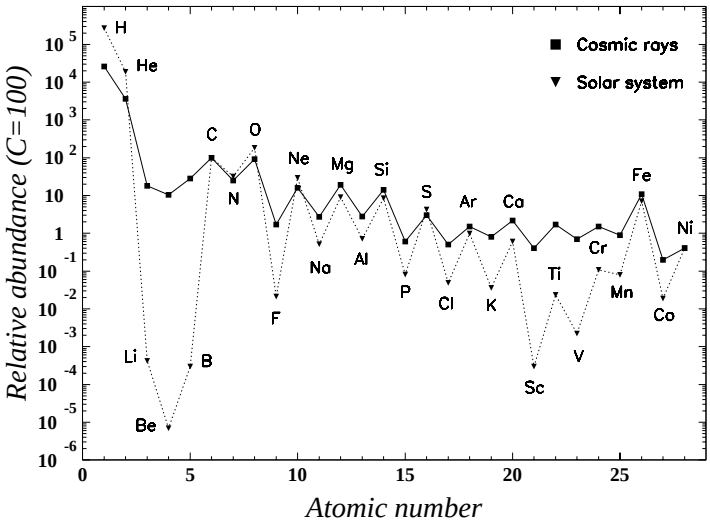

Figure B.2: Relatives abundances of different elements (with Z between 1 and 28), as measured at 1 AU, compared with the chemical abundances in the solar system. The vertical scale is normalized to the Carbon abundance (ref). It is possible to see the difference between the cosmic rays and the solar system matter for the Li-Be-B and for Sc-Ti-V-Cr-Mn groups: $(C,N,O)_{H.E} + A_{target} \rightarrow$ *light nuclear fragments* $Fe_{H.E.} + A_{target} \rightarrow$ *heavy nuclear fragments* where A is a nucleus at rest in the galaxy frame, likely to be a light element like H or He.

cut off. The Cosmic Rays and the CMBR can interact via photo-pion production:

$$\gamma\, p \;\rightarrow\; \Delta^{+} \;\rightarrow\; p\,\pi^{0}\;,\; or \;\; n\,\pi^{+} \tag{B.2}$$

The reaction energy threshold for the proton is in the order 10^{20}eV, the cross section for the reaction is σ=2×10^{-28}cm^2 near threshold; the total CMBR photon density is in the order of 400cm^{-3} (from [67]). Therefore the mean free path for such protons is 10^{23}m (= 5Mpc).

Cosmic rays composition is dominated by light nuclei (H and He). The relative abundances of chemical elements resemble the one of the matter in the solar system but with very important differences. The group of light elements (Li-Be-B) and the group of elements just lighter than iron (Sc-Ti-V-Cr-Mn) are remarkably more abundant in cosmic rays than in the solar system matter. Such abundances are explained in terms of *spallation* of heavier nuclei. Heavy nuclei with enough energy can be fragmented by the collisions with particles of the interstellar matter. Then C,N and O can

produce the Li-Be-B group while Fe can fragment in the elements of the other group (Sc-Ti-V-Cr-Mn).

Together with nuclei, a component of sub-nuclear particles is present, in the cosmic radiation:

- electrons ($e^{\pm}$) the fraction of electrons in the cosmic rays is small. The ratio e/p is in the order of 1 %. It is thought that electrons can easily escape from the Galaxy. Charged particles (i.e. nuclei and electrons) are deflected by the Galactic magnetic field, and it is not possible to trace back their source. Instead UHE nuclei (E $> 10^{20}$ eV)can propagate also in the Galaxy, almost without deflection, because of their very large momentum.

- neutrinos (ν)

  neutrinos are the most abundant specie in terms of the number. They are generated by many interactions and decays at the Earth atmosphere (secondary νs). The Sun is the next and more powerful source of neutrinos (primary νs); for long time it was also the only astrophysical source of νs to be observed. A few neutrinos were detected from the explosion of the SN1987 which was the second detected astrophysical ν source and, until now, the last one.

- gamma rays (γ)

  a component of γ rays is present in the cosmic rays. Cosmic γ radiation is coming from the discrete sources, either point-like or moderately extended. It is also present the diffuse γ radiation, which is coming from the interactions of the high energy charged particles in the galactic environment. Its intensity is $\approx 10^{-6}$ the one of the protons (the precise ratio in unknown). Another diffuse γ radiation component has extra-galactic origin (maybe from unresolved sources). Gamma rays are, together with neutrinos, are not deflected by the galactic magnetic field, during their propagation (also at low energies) and can be traced with appropriate detectors to their origin.

Appendix C

The Hillas parameters

$$< X > = \frac{\sum_i \ s_i X_i}{\sum_i \ s_i} \ , \ < Y > = \frac{\sum_i \ s_i Y_i}{\sum_i \ s_i} \tag{C.1}$$

$$< X^2 > = \frac{\sum_i \ s_i X_i^2}{\sum_i \ s_i} \ , \ < Y^2 > = \frac{\sum_i \ s_i Y_i^2}{\sum_i \ s_i} \tag{C.2}$$

$$< XY > = \frac{\sum_i \ s_i X_i Y_i}{\sum_i \ s_i} \tag{C.3}$$

$$\sigma_X^2 \ = < X^2 > - < X >^2 \ , \ \sigma_Y^2 \ = < Y^2 > - < Y >^2 \tag{C.4}$$

$$A \ = \ \frac{D + \sqrt{D^2 + 4\sigma_{xy}^2}}{2\sigma_{xy}} \ , \ B \ = < Y > \ - \ A \ < X > \tag{C.5}$$

$$Width \ = \ \sqrt{\frac{\sigma_y^2 + A^2\sigma_X^2 - 2A\sigma_{XY}}{1 + A^2}} \tag{C.6}$$

$$Length \ = \ \sqrt{\frac{A^2\sigma_y^2 + \sigma_X^2 + 2A\sigma_{XY}}{1 + A^2}} \tag{C.7}$$

$$Dist \ = \ \sqrt{< X >^2 + < Y >^2} \, , \ Alpha \ = \ ARCSIN\Big(\frac{|B|}{Dist \ \sqrt{1 + A^2}}\Big) \tag{C.8}$$

where X_i and Y_i are the coordinates of the i^{th} pixel, s_i is the calibrated signal of the i^{th} pixel, the shower major axis is given by Y = AX + B, D = $\sigma_Y^2 - \sigma_X^2$ and Width, Length, Dist and Alpha are the main image (Hillas) parameters.

Bibliography

[1] Fermi,E. 1949,Phys.Rev. 75, 1169

[2] Tayler, R. J. Pollacco, D. "The stars: their structure and evolution", Cambridge U Press, 1994

[3] "From Twilight to Highlight: The Physics of Supernovae", Spinger Verlag, proceeding of the ESO/MPA/MPE workshop held in Garching, Germany, 29-31 July 2002, editor W.Hilledrandt et al.

[4] Barry Kellett, Rutherford Appleton Laboratory bjke@ast.star.rl.ac.uk, Rutherford Appleton Laboratory Chilton, DIDCOT, Oxon OX11 0QX, U.K.

[5] Keil, M.T., "SN Neutrino Spectra and Applications to Flavor Oscillations ", PhD thesis, Technische Univesität München, September 2003.

[6] Green D.A., 2000, "A catalogue of galactic Supernova Remnants", Cambridge: Mullard Radio Astronomy Observatory

also as catalog on line

(http://www.mrao.cam.ac.uk/surveys/snrs)

[7] Aschenbach,B., proc. of "Neutron Stars, Pulsars and Supernova Remnants", Bad Honnef (Germany), Jan 2002, pag. 13-25

[8] Schaudel,D. et al., proc. of "Neutron Stars, Pulsars and Supernova Remnants", Bad Honnef (Germany), Jan 2002, pag. 26-28

[9] Pacini,F. , proc. of "Neutron Stars, Pulsars and Supernova Remnants", Bad Honnef (Germany), Jan 2002, pag. 300-302

[10] P.A.Charles, F.D.Seward,"Exploring the X-ray Universe", Cambridge University Press

[11] Dyer, K.K., "Thermal and Nonthermal Emission in Supernova Remnants", PhD thesis, North Carolina State University , December 2001.

[12] George Pavlov and Oleg Kargaltsev, "SNR observed with Chandra"web page, Department of Astronomy and Astrophysics Pennsylvania State University,

http://www.astro.psu.edu/users/green/Main/

[13] Sreekumar,P. and Fichtel,C.E., 1991, Astr.Astrophys. 251, 447-453

[14] Gaisser,K.G., Cosmic Rays and Particle Physics, Cambridge University Press, Cambridge, England.

[15] Aharonian,F., Nature 416 (2002), 797-798

[16] Schönfelder,V., The Universe in Gamma Rays, Springer Verlag 2001, Berlin, Germany.

[17] Schweizer, F. & Lasker, B.M. 1978, apj, 226, 167

[18] Winkler, P. F., Gupta, G., & Long, K. S. 2003, apj, 585, 324

[19] Ghavamian, P., Winkler, P. F., Raymond, J. C., & Long, K. S. 2002, apj, 572, 888

[20] Gardner, F. F. & Milne, D. K. 1965, aj, 70, 754

[21] Winkler, P. F. & Laird, F. N. 1976, apjl, 204, L111

[22] Pye,J.P. et al. 1981, MNRAS, 194, 569

[23] Koyama,K. et al.,Nature.378,255-258,1995

[24] Willingale,R.,et al.,Mon.Not.R.Astron.Soc.,278,749,1996

[25] Tanimori,T.,et al.,Astrophy.J.,497,L25-L28,1998

[26] Vink,J. et al. 2000, A&A, 354, 931

[27] Gupta,G. et al. 2003, Astr.J., 585, 324

[28] Dubner,G.M. et al. 2002, A&A., 387, 1047

[29] Long, K.S., Reynolds, S.P., Raymond, J.C., Winkler, P.F., Dyer, K.K., & Petre, R. 2003, ApJ, 586, 1162

[30] Bamba,A. et al. 2003, Astr.J, 589, 827

[31] Longair, M.S., High Energy Astrophysics, Vol. I, 2nd Ed., Cambridge University Press, Cambridge, England, 1994.

[32] The Particle Data Group, "Review of Particle Physics" 2002, Phys.Rev.D, 66

[33] Leo, W.R., Techniques fo Nuclear Physics Experiments, 2nd Ed., Springer Verlag, Berlin, 1994.

[34] Gilmore, R., Single Particle Detection and Measurement, Taylor and Francis, London, 1992.

[35] Schwarz, R., "Development of a LIDAR for Measuring the Atmospheric Transmission for GeV-TeV γ Astronomy with the 17m MAGIC Telescope", MSc thesis, Ludwig-Maximilians Univesität, München, April 2002.

[36] Mirzoyan, R. et al. New. As. 1998..42..547

[37] Fegan,D.J., J.Phys, G 23 (1997), 1013-1060

[38] Hillas A.M. Proc.19th ICRC (La Jolla) 3,445

[39] Fomin, V.P. et al.,Astrop.Phys. 1994, 2.. 151-159

[40] Fomin, V.P. et al.,Astrop.Phys. 1994, 2.. 137-150

[41] Fomin, V.P. et al.,Izv.Krym.Astr. 1992, 85..127

[42] Mirzoyan, R. et al., proceeding of *Towards a Major Atmospheric Cherenkov Detector IV* 1995, Padua

[43] Petry D., Ph.D. Thesis, 1997

[44] SIMBAD Astronomical Database,

web access at

(http://simbad.u-strasbg.fr/Simbad)

[45] Punch,M et al., Proc. 22nd ICRC (Dublin), 1 464

[46] Reynolds,P.T. et al., Astr.J. 404, 206

[47] Sobczynska, D. et al.,Nucl.Inst.Meth.A 2002, 490..124

[48] Heck, D. et al.,FZKA 1998, 6019

[49] Knapp, J. et al.,Corsika User's Manual 1998, 6019

[50] Lessard, R.W. et al.,Astrop.Phys. 2001, 15.. 1-18

[51] T.Li, Y.Ma, 1983, Astr.J., 272, 317-324

[52] S.N.Zhang, D.Ramsden, 1990, Exper.Astr., 1, 145-163

[53] Capdevielle, J.N. et al., 1992, KfK Report 4998

[54] Aharonian et al.(the HEGRA collaboration), A&A 2003, 410, 813-821

[55] Mohanty,G., Astroparticle Phy. 9 (1998), 15-43

[56] Osborne,J.L., Bull. Astr.Soc. India 30 (2002), 51-59

[57] Pakstiene,E., Baltic Astr. 10 (2001), 651-66

[58] Masterson,C. et al. proceeding of the ICRC 2003, Tsukuba (Japan)

[59] Drury L.O'C.,Aharonian F.,V "olk H.J. 1994,A&A 287, 959

[60] Gaisser,T.K., et al., ApJ 1998 492..219G

[61] Sturner, s. J. et al. ApJ, 1997 490..619S

[62] Baring, M. et al., ApJ, 1999 513..311B

[63] Ahronian, F.A. et al., A&A 1999, 351..330A

[64] Berezhko, E.G. et al.,A&A 2002, 395..943B

[65] 'The NASA Astrophysics Data System', a Digital Library for Physics, Astrophysics, and Instrumentation http://adswww.harvard.edu/

[66] Berezinskii, S.V. et al., Astrophysics of Cosmic Rays, North-Holland, Amsterdam, The Netherlands, 1990.

[67] Perkins, D, Particle Astrophysics, Oxford University Press, Oxford, United Kingdom , 2003.

[68] Naito T.,Takahara F.1994 J.Phys.G 20,477

[69] Tanimori,T.,et al.,I.C.R.C. 2001, Hamburg

[70] Baring M.G.,et al.,Snowbird Workshop on TeV Gamma-Ray Astronomy, Towards a Major Atmospheric Cherenkov Detector - VI,173,AIP,New York, ISBN 1-56396-938-6

Acknowledgments

I would like to thank:

- The ***Max-Planck-Gesellschaft*** and the ***Max-Planck-Institut für Physik, München*** **(Werner-Heisenberg-Institut)**, in the persons of the Board of the Directors. These institutions have granted me a three years scholarship in order to perform the my PhD studies.

- **Prof. Dr. Siegfried Bethke**. He has been my thesis supervisor and he has always been willing to help me when I needed.

- **Dr. Eckart Lorenz**. Eckart has taught me a lot of things, and not only in physics. I want to remember his many efforts to help me in understanding and learning.

- The administrative personal of the MPI. In particular I want to remember **Frau Sybille Rodriguez**, **Frau Ursula Grenzemann** and **Frau Ina Waker**, for their precious help.

- the **Colleagues** of the HEGRA Collaboration, of the MAGIC Collaboration and of the MPI for Physics in Munich. They have been an example for me. Unfortunately it is not possible to list all of them. Here I would like to remember: **Prof. Dr. Masahiro Teshima, Dr. Rudolf Böck, Dr. Razmik Mirzoyan, Dr. Wolfgang Wittek, Ing. Jürgen Gebauer, Dr. Juan Cortina, Dr. Tony Coarasa, Dr. Daniel Kranich, Dr. Dorota Sobczynska, Dr. Martin Kestel, Dr. Florian Goebel, Dr. Kenji Shinozaki**. Among my colleagues I would like to remember in a particular my fellow students: **Markus Garczarczyk, David Paneque, Mustapha Laatiaoui, Nadia Tonello, Robert Wagner, Keiichi Mase** (who had the patience and courage to share with me the same office), **Daniel Mazine, Nepomuk Otte, Heindrik Bartko, Satoko Mizobuchi** and the just arrived **Masaaki Hayashida**.